TECHNISCHE UNIVERSITÄT WIEN

Modeling of tensile twins and texture evolution in AZ31 Mg alloys during deformation

DISSERTATION

zur Erlangung des akademischen Grades

Doktor der technischen Wissenschaften

eingereicht von

Wenwen Wei

Matrikelnummer 1429011

an der Technischen Universität Wien,

Fakultät für Maschinenwesen und Betriebswissenschaften

unter der Leitung von Univ. Prof. Dipl.-Ing. Dr.techn. Ernst Kozeschnik, E308, Institut für Werkstoffwissenschaft und Werkstofftechnologie

Diese Dissertation haben begutachtet:

Univ.Prof. Dipl.-Ing. Dr. techn. Bernhard Sonderegger

PD Dr.-Ing. habil. Matthias Schmidtchen

Wien, am 11.09.2018

Erklärung zur Verfassung der Arbeit

Ich erkläre hiermit, dass ich die vorliegende Dissertation zur Gänze selbst verfasst habe und dazu keine anderen als die angeführten Quellen benutzt habe, und die den benutzten Quellen wörtlich und inhaltlich entnommenen Stellen als solche kenntlich gemacht habe.

Declaration

I declare in lieu of oath, that I wrote this thesis and performed the associated research by myself, using only literature cited in this volume.

_____

Wien, 11.9.2018, Wenwen Wei

Modeling of tensile twins and texture evolution in AZ31 Mg alloys during deformation

Wenwen Wei

DOCTORAL THESIS

TU Wien

Faculty of Mechanical and Industrial Engineering

Institute of Materials Science and Technology

September 2018

Acknowledgements

I thank the China Scholarship Council for providing the financial support for my Ph.D. study at TU Wien. I am especially obliged to Univ.Prof. Dr. Ernst Kozeschnik, my supervisor, who gave me irreplaceable guides and inspired me enormously during my last four years studying and living in Vienna. I also express my special gratitude to Ass.Prof. Dr. Erwin Povoden-Karadeniz, who supported finishing of this thesis with his invaluable suggestions and fruitful discussions. I also thank Tomasz Wojcik and Edith Asiemo for their help in EBSD sampling and measurement. I sincerely express my great gratitude to Harald Radlwimmer for assisting me with the final formatting of this thesis. Finally, I appreciate to all my colleagues at the Institute of Materials Science and Technology, TU Wien.

Ich danke dem China Scholarship Council für die finanzielle Unterstützung meines Doktoratsstudiums an der TU Wien. Mein besonderer Dank gilt Univ.Prof. Dr. Ernst Kozeschnik, meinem Betreuer, der mir unersetzliche Leitfäden zur Verfügung stellte und mich in den letzten vier Jahren des Studiums und Lebens in Wien enorm inspiriert hat. Mein besonderer Dank gilt auch Ass.Prof. Dr. Erwin Povoden-Karadeniz, der die Fertigstellung dieser Arbeit mit seinen unschätzbaren Anregungen und fruchtbaren Diskussionen unterstützte. Ich danke Tomasz Wojcik und Edith Asiemo für ihre Hilfe bei der EBSD-Probenahme und Messung. Harald Radlwimmer danke ich aufrichtig für die Unterstützung bei der finalen Formatierung dieser Arbeit. Abschließend bedanke ich mich bei allen meinen Kollegen am Institut für Werkstoffwissenschaft und Werkstofftechnologie der TU Wien.

Abstract

A semi-empirical law for twin growth is proposed, which considers the twin volume saturation and initial twin volume fraction after nucleation. This law is in good agreement with the experimental electron back scattered diffraction results of AZ31 Mg alloy. A growth factor is included in the model, which controls the speed of increase of twin volume fraction and its saturation. The underlying physics of this factor. By extracting the common features of assessed physical mechanisms of twin growth, a simple dislocation model of twin thickening is proposed. This model delivers a reasonable estimate of the velocity of a twin partial dislocation, serving as reference or input for dislocation dynamics modeling of twinning. Based on the understanding on the twinning and dislocation slips in Mg, a novel thermomechanical treatment containing a pre-straining step is tested experimentally in AZ31 Mg alloy. Three different pre-strain schemes are attempted and their effectiveness for weakening of the strong basal texture of AZ31 Mg alloy is discussed. It is shown that the <c+a> pyramidal slip promotes the recrystallization process in the subsequent isothermal heat treatment, resulting in significant weakening of the basal texture. Finally, a Taylor type mean field model embedding twin growth and Voce hardening law, is developed. Instead of using the non-linear rate-sensitive constitutive law, *i.e.*, the visco-plasticity formulation, this model provides rapid predictions on the texture evolution of as extruded Mg alloys and delivers relative activities of different deformation modes. The prediction is consistent with the experimental results of AZ31 Mg alloy.

Contents

1 Introduction

Mg exhibits intrinsically strong anisotropy because of its hexagonally close packed (hcp) lattice structure [1, 2]. This anisotropy has profound impacts on its microstructural response to deformation. The anisotropy is closely related to the different activation stresses of various deformation modes including basal slip, pyramidal slip, prismatic slip and deformation twinning. The activation stress is represented by the critical resolved shear stress (CRSS). It can be generalized from the literature that $CRSS_{basal} < CRSS_{twinning} < CRSS_{prismatic} \leq CRSS_{pyramidal}$ [3-7]. The CRSS of different deformation modes suggests that basal slip should be the most easily activated. The earlier studies have also confirmed this statement [8-11]. However, basal slip can only accommodate the plain strain on the basal plane of the hcp lattice. Non-basal slip systems and deformation twinning are required to be activated in the case that the strain tensor has components along the *c* axis. Due to its relatively low CRSS, the tensile twinning $\{10\bar{1}2\}<10\bar{1}1>$ (twinning plane and twinning direction) plays an important role in the deformation of Mg at room temperature. Not only can tensile twinning accommodate the strain components along c axis, but also it exerts significant effects on the texture evolution, *i.e.*, the *c* axis of the matrix lattice is reoriented by tensile twinning $\{10\bar{1}2\}<10\bar{1}1>$ by approximately 86° around the $<10\bar{1}0>$ axis. Furthermore, tensile twinning has a strong impact on work hardening, since it reduces the mean free path of dislocation slip and causes the formation of twin-twin joints. Tensile twinning is prevailing at room temperature deformation [12], and understanding of the mechanisms of twin evolution has thus a high practical relevance. Despite considerable efforts to research the nucleation and growth of twins [13-17], the twin-dislocation interaction at atomic scale [18] and the effects of twinning on work hardening and texture evolution [19-21], a physical law capturing twin growth and associated twin volume fraction has not been established yet. In fact, numerical methods such as Volume Fraction Transfer (VFT) scheme and Predominant Twin Reorientation (PTR) scheme [22] enclose the twin volume fraction and were applied in texture modeling of hcp metals Mg, Zr and Ti, accepting some arbitrariness in the computational parameter selection (*e.g.*, arbitrary threshold value of the twin volume fraction in PTR). The numerical nature of VFT and PTR entail many iterations, associated with high computational cost. In the present thesis, a semi-empirical law on the evolution of twin volume fraction was intended to be proposed. This law considers initial twin volume fraction after nucleation and the twin volume saturation. A growth factor of twin, α, is included, which is required to determine the speed of increase of twin volume fraction and its saturation. A simple dislocation model considering twin thickening is developed. This model is supposed to deliver a reasonable estimate of the velocity of a twin partial dislocation. Since the

physically precise quantitative evaluation of this property is beyond conventional experimental determination, an estimate on its order of magnitude will be a useful reference or input for dislocation dynamics modeling of twinning. It has been shown that the basal texture greatly handicaps deformation ability of Mg alloy. Here, a novel thermal mechanical method will be developed to weaken the strong basal texture. Three pre-strain schemes are attempted experimentally, and their ability to weaken the strong basal texture is discussed.

The orientation distribution of polycrystal grains and its control is a key to innovation and process optimization in industry. All non-random orientation distributions are defined as "texture". Understanding the consequences of relative activity of different deformation modes and associated ratios of CRSS allows for controlling and understanding the deformation response of the material, such as, texture evolution and vice versa. Although transmission electron microscopy (TEM) was applied to clarify the activity of deformation modes [23, 24], explicit and detailed experimental investigation of the relative activity of different deformation modes remains a challenging task. In the framework of virtual materials design, studying the texture evolution and the anisotropic mechanical response of Mg via crystal plasticity [25, 26] has been shown to be an efficient, promising approach, since, the relative activities of different deformation modes can be evaluated at each moment of a deformation setting.

Present texture modeling approaches can be divided into the categories 1) mean field and 2) full field. 1) The full constraints Taylor model (FC model), the relax constraints Taylor model (RC model) [27] and the visco-plasticity self-consistent method (VPSC) are mean field models [22]. VPSC is much more complex than Taylor Type models. Due to its iteration algorithm, it is also computationally costly. Thus, the Taylor Type model may be a suitable choice when it comes about simulative trends of texture evolution, whereas, in fact, VPSC will deliver more accurate numerical simulation results. 2) Crystal plasticity finite element method (CPFEM) represents a full field model [28]. Compared to the mean field models, the full field model indeed delivers additional information to the understanding of texture, like the local stress field. However, high computation expense is needed, and the method does not necessarily give more reliable answers compared to the results of Taylor type model [29]. Further, restrained by the calculation capacities of even high-end computers, the grain number in full field method is limited. In contrast, in the mean field method, more grains (more than 5000) can be considered easily and allow for better statistics.

In the present thesis, a Taylor type model is developed to simulate the texture evolution of the as-extruded AZ31 Mg alloy. The semi-empirical physics law of twin growth is embedded

in this model and the minimum shear principle proposed by Bishop and Hill [30] is applied to select the active slip systems.

2 Objectives

The objectives of this thesis are

1. Establishing a semi-empirical twin growth law. This law should be consistent with the experimental observations, and its simplicity should facilitate its implementation into a texture model.
2. Finding a novel thermal mechanical experimental method to weaken the strong basal texture of the as-extruded AZ31 Mg alloy. Three pre-strain schemes will be tested and their ability of weakening basal texture will be examined.
3. Developing a modified Taylor type model into which a semi-empirical twin growth law is embedded. This model will be applied to simulate the texture evolution of as-extruded AZ31 alloy. The prediction should be consistent with the experimental results of AZ31 Mg alloy. This model should also significantly reduce the calculation time due to its simplicity of mathematical form.

3 State of the art

In this section, the current understanding of deformation of single crystal and polycrystal is presented in Section 3.1 and 3.2. In Section 3.3, the reader is led through relevant pre-requisites for texture modeling, starting with a representation of orientation and texture to the understanding of orientation distribution function (ODF). Deformation modes in Mg and its alloys are presented in Section 3.4. For the purpose of modeling the texture, a basic knowledge on crystal plasticity is required, which is the focus of Section 3.5. Modeling approaches based on crystal plasticity are briefly introduced and compared in Section 3.6, focusing on their usability for modeling the texture evolution.

3.1 Understanding deformation - single crystal

In this section, the state-of-the-art of understanding deformation of a single crystal is discussed, which sets up the basis for the considerations of deformation in polycrystalline material (Section 3.2).

3.1.1 Schmid´s law and generalized Schmid´s law

When a single crystal metal sample is subjected to a uniaxial tensile test, its yield strength will vary with the orientation of the sample. This indicates that yielding of a single crystal is directly related to the activation of its slip systems. The experimental observation has shown that a slip system can be activated when the shear stress acting in the slip direction on the slip plane reaches some critical value. This critical shear value is the stress required to move a dislocations along the slip plane [31].

The yield strength of the single crystal with a certain orientation is calculated as follows. The applied stress in the tensile direction on cross section area A is $\sigma=F/A$, F is the applied force. The resolved shear stress, τ_R, acting along the slip direction on the slip plane then reads

$$\tau_R = \frac{resolved\ \ force\ acting\ along\ the\ slip\ direction}{area\ of\ \ slip\ \ plane} \ . \tag{3.1}$$

The resolved force acting along the slip direction is $F\ cos\ \lambda$, and the area of the slip plane is $A/cos\varphi$, where λ is the angle between the tensile axis and the slip direction and φ is the angle between the tensile axis and the slip plane normal, as shown in Fig. 3.1. τ_R is then given by:

$$\tau_R = \frac{F \cdot cos\lambda}{A/cos\varphi} = \sigma \cdot cos\varphi \cdot cos\lambda \ . \tag{3.2}$$

It is found that the resolved shear stress required to activate a specific slip system in a given material with specified dislocation density and purity is constant. This threshold stress is known

as the critical resolved shear stress (CRSS), τ_c, being different for different slip systems. The Schmid´s law can be expressed as

$$\tau_R = \sigma \cdot cos\varphi \cdot cos\lambda \geq \tau_c \ . \tag{3.3}$$

$cos\varphi \cdot cos\lambda$ is called the *Schmid factor*. Usually, in metals, several slip systems are activated during deformation. It is unlikely that the resolved shear stress acting on each system simultaneously reaches their respective τ_c as the applied tensile stress increases. More probable, for one slip system, τ_c is reached first. This is the primary slip system, whose CRSS is τ_c^p. The activation of the primary slip system marks the start of plastic deformation. The stress required for the activation of the primary slip system is the yield stress of the single crystal, $\sigma_c = \tau_c^p / cos\varphi \cdot cos\lambda$. In the cases where the different slip systems have same τ_c (*e.g.* in the face cantered cubic metals), according to the Schmid's law Eq. (3.3), the primary slip system will be the system with the largest *Schmid factor*.

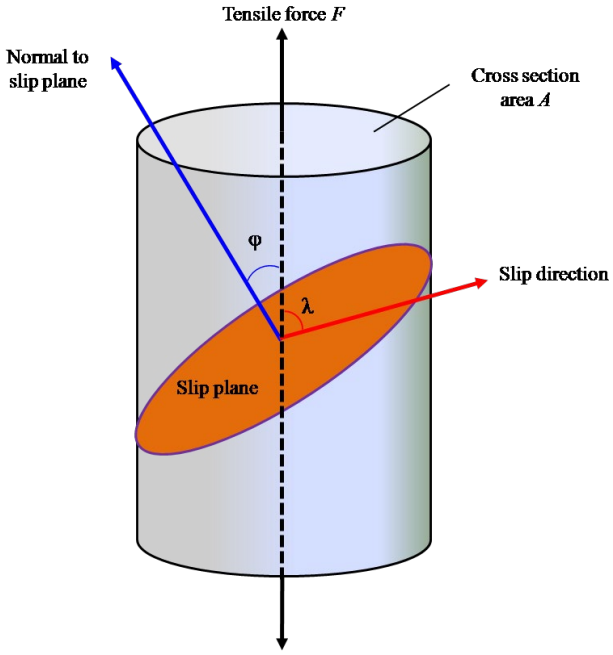

Fig. 3.1. Uniaxial tensile deformation of a single crystal: λ is the angle between the tensile axis and the slip direction; φ is the angle between the tensile axis and the slip plane normal.

When the stress state imposed on the single crystal is complex, the Schmid's law is transmuted to tensor form. Hereby, the unit vector of the slip direction $\mathbf{b}^{(s)}$ and normal to the slip plane $\mathbf{n}^{(s)}$ for a given slip system are written in the sample coordinate frame. $b_i^{(s)}$ is the *i*th component of

unit vector $\mathbf{b}^{(s)}$ in the slip direction in the sample coordinate frame and $n_j^{(s)}$ is the jth component of unit vector $\mathbf{n}^{(s)}$ normal to the slip plane. Then the dyadic product of $\mathbf{b}^{(s)}$ and $\mathbf{n}^{(s)}$ can be defined as $\mathbf{b}^{(s)}\mathbf{n}^{(s)}$, and the symmetric and skew parts of this dyadic can be expressed as:

$$m_{ij}^{(s)} = \frac{1}{2}\left(b_i^{(s)} n_j^{(s)} + b_j^{(s)} n_i^{(s)}\right) , \tag{3.4a}$$

$$\mathbf{m}^{(s)} = \frac{1}{2}\left(\mathbf{b}^{(s)}\mathbf{n}^{(s)} + \mathbf{n}^{(s)}\mathbf{b}^{(s)}\right) , \tag{3.4b}$$

$$q_{ij}^{(s)} = \frac{1}{2}\left(b_i^{(s)} n_j^{(s)} - b_j^{(s)} n_i^{(s)}\right) , \tag{3.5a}$$

$$\mathbf{q}^{(s)} = \frac{1}{2}\left(\mathbf{b}^{(s)}\mathbf{n}^{(s)} - \mathbf{n}^{(s)}\mathbf{b}^{(s)}\right) , \tag{3.5b}$$

where $\mathbf{m}^{(s)}$ is the Taylor tensor and the generalized Schmid´s law can be expressed as

$$\mathbf{m}^{s} : \boldsymbol{\sigma}^{s} = \tau^{s} . \tag{3.6}$$

$\boldsymbol{\tau}^{s}$ is the CRSS for one specific slip system. Its essence is that the component of the applied stress performing the plastic work determines the kinematic behavior [32]. When there is no thermal dissipation, the plastic work done by the macroscopic tensile stress will be equal to that of the micro resolved shear stress.

$$\tau^{s} d\gamma = \sigma d\varepsilon . \tag{3.7}$$

Based on Schmid's law, the shear strain is expressed as

$$d\varepsilon = \cos\varphi \cos\lambda d\gamma . \tag{3.8}$$

For the strain rate, we obtain

$$\dot{\varepsilon} = \cos\varphi \cos\lambda \dot{\gamma} , \tag{3.9}$$

which represents the relationship between macro-strain rate and micro-strain rate in the one dimensional case (*e.g.* the uniaxial tension of a single crystal). However, since the general strain in one grain of a polycrystal (which may be thought of as a "single crystal" in a polycrystal, here) has 6 different components (for it is a tensor), Eq. (3.9) will become a tensor formula. When there are many active slipping systems, all these active slipping systems contribute to the whole deformation, and the strain rate of the single crystal (or one grain in a polycrystal aggregate) can be expressed as

$$\mathbf{D}^{c} = \sum_{s} \dot{\gamma}^{s} \mathbf{m}^{s} . \tag{3.10}$$

$\mathbf{D}^{c}$ is the strain rate tensor of one grain in the polycrystal. Therefore, in a polycrystal aggregates, since the mechanical response of each grain is different also $\mathbf{D}^{c}$ of each grain is different. From the Eq. (3.10), the *direction* of strain rate tensor $\mathbf{D}^{c}$ is determined by the Taylor tensors $\mathbf{m}^{s}$ of

all active slip systems and $\dot{\gamma}^s$ can be seen as the component of the strain tensor $\mathbf{D}^c$ along the Taylor tensors of this slip system. Based on the volume conservation assumption during deformation processes, the strain rate tensor $\mathbf{D}^c$ will have 5 independent components, indicating that 5 independent slip systems are required to accommodate any inhomogeneity during deformation. It is notable that Schmid´s law serves as a corner stone for all kinds of crystal plasticity models.

3.1.2 Orientation change of a single crystal

Fig. 3.2 illustrates a single crystal subjected to tension. Here the resolved shear stress on the slip system reaches the CRSS, *i.e.*, this slip system is activated. If there were no constraints on the end of the sample bar, the tensile axis of the sample would rotate with the normal to the slip plane and the slip direction would remain unchanged. However, usually the end of the tensile axis of the sample is fixed and cannot rotate. Then the crystal orientation will vary and the crystal will suffer a rigid rotation. Assume the unit vectors $\boldsymbol{s}$ and $\boldsymbol{m}$ standing for the slip direction and normal to the slip plane of active slip system. The rotation axis around which slip direction $\boldsymbol{s}$ rotates toward the tensile axis $\boldsymbol{T}$ is then given by

$$\mathbf{r} = \mathbf{s} \times \mathbf{T} \Big/ \left[1 - (\mathbf{s} \times \mathbf{T})^2 \right]^{1/2} , \tag{3.11}$$

where $\boldsymbol{r}$ is the unit vector and $\boldsymbol{T}$ is the unit vector along axis. The change rate of $\mathbf{s}$ and $\mathbf{m}$ can be expressed as $\dot{\boldsymbol{s}}$ and $\dot{\boldsymbol{m}}$ [33]

$$\dot{\boldsymbol{s}} = \boldsymbol{\Omega}^* \cdot \boldsymbol{s} , \tag{3.12}$$

$$\dot{\boldsymbol{m}} = \boldsymbol{\Omega}^* \cdot \boldsymbol{m} , \tag{3.13}$$

$$\boldsymbol{\Omega}^* = -\dot{\gamma} \left(\boldsymbol{sT} - \boldsymbol{TS} \right) \boldsymbol{T} \cdot \boldsymbol{m} , \tag{3.14}$$

where $\boldsymbol{\Omega}^*$ is the rigid lattice spin rate. Eq. (3.14) will be applied in Section 6.1.

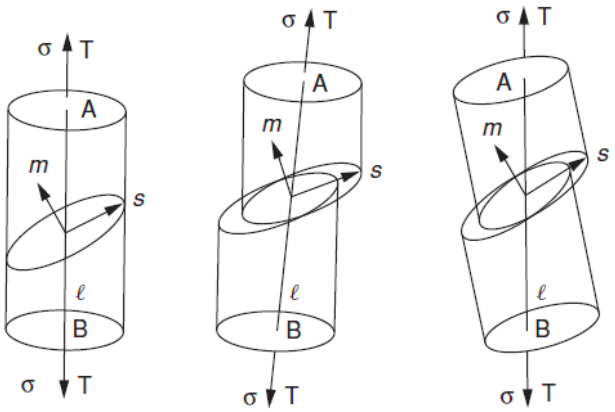

Fig. 3.2. Schematic diagrams for a single crystal undergoing single slip in tension [33].

In the case of a uniaxial tension test of a single crystal, assuming the instantaneous hardening rate is h, the tensile stress rate $\dot{\sigma}$ evolves with the tensile strain rate (the true strain rate) $\dot{e}$ as

$$\dot{\sigma} = M\dot{\varepsilon} \ , \tag{3.15}$$

and

$$M = \frac{h}{\cos^2 \Phi \cos^2 \theta} + \frac{\sigma \cdot \cos(2\Phi)}{\cos^2 \Phi} \ . \tag{3.16}$$

The first term of Eq. (3.16) represents the work hardening effects, while the second term of Eq. (3.16) is related to geometrical softening. During the tensile test, the orientation of single crystal will change. When the change of the orientation of single crystal makes the required tensile stress decrease, single crystal appears to become soft with deformation. This phenomenon is called geometrical softening, which is exclusively caused by the rotation of the crystal. Geometrical softening happens locally, which can be ascribed to the inhomogeneous dislocation distribution and the non-uniform deformation [33]. Eq. (3.16) allows for the competition between work hardening and geometrical hardening. When M becomes negative, geometrical softening outweighs the work hardening and the crystal softens.

3.1.3 Stages in the τ-γ curves of a single crystal

The proposal of different stages of strain hardening in stress–strain curves marks a major benchmark in the evolution of strain-hardening theory [34]. Experiments of single crystals have demonstrated the existence of a number of different stages of strain hardening, which are introduced here in short.

Stage I is initiated by the motion of a single slip system, which strongly depends on the orientation of the crystal and does not occur if the deformation is initialized by multiple slip from the beginning. Stage II exhibits the largest hardening rate, whose magnitude is of 1/200 of the shear modulus μ. The hardening rate in Stage II depends on orientation as well, while it is insensitive to strain rate or material compositions. The work hardening rate in stage III exhibits a decreasing trend and it is very sensitive to temperature and the rate of deformation. Stage III has been shown to depend strongly on the type of material, indicating the stacking fault energy (SFE), which itself is strongly material-dependent, plays an important role in this stage. The presence of stage III confines the extent of stage II, especially at high temperatures and for materials with high SFE. Fig. 3.3 illustrates the shear stress versus shear strain curves (τ-γ) for single crystals with different orientations in 99.98% Cu at room temperature and an initial shear strain rate of 2×10^{-3}/s [34].

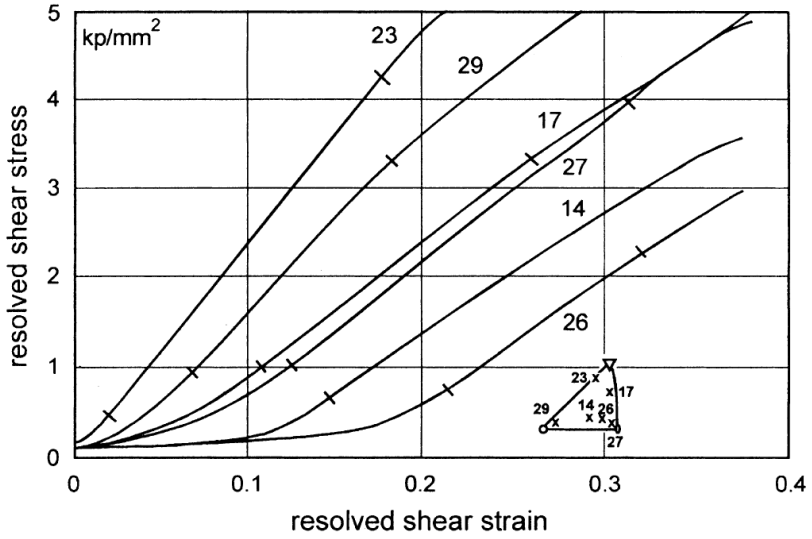

Fig. 3.3. Resolved shear stress – resolved shear strain curves of 99.98% Cu single crystals with various orientations at room temperature and an initial shear strain rate of 10^{-3}/s (The beginning and end of stage II are marked) [34].

3.2 Deformation of polycrystals

3.2.1 Experimental observations

Fig. 3.4 (a) shows the optical micrograph of deformed polycrystalline lead. The observed plastic deformation caused by simple shearing is a local feature. Formation of slip-steps (Fig. 3.4 (b)) was explained by sliding of certain families of crystal planes over each other in certain crystallographic directions lying in the planes

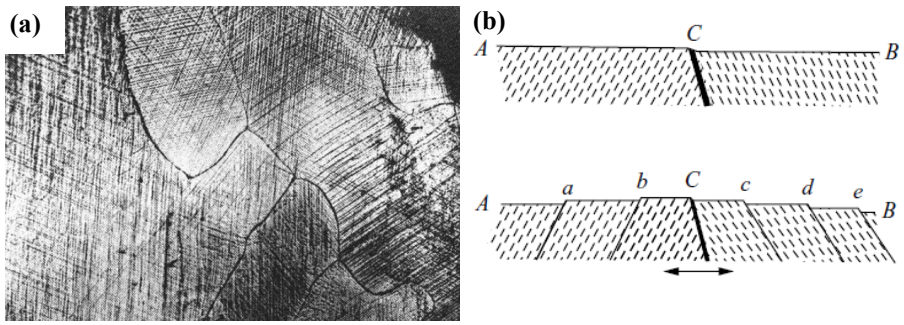

Fig. 3.4. Observation of slip lines in polycrystalline Pb (a); and (b) the schematic representation of slip-steps [35].

Fig. 3.4 (b) illustrates the “slip-steps” caused by the emergence of “slip bands”, which formed along crystallographic planes, at the specimen surfaces. The dashed lines indicate the traces of the crystalline slip planes and the bold line C represents a grain boundary separating

two grains. Nowadays, it can be verified by transmission electron microscopy that, in microscale, the dislocations were stored on the slipping planes.

3.2.2 Stages in σ-ε curves of polycrystals

Fig. 3.5 illustrates a set of stress-strain curves in Cu fcc polycrystals at different temperatures. The starting stage of all of these curves exhibit the same constant slope, which is similar to stage II in single crystals, while stage I is absent in polycrystals, indicating that deformation is initiated by the simultaneous activation of multiple slip systems. Further studies have shown that other fcc metals also have a similar linear strain hardening stage. Moreover, stage II in polycrystals is almost insensitive to the deformation temperature. The hardening rate in stage II is of the magnitude of 1/50 of Young's modulus *E*. Stage II and associated multi-slip behavior is restricted to the low-strain range. The commencement of stage III is characterized by the strong dependence on temperature, strain rate and material composition. There is also a stage IV in the high-strain range of the stress-strain curves for metals with a low hardening rate. This stage can be considered as an asymptote for high strains, and stage II can be seen as an asymptote for low strain [34].

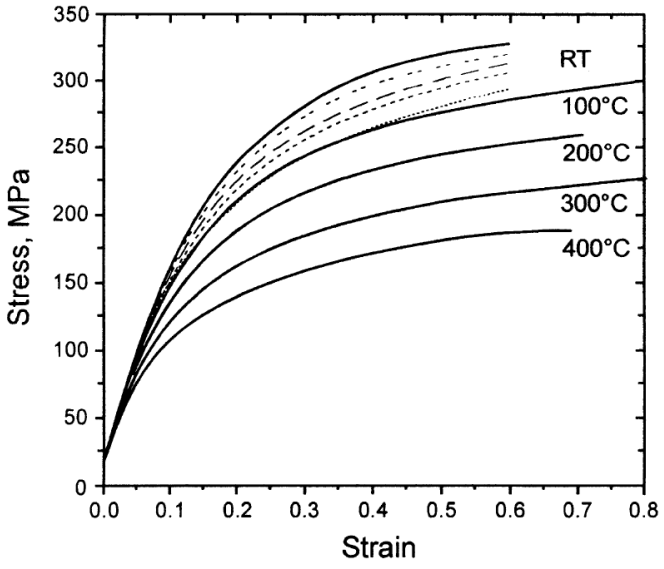

Fig. 3.5. Compressive stress-strain curves for Cu polycrystals at different temperature. The strain rate is 1 s^{-1} for all solid curves [34].

Fig. 3.6 shows tension and compression responses of rolled AZ31 alloy sheets at the strain rate of 10^{-2} s^{-1} at different temperatures of 25 °C, 65 °C and 150 °C [36]. The uniaxial tension, compression tests were performed in different directions: along rolling direction (RD);

transverse to rolling direction (TD); along normal direction (ND); and 45º to rolling direction (DD).

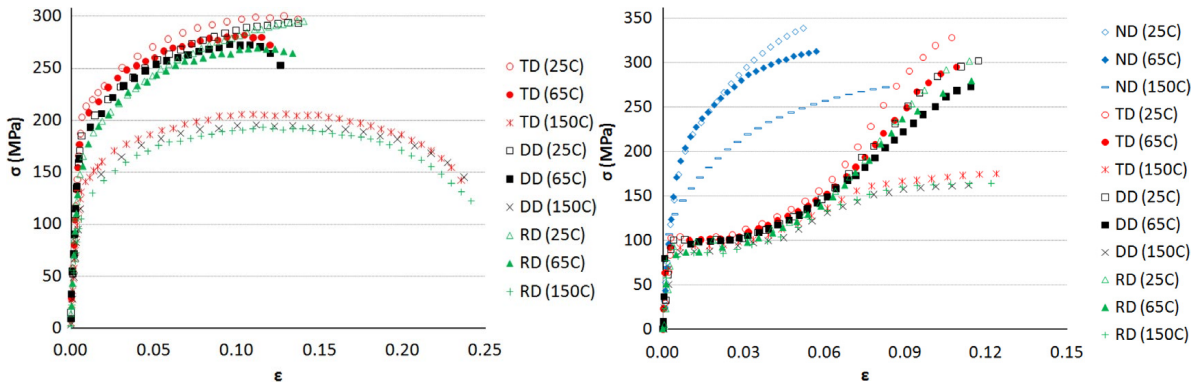

Fig. 3.6. Tension (a) and compression(b) responses of rolled AZ31 alloy sheets at a strain rate of 10^{-2} s^{-1} at different temperatures and directions [36].

The tension response of the rolled, polycrystalline AZ31 Mg alloy, as shown in Fig. 3.6 (a), is similar to the curves shown in Fig. 3.5. However, as shown in Fig. 3.6 (b), the compression of rolled AZ31 Mg alloys displays the flow curves with very different shapes, which cannot be simply divided to 3 stages as in the fcc metals. The shape differences between the compressive flow curves are strongly related to the deformation twinning [36], which is absent in the case of Cu polycrystal compression.

3.2.3 Work hardening

Work hardening or strain hardening primarily originates from interactions of the following material defects interactions, 1) dislocation-dislocation, 2) twin-dislocation and 3) twin-twin.

1) dislocation-dislocation interaction: As deformation goes on, dislocations multiply and interact mutually[37]. Due to this dislocation-dislocation interaction, the stress needed for activation of dislocation movement and initiation of plastic deformation [38, 39] increases. Bassani and Wu [40] proposed a simple strain rate-independent phenomenological hardening formulation:

$$\dot{\tau}_c^{(\alpha)} = \sum_{\beta} h_{\alpha\beta}\dot{\gamma}^{(\beta)} \ , \tag{3.17}$$

$$h_{\alpha\alpha} = \left[\left(h_0 - h_s\right)\operatorname{sech}^2\left(\frac{\left(h_0 - h_s\right)\gamma_\alpha}{\tau_1 - \tau_0}\right) + h_s\right]\left[1 + \sum_{\substack{\beta=1 \\ \beta\neq\alpha}}^{N} f_{\alpha\beta}\tanh\left(\frac{\gamma_\beta}{\gamma_0}\right)\right], \tag{3.18a}$$

$$h_{\beta\alpha} = q h_{\alpha\alpha}, \alpha \neq \beta \ . \tag{3.18b}$$

where $\tau_c^{(\alpha)}$ is the current yield strength on the α slip system, and $h_{\alpha\beta}$ are the hardening rates. The off-diagonal terms in the matrix represent latent hardening. Latent hardening refers to the influence of the active slip systems on hardening of the inactive slip systems. $f_{\alpha\beta}$ is the amplitude factor, which depends on the type of dislocation junction [40] formed between slip system α and β. γ_0 is the amount of slip after which the interaction between slip system α and β reaches peak strength (generally, γ_0 is assumed to be the same for all pairs of systems). τ_0 is the initial critical resolved shear stress, τ_I is the stage I stress (or the breakthrough stress where large plastic flow initiates). h_0 is the hardening modulus just after initial yield, and h_s is the hardening modulus during easy glide. q is the ratio of the latent and self-hardening rate.

In constitutive laws, an extended Taylor's law is usually applied to capture the effects of dislocation-dislocation interactions on CRSS, which relates the CRSS on a given system to the total dislocation densities on all slip systems. This approach yields proper results when the hardening in stage III is mainly controlled by the increasing dislocations density. However, the softening of flow stress due to annihilation of dislocations can be frequently observed, such as during deformation of Aluminum. This process is called dynamic recovery. In order to account for differing strengths due to dislocation–dislocation interactions and varying influence of dislocation interactions on hardening, Franciosi and Zaoui proposed an interaction matrix and the following expression for defining the CRSS on a slip system [41]:

$$\tau_c^{\mathrm{s}} = \tau_0^{\mathrm{s}} + \mu^s b^s \sqrt{\sum_{s'} \alpha_{FZ}^{ss'} \rho^{s'}} \ , \tag{3.19}$$

where τ_c^{s} is the CRSS and τ_0^{s} is the lattice friction stress on the slip system s, respectively. μ^s and b^s are the shear modulus and magnitude of Burgers vector of this slip system. $\alpha_{FZ}^{ss'}$ is the interaction coefficient related to the strength of the interaction between dislocation slip systems s and s'. Then, an interaction matrix can be established by $\alpha_{FZ}^{ss'}$. $\rho^{s'}$ denotes the dislocation density of system s'. The dislocation system s, on which the CRSS is evaluated, is generally referred to as the primary system, while the other slip systems s' are referred to as forest systems (which might be inactive at a specific deformation increment) with respect to s. It should be noted that the *FZ* formulation was originally proposed for fcc materials where the magnitude of the Burgers vector of different slip systems is identical. In hcp metals, the magnitude of the Burgers vector of different slip system is different, and dislocation mobility and friction stress associated with hcp slip systems are expected to yield a non-symmetrical latent hardening

matrix. The work hardening behavior in hcp metals will thus be different from that of fcc metals. A proper hardening law for hcp materials has been proposed by Lavrentev and Pokhil [42]:

$$\tau_c^{\mathrm{s}} = \tau_0^{\mathrm{s}} + \sum_{s'} \mu^{s'} b^{s'} \alpha_{LP}^{ss'} \sqrt{\rho^{s'}} \quad , \tag{3.20}$$

This formulation also contains τ_c^{s} and τ_0^{s}, and μ^s and b^s are again the shear modulus and magnitude of Burgers vector of the *s'* slip system. Now, $\alpha_{LP}^{ss'}$ is the interaction coefficient related to the strength of the interaction between dislocation slip systems s and s'. The numerical values of the FZ of Eq. 3.19) and LP coefficients of Eq. (3.20) are not expected to coincide. Obviously, the FZ and LP expressions of the hardening law differ by two aspects: (1) the position of the summation symbol and (2) the Burgers vector of the primary slip system enters the FZ formulation while Burgers vector associated with the forest slip systems is inserted in the LP expression.

2) twin-dislocation interactions: It was found that the dislocation transmutation was irreversible and resulted in the presence of a larger number and a higher fraction of various dislocation types within the twinned regions than in the parent, forcing them to interact and induce an increasing latent hardening unique for twinning [43]. The interaction matrix, in principle, defines both, the flow stress and the hardening rate.

Research on the influence of twin-dislocation interaction on work hardening is scarce, and studying the role of twin-dislocation interaction is an unsolved task.

However, the frequently applied Voce type hardening law [44-47] considers twin-dislocation interactions phenomenologically by the hardening matrix $h_{ss'}$, being found in the rate Eq. (3.21b) of the work hardening formulations:

$$\hat{\tau}^s = \tau_0^{\mathrm{s}} + \left(\tau_1^{\mathrm{s}} + \theta_1^{\mathrm{s}}\Gamma\right)\left[1 - \exp\left(-\frac{\theta_0^{\mathrm{s}}\Gamma}{\tau_1^{\mathrm{s}}}\right)\right] , \tag{3.21a}$$

$$\dot{\tau}^s = \frac{d\hat{\tau}^s}{d\Gamma} \sum_{s'} h_{ss'} \dot{\gamma}^{s'} \quad , \tag{3.21b}$$

where Γ is the total accumulated shear in the grain by summing over all the slip and twinning systems. $\hat{\tau}^s$ is the reference stress. τ_0^{s} is the initial CRSS of slip system "*s*". τ_1^{s} is the back extrapolated CRSS. θ_0^{s} is the initial hardening rate and θ_1^{s} is the asymptotic hardening rate. $\dot{\gamma}^{s'}$ is the shear rate of the slip system. $h_{ss'}$ represents the components of the hardening matrix. When $h_{ss'}$=1, the "self" and "latent" hardening are indistinguishable and the evolution of threshold stress of each slip system is only given by the reference hardening function $\hat{\tau}^s$. In

the present thesis, the Voce type hardening law is applied in the texture model presented in Chapter 6.

3) twin-twin interactions: Twin-twin interactions in fact represent important microstructural features since they contribute to mechanical hardening in mechanical deformation. Twin-twin junctions resulting from twin–twin interactions can retard the detwinning process and thus impede the stress relaxation and promote the nucleation of new tensile twins [48-50]. The retardation behavior has been ascribed to the (unfavorable) dissociation of twin–twin boundary (TTB) dislocations [51]. However, the systematic research on the effects of twin-twin interaction on the work hardening is still missing.

3.3 Representation of orientation and texture

3.3.1 Representation of orientation

Orientation is used in materials science for a complete relation between two coordinate frames, *i.e.*, the crystal coordinate system and sample coordinate system [52]. In general, there are several ways to represent the relation between these two coordinate frames. The most commonly used method is adopting a *rotation* from one frame to another. Given two orthogonal coordinate frames, one orthogonal coordinate frame can be transformed into the other by a sequence of rotations and *vice versa*. The Euler angle is used to unambiguously define this rotation. There are several different, but equivalent definitions of Euler angle. In the following, these definitions are reviewed, and their differences are clarified.

1) Kocks definition. This definition implies the advantage of symmetry and leads to symmetric Euler angles.

We denote the sample coordinate system (SC) by *X*-*Y*-*Z* coordinates and the crystal coordinate system (CC) by *1*-*2*-*3* coordinates. Both coordinate systems are presumed to have right-handedness. The SC is set to be fixed in a unit sphere with the *Z* axis coinciding with the North Pole and the *X* axis lying in the prime meridian line, as depicted in Fig. 3.7. A notional *boat* on the surface of the sphere represents a specific coordinate system with its heading direction being the 1 axis and its mast direction being the 3 axis. The transformation from SC to CC can be well explained by using an analogue of moving the *red* boat (SC) to the *purple* boat (CC) in Fig. 3.7 through a sequence of rotations. The red boat initially experiences a rotation of Ψ around the 3 axis with the rotation direction from the 1 to the 2 axis thus transforming to the orange boat. Then the orange boat moves along the meridian line (orange) to its new position with the azimuthal angel of θ, which is equivalent to the rotation around its 2 axis by θ from 3 to 1. Now, the orange boat's mast is located along its final direction (3 axis).

The last step is to rotate the orange boat around its 3 axis by π-Φ from the 1 to the 2 axis. The orange boat now exactly coincides with the purple boat, which means SC has been transformed to CC. It is interesting that the transformation from CC to SC is just needed to interchange Ψ and Φ. That is why the Kocks definition is called symmetric Euler angles.

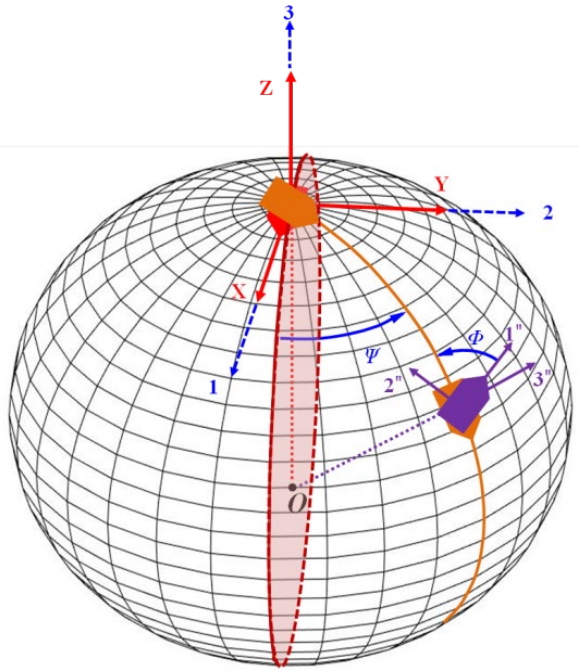

Fig. 3.7. Schematic representation of definition of Euler angles as spherical coordinates for a boat on the surface of a unit sphere (Kocks).

Here, one question emerges, *i.e.*, what is the rule governing the transformation between the components of one vector or tensor in SC and its components in CC. Mathematically, a rotation manipulation can be described by a rotation matrix $\boldsymbol{Q}$. In order to deduce the transformation matrix from SC to CC, the rotation manipulation displayed in Fig. 3.7 is represented in the orthogonal coordinate systems in Fig. 3.8, where the red coordinate systems is denoted as SC and the purple coordinate systems is CC. After three successive rotations, the SC is completely transformed to CC. Given a vector $\boldsymbol{v}$, its contra-variant components in the old coordinate system A and the new coordinate system B are $(v^1,v^2,v^3)^{\mathrm{T}}$ and $(v^{1\prime},v^{2\prime},v^{3\prime})^{\mathrm{T}}$, respectively. The covariant base vectors of the new coordinate system $B(\mathbf{b_1}, \mathbf{b_2}, \mathbf{b_3})$ can be expressed by that of the old coordinate system $A(\mathbf{a_1}, \mathbf{a_2}, \mathbf{a_3})$ by equation:

$$\begin{pmatrix} \mathbf{b}_1 \\ \mathbf{b}_2 \\ \mathbf{b}_3 \end{pmatrix} = \begin{bmatrix} l_1^1 & l_1^2 & l_1^3 \\ l_2^1 & l_2^2 & l_2^3 \\ l_3^1 & l_3^2 & l_3^3 \end{bmatrix} \begin{pmatrix} \mathbf{a}_1 \\ \mathbf{a}_2 \\ \mathbf{a}_3 \end{pmatrix}, \tag{3.22a}$$

then $(v^{1'},v^{2'},v^{3'})^{\mathrm{T}}$ can be expressed by $(v^1,v^2,v^3)^{\mathrm{T}}$ as:

$$\begin{pmatrix} v^{1'} \\ v^{2'} \\ v^{3'} \end{pmatrix} = \begin{bmatrix} l_1^1 & l_1^2 & l_1^3 \\ l_2^1 & l_2^2 & l_2^3 \\ l_3^1 & l_3^2 & l_3^3 \end{bmatrix}^{-T} \begin{pmatrix} v^1 \\ v^2 \\ v^3 \end{pmatrix} \tag{3.22b}$$

When the old coordinate system *A* transforms to the new coordinate system *B via* a rigid rotation, $\boldsymbol{Q}=\begin{bmatrix} l_1^1 & l_1^2 & l_1^3 \\ l_2^1 & l_2^2 & l_2^3 \\ l_3^1 & l_3^2 & l_3^3 \end{bmatrix}$ will be an orthogonal matrix, meaning $\boldsymbol{QQ^T=Q^TQ=I}$, and Eq. (3.22b) can be simplified as:

$$\begin{pmatrix} v^{1'} \\ v^{2'} \\ v^{3'} \end{pmatrix} = \begin{bmatrix} l_1^1 & l_1^2 & l_1^3 \\ l_2^1 & l_2^2 & l_2^3 \\ l_3^1 & l_3^2 & l_3^3 \end{bmatrix} \begin{pmatrix} v^1 \\ v^2 \\ v^3 \end{pmatrix}. \tag{3.23}$$

In the rotation manipulation of coordinate system defined by Kocks, the rotation matrix for the first rotation manipulation (Fig 3.8a) can be expressed as:

$$\boldsymbol{Q}_1 = \begin{bmatrix} \cos\Psi & \sin\Psi & 0 \\ -\sin\Psi & \cos\Psi & 0 \\ 0 & 0 & 1 \end{bmatrix}. \tag{3.24}$$

The rotation matrix for the second rotation manipulation (Fig 3.8b) can be expressed as:

$$\boldsymbol{Q}_2 = \begin{bmatrix} \cos\theta & 0 & -\sin\theta \\ 0 & 1 & 0 \\ \sin\theta & 0 & \cos\theta \end{bmatrix}. \tag{3.25}$$

The rotation matrix for third rotation manipulation (Fig 3.8c) can be expressed as:

$$\boldsymbol{Q}_3 = \begin{bmatrix} \cos(\pi-\Phi) & \sin(\pi-\Phi) & 0 \\ -\sin(\pi-\Phi) & \cos(\pi-\Phi) & 0 \\ 0 & 0 & 1 \end{bmatrix}. \tag{3.26}$$

The transformation matrix from SC to CC can be finally expressed by

$$\boldsymbol{g} = \boldsymbol{Q}_3\boldsymbol{Q}_2\boldsymbol{Q}_1 , \tag{3.27}$$

and

$$\boldsymbol{g} = \begin{bmatrix} -\sin\Phi\sin\Psi-\cos\Phi\cos\Psi\cos\theta & \sin\Phi\cos\Psi-\cos\Phi\sin\Psi\cos\theta & \cos\Phi\sin\theta \\ \cos\Phi\cos\Psi-\sin\Phi\cos\Psi\cos\theta & -\cos\Phi\cos\Psi-\sin\Phi\sin\Psi\cos\theta & \sin\Phi\sin\theta \\ \cos\Psi\sin\theta & \sin\Psi\sin\theta & \cos\theta \end{bmatrix} \tag{3.28}$$

As previously discussed, the Kocks definition of Euler angles has an advantage of symmetry. Interchanging Ψ and Φ, we obtain $\boldsymbol{g}^{\mathrm{T}}$. This represents the reverse manipulation transforming CC to SC since $\boldsymbol{g^{T}g=I}$, which can be easily understood from Fig. 3.7. In the stereotype projection, the Kocks definition is shown in Fig. 3.9.

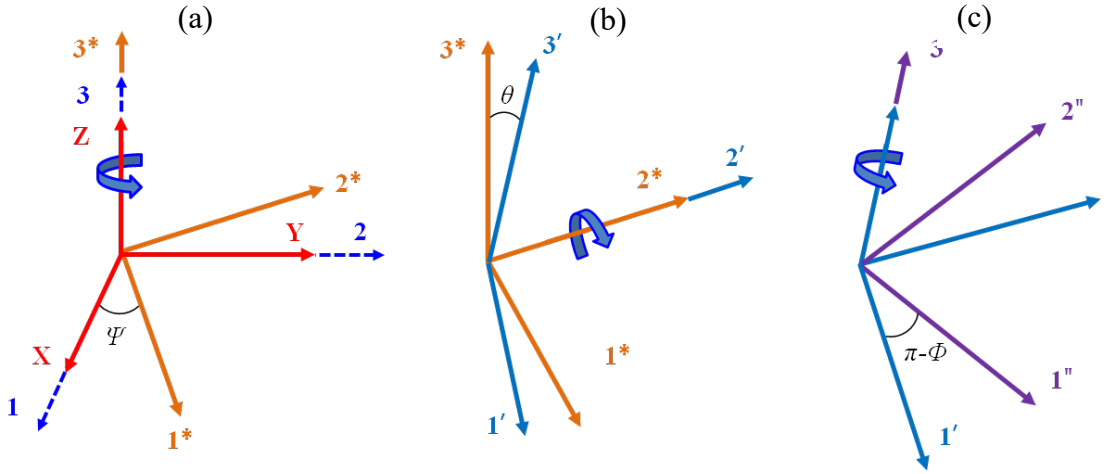

Fig. 3.8. Rotation manipulations based on Kocks definition of Euler angles.

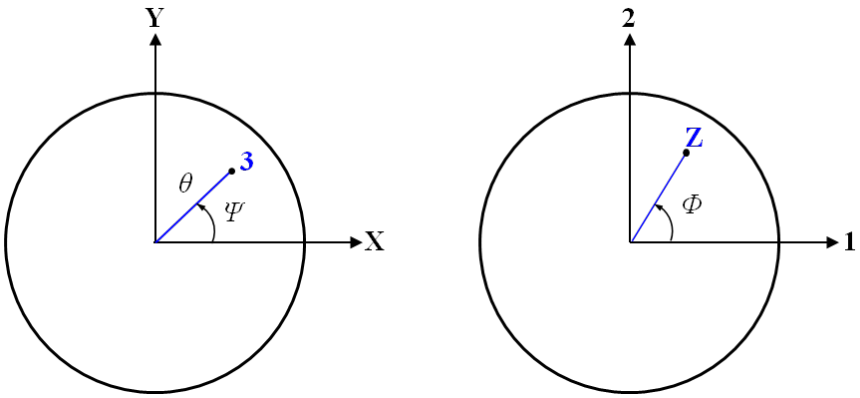

Fig. 3.9. Kocks definition of Euler angles in sample and crystal coordinates.

2) The Bunge definition: Euler angles are expressed as (φ_1,Φ,φ_2), which is shown in Fig. 3.10, where the red coordinate systems is denoted as SC and the purple coordinate system is CC. In terms of the Bunge definition, the transformation matrix from SC to CC can also be decomposed as a series of successive rotation manipulations, as depicted in Fig. 3.10.

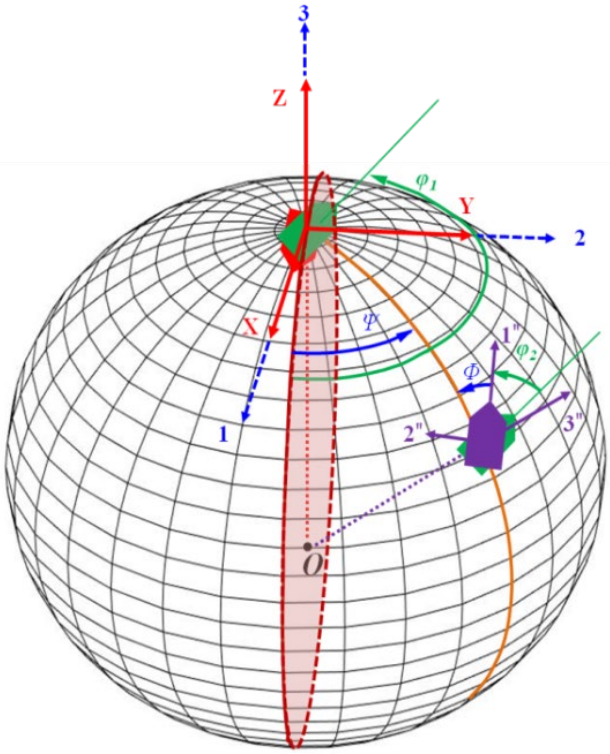

Fig. 3.10. Bunge definition of Euler angles as spherical coordinates for a boat on the surface of unit sphere.

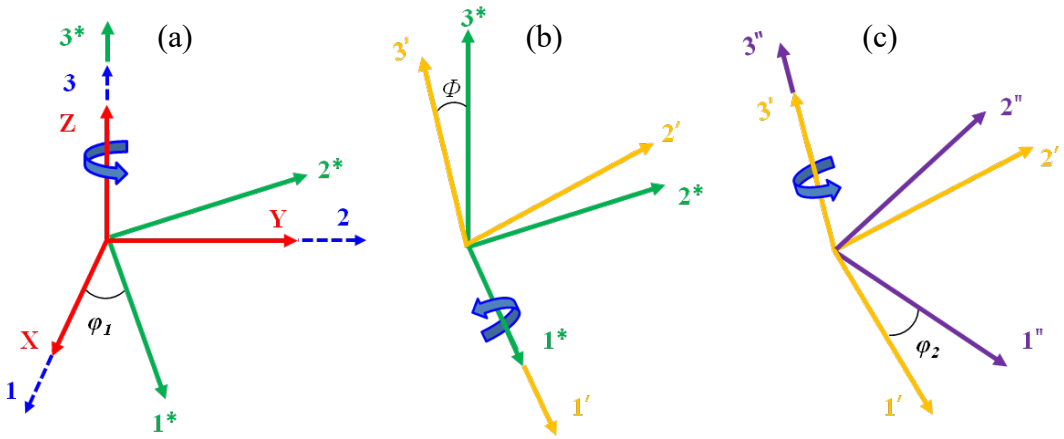

Fig. 3.11. Rotation manipulations based on the Bunge definition of Euler angles.

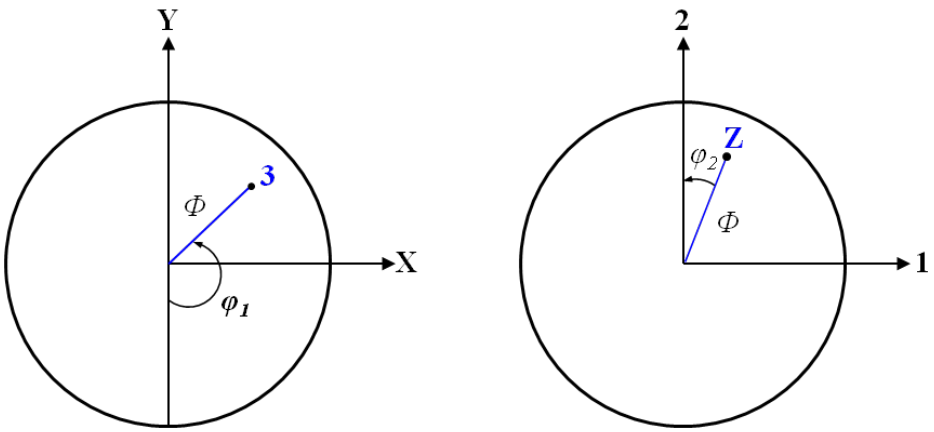

Fig. 3.12. Bunge definition of Euler angles in sample and crystal coordinates.

In the rotation manipulations of coordinate system defined by Bunge, the rotation matrix for the first rotation manipulation (Fig 3.11 (a)) can be expressed as:

$$\boldsymbol{R}_1 = \begin{bmatrix} \cos\varphi_1 & \sin\varphi_1 & 0 \\ -\sin\varphi_1 & \cos\varphi_1 & 0 \\ 0 & 0 & 1 \end{bmatrix}. \tag{3.29}$$

The rotation matrix for second rotation manipulation (Fig. 3.11 (b)) can be expressed as:

$$\boldsymbol{R}_2 = \begin{bmatrix} 1 & 0 & 0 \\ 0 & \cos\Phi & \sin\Phi \\ 0 & -\sin\Phi & \cos\Phi \end{bmatrix}. \tag{3.30}$$

The rotation matrix for third rotation manipulation (Fig. 3.11 (c)) can be expressed as:

$$\boldsymbol{R}_3 = \begin{bmatrix} \cos\varphi_2 & \sin\varphi_2 & 0 \\ -\sin\varphi_2 & \cos\varphi_2 & 0 \\ 0 & 0 & 1 \end{bmatrix}. \tag{3.31}$$

The transformation matrix from SC to CC can be finally expressed by

$$\boldsymbol{g}' = \boldsymbol{R}_3\boldsymbol{R}_2\boldsymbol{R}_1 \ . \tag{3.32a}$$

and

$$\boldsymbol{g}' = \begin{bmatrix} \cos\varphi_1\cos\varphi_2 - \sin\varphi_1\sin\varphi_2\cos\Phi & \sin\varphi_1\cos\varphi_2 + \cos\varphi_1\sin\varphi_2\cos\Phi & \sin\varphi_2\sin\Phi \\ -\cos\varphi_1\sin\varphi_2 - \sin\varphi_1\cos\varphi_2\cos\Phi & -\sin\varphi_1\sin\varphi_2 + \cos\varphi_1\cos\varphi_2\cos\Phi & \cos\varphi_2\sin\Phi \\ \sin\varphi_1\sin\Phi & -\cos\varphi_1\sin\Phi & \cos\Phi \end{bmatrix}. \tag{3.32b}$$

Relations between Kocks definition and Bunge definition of Euler angles are obvious by comparing Fig. 3.9 with Fig. 3.12, where $\Psi=\varphi_1-\pi/2$, $\theta=\Phi$, $\Phi=\pi/2-\varphi_2$, giving rise to $\boldsymbol{g}=\boldsymbol{g}'$, which means the same orientation is obtained.

3.4.2 Orientation space

From the definition of the Euler angles described in Section 3.4.1, it follows that they are periodic with the period of 2π. Then the following equation holds:

$$g\{\varphi_1+2\pi,\Phi+2\pi,\varphi_2+2\pi\}=g\{\varphi_1,\Phi,\varphi_2\}\ . \tag{3.33}$$

All possible Euler angles of one crystal form a space, which is called *orientation space*. From Eq. (3.33), the orientation space is a three dimensional periodic space with period 2π in three coordinate axis directions in a Cartesian coordinate system. The unit cell of orientation space $\{\varphi_1, \Phi, \varphi_2\}$ is $\{2\pi, 2\pi, 2\pi\}$. From the Bunge definition of Euler angles, the following relation is also valid:

$$g\{\varphi_1+\pi,2\pi-\Phi,\varphi_2+\pi\}=g\{\varphi_1,\Phi,\varphi_2\}\ . \tag{3.34}$$

If we input an Euler angles set $\{\varphi_1+\pi, 2\pi-\Phi, \varphi_2+\pi\}$ into Eq. (3.32), we find that the resulting transformation matrix is just the same as if we input an Euler angles set $\{\varphi_1, \Phi, \varphi_2\}$. Actually, this relation corresponds to an operation of reflection with plane Φ=π, plus a simultaneous displacement by π along the axes φ_1 and φ_2, which is schematically represented by Fig. 3.13. Therefore, the asymmetric unit cell can be expressed as $\{2\pi, \pi, 2\pi\}$, which is equivalent to the unit cell and thus can represent all possible Euler angle sets. This symmetry corresponds to a space group P_n in orientation space.

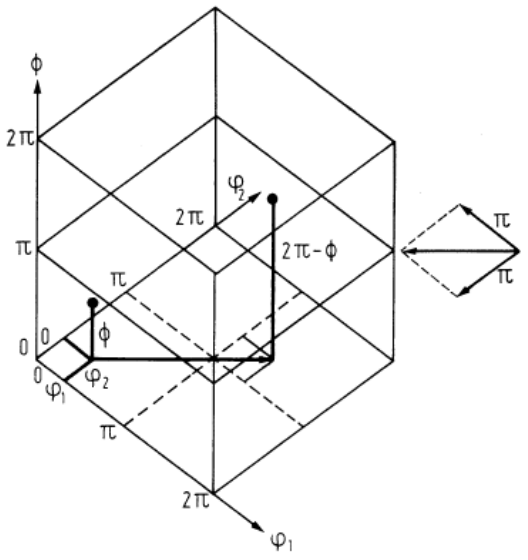

Fig. 3.13. Unit cell and asymmetric unit in orientation space [53].

Conventionally, to represent a crystal orientation, we can start from a coordinate system, which coincides with the SC and then rotate this coordinate system by $\boldsymbol{g}$ to make this coordinate system coincide with the CC. Thus, $\boldsymbol{g}$ is the representation of crystal orientation. However, it is not necessary to start from the coordinate system coinciding with the SC. We can also begin with an arbitrary coordinate system whose orientation is $\boldsymbol{g}_0$ in terms of SC and after the rotation $\boldsymbol{g}'$, this coordinate system coincides with the final CC. Hence, the relation between these two descriptions can be expressed as $\boldsymbol{g} = \boldsymbol{g}' \cdot \boldsymbol{g}_0$. This equation represents a transformation in two orientation spaces. For a specific orientation $\boldsymbol{g}$, it can be expressed by a point with the coordinate $\{\varphi_1, \Phi, \varphi_2\}$ in orientation spaces s, while it can also be expressed by a point with the coordinate $\{\varphi'_1, \Phi', \varphi'_2\}$ in orientation spaces s'. However, if we consider the volume element $d\varphi_1 d\Phi d\varphi_1$ in the vicinity of point $\{\varphi_1, \Phi, \varphi_2\}$, generally, this volume is not equal to the corresponding volume element $d\varphi'_1 d\Phi' d\varphi'_2$ in the vicinity of point $\{\varphi'_1, \Phi', \varphi'_2\}$. Because of the volume distortion involved in this transformation, we introduce an invariant parameter $I(\varphi_1, \Phi, \varphi_2)$ to make the volume of orientation space unchanged after transformation. Thus, the following relation holds:

$$I\left(\varphi'_1, \Phi', \varphi'_2\right) d\varphi'_1 d\Phi' d\varphi'_2 = I\left(\varphi_1, \Phi, \varphi_2\right) d\varphi_1 d\Phi d\varphi_2 \ . \tag{3.35}$$

For Euler angles, the invariant parameter $I(\varphi_1, \Phi, \varphi_2) = \sin\Phi$. With the help of a random orientation distribution, the invariant parameter $I(\varphi_1, \Phi, \varphi_2)$ can be defined as the number of orientation points falling into the volume element $d\varphi_1 d\Phi d\varphi_1$:

$$I\left(\varphi_1, \Phi, \varphi_2\right) = \frac{dn}{d\varphi_1 d\Phi d\varphi_2} \ . \tag{3.36}$$

There is another way to understand the physical meaning of the invariant parameter $I(\varphi_1, \Phi, \varphi_2)$. As can be seen in Fig. 3.14, in a *unit* sphere, this random orientation distribution can be represented by a homogeneous radiation from the center point of the sphere, and each ray vector can be considered as the "z" axis of the crystal coordinate system.

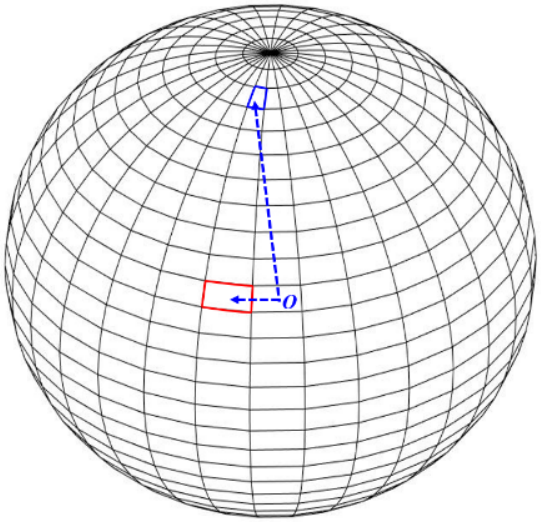

Fig. 3.14. Random orientation distribution can be represented by a homogeneous radiation.

At a different point on the spherical surface, in general, the same $\Delta\varphi_1$ and $\Delta\Phi$ cannot assure that the same number of ray vectors penetrate the surface area element. Apparently, as Φ approaches $\pi/2$, more ray vectors will pass through the surface area element. As a consequence, in orientation space, the density where Φ near to $\pi/2$ will be bigger than that in other parts of orientation space. The area element on the spherical surface can be expressed as $dS=\sin\Phi d\Phi d\varphi_1$ (Fig. 3.15a). When dS is the same, then the same number of ray vectors will pass through dS, which means that the density in orientation space is homogenous (Fig. 3.15b).

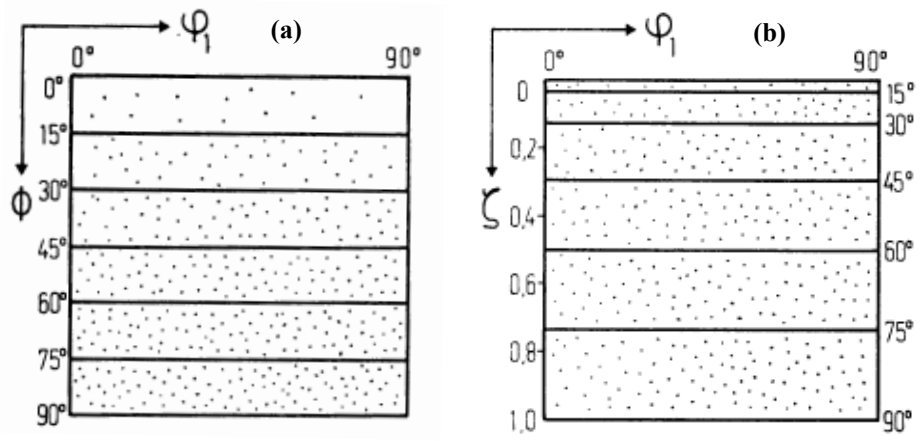

Fig. 3.15. (a) The definition of invariant parameter I (φ_1, Φ, φ_2) by random orientation distribution in orientation space; (b) definition of invariant parameter I (φ_1, ζ, φ_2) [50].

Indeed, dS is exactly the definition of the solid angle $d\Omega$. The same $d\Omega$ guarantees for the same number of rays.

$$d\Omega = \sin\Phi d\varphi_1 d\Phi \ . \tag{3.37}$$

Thus, the volume element in orientation space can be expressed as

$$d\boldsymbol{g} = \frac{1}{8\pi^2}\sin\Phi d\varphi_1 d\Phi d\varphi_2 \ . \tag{3.38}$$

where $1/8\pi^2$ is the normalization factor.

By substituting $\varsigma = \cos\Phi$, the infinitesimal increment of the new parameter ς can be expressed as

$$d\varsigma = \sin\Phi d\Phi \ . \tag{3.39}$$

Hence, the orientation increment element in orientation space $\{\varphi_1, \varsigma, \varphi_2\}$ can be rewritten by

$$d\boldsymbol{g} = \frac{1}{8\pi^2} d\varsigma d\varphi_1 d\varphi_2 \ . \tag{3.40}$$

Apparently, this orientation space has homogeneous density, which can be seen in Fig. 3.15 (b).

3.3.2 Representation of textures

In Section 3.3.1, the definition of orientation and orientation space are explained in detail. They are applicable for the question of orientation between the CC of a single crystal or one specific grain and SC. However, in terms of the orientations of a large number of grains, *i.e.*, *texture*, the question remains how to represent orientation and orientation space properly? Consider one specific crystal direction of all grains (*e.g.* the c axis of all grains in polycrystalline Mg) in relation to the SC. Then, we can plot all the c poles as points on the *pole figure*.

Fig. 3.16 shows the pole figure of rolled AZ31B Mg alloy [54], which exhibits a typical basal texture of moderate strength and uniform distribution of prismatic poles. This is the smoothed recalculated pole figure.

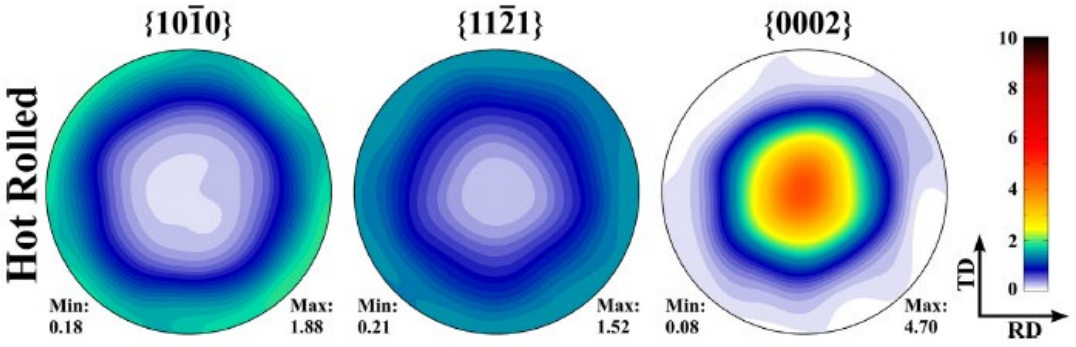

Fig. 3.16 Recalculated pole figures for a hot-rolled thick AZ31B Mg plate measured by neutron diffraction [54].

In the original pole figure, texture is represented by a large amount of discrete points, which may overlap and lead to an underestimation of distinct points and misinterpretation of texture. Therefore, it is beneficial to assign intrinsic weights / densities to discrete points to plot a contour pole figure. By plotting one specific axis of SC in CC of each grain, the *inverse pole figure* is obtained. This is especially useful when we consider the tensile axis of sample relative to the CC of one grain, where we can easily get the Schmid factor of one particular slip system. Fig. 3.17 illustrates the inverse pole figure of Mg-0.23 wt% Ce alloy (1:6 extrusion ratio) extruded at 450 °C [55].

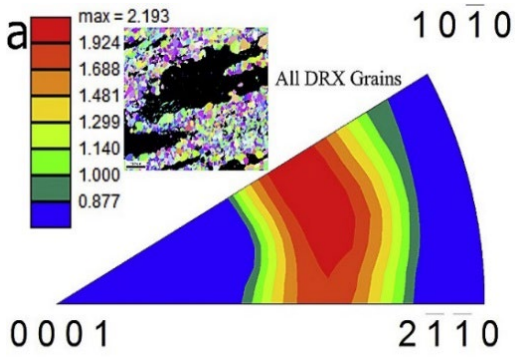

Fig. 3.17 Inverse pole figures (IPF) of Mg-0.23 wt % Ce alloy extruded at 450 ℃ [55].

In three dimensional orientation space, the texture of polycrystalline aggregates corresponds to a distribution of points. Conventionally, this distribution of orientation points is assumed to be continuous. This continuous orientation distribution can then be expressed as an expansion of series, which is the most frequently applied scheme in texture analysis.

As shown in Fig. 3.16, the texture reflects the crystal symmetry. Therefore, only one part of the pole figure is sufficient to express the whole information of texture. We can rotate the fixed SC to the fixed CC by the rotation matrix $\boldsymbol{g}$, where $\boldsymbol{g}$ corresponds to a set of Euler angles. Since there is also a series of rotations $\boldsymbol{g_A}$ by which the crystal can be transformed to its symmetrically equivalent orientation, the crystal cannot be distinguished from its pre-rotation state after subjected to rotation $\boldsymbol{g_A}$. Therefore, the orientation represented by $\boldsymbol{g}$ is equivalent to the orientation represented by $\boldsymbol{g_A \cdot g}$. This is the crystal symmetry. For the highest crystal symmetry of face-centered cubic metals, the texture is most frequently described by {111} pole figure. Since the {111} pole figure has four {111} poles, a quarter of the whole pole figure is then enough to represent the texture. Besides the crystal symmetry, the texture also reflects the sample symmetry. For instance, the axis symmetry of an as-extruded Mg alloy is related to the extrusion axis.

3.3.3 Orientation distribution functions

The texture of a polycrystalline aggregate can be described by an assembly of "discrete orientations," or by a "continuous pole figure" with intensity assigned to each orientation. Generally, the texture can also be represented by a continuous function, assuming that the orientations in orientation space are continuously distributed. If the totality of all volume elements of the sample, whose orientations fall within the infinitesimal interval $\boldsymbol{g}$~$\boldsymbol{g}$+$d\boldsymbol{g}$, is denoted by dV, and V is the total sample volume, we can then define an orientation distribution function $f(\boldsymbol{g})$, which follows:

$$\frac{dV}{V} = f\left(\boldsymbol{g}\right) d\boldsymbol{g} \ . \tag{3.41}$$

Obviously, if we set the orientation distribution function $f(\boldsymbol{g})$ to 1, then we get a random orientation distribution without preferred orientations. When the orientation $\boldsymbol{g}$ is expressed by Euler angles (φ_1, Φ, φ_2), the infinitesimal increment of orientation dg can then be represented by $d\boldsymbol{g} = \left(1/8\pi^2\right)\sin\Phi d\varphi_1 d\Phi d\varphi_2$ and

$$\frac{dV}{V} = \frac{1}{8\pi^2} f\left(\varphi_1, \Phi, \varphi_2\right)\sin\Phi d\varphi_1 d\Phi d\varphi_2 \ . \tag{3.42}$$

As introduced in Section 3.3.2, the orientation distribution essentially can be characterized by the "ray vector density" on the surface of a sphere. Hence, from an intuitive view, the orientation distribution function may be expressed by *"generalized spherical harmonics"*. Bunge [56] has done pioneering work in expanding the orientation distribution function $f(\boldsymbol{g})$ to series and develop this harmonic method to a general method for quantitative texture analysis. The term of orientation distribution function sometimes has indeed been the synonym of the harmonic decomposition. The harmonic decomposition is very suitable for describing the gradual variation near a random orientation distribution. If only few terms of the harmonics are required to represent the orientation distribution function, the harmonic decomposition can prove its greatest usefulness.

The generalized spherical harmonics can be expressed as [56, 57]

$$f\left(\boldsymbol{g}\right) = \sum_{l=0}^{\infty}\sum_{m=-l}^{+l}\sum_{n=-l}^{+l} C_l^{m,n} T_l^{m,n}\left(\boldsymbol{g}\right) \ . \tag{3.43}$$

The orientation distribution function can also be expressed by Euler angles

$$f\left(\varphi_1, \Phi, \varphi_2\right) = \sum_{l=0}^{\infty}\sum_{m=-l}^{+l}\sum_{n=-l}^{+l} C_l^{m,n} e^{im\varphi_2} P_l^{m,n}\left(\Phi\right) e^{im\varphi_1} \ . \tag{3.44}$$

$P_l^{m,n}(\Phi)$ are the associated Legendre functions. There exist some relations between the coefficients of $f(\varphi_1,\Phi,\varphi_2)$ and $T_l^{m,n}(\boldsymbol{g})$ can be expressed as

$$T_l^{m,n}(\boldsymbol{g}) = T_l^{m,n}(\varphi_1,\Phi,\varphi_2) = e^{im\varphi_2} P_l^{m,n}(\cos\Phi) e^{im\varphi_1} \quad . \tag{3.45a}$$

Where

$$P_l^{m,n}(\cos\Phi) = P_l^{m,n}(x)$$
$$= \frac{(-1)^{l-m} i^{n-m}}{2^l (l-m)!} \left[\frac{(l-m)!(l+n)!}{(l+m)!(l-n)!}\right]^{1/2} \cdot (1-x)^{-\frac{n-m}{2}} \cdot (1+x)^{-\frac{n+m}{2}} \cdot \frac{d^{l-n}}{dx^{l-n}} \left[(1-x)^{l-m}(1+x)^{l+m}\right] \quad . \tag{3.45b}$$

$T_l^{m,n}(\boldsymbol{g})$ has an advantageous property, *i.e.*, the orthonormality, which can be expressed as

$$\int T_l^{m,n}(\boldsymbol{g}) T^{*m',n'}_{l'}(\boldsymbol{g}) d\boldsymbol{g} = \frac{1}{2l+1} \delta_{ll'} \delta_{mm'} \delta_{nn'} \quad , \tag{3.46}$$

where $\delta_{ll'}\delta_{mm'}\delta_{nn'}$ is the three-dimensional δ function.

The essence of texture analysis is to derive the ODF from the PDF (pole density function) by using the harmonic spherical function series method. Eqs. (3.43) to (3.46) are especially useful in calculating the ODF. The software MTEX is based on this method and is extensively used in post processing of pole figures in texture modeling and simulation [58].

3.4 Deformation modes in Magnesium

3.4.1 Overview of deformation modes in Magnesium

Mg possesses hexagonal-close-packed (hcp) lattice structure, with the ratio of its *c* axis to *a* axis equal to 1.6242. The lattice parameter of Mg is *a*=320.94 pm and *c*=521.08 pm [59]. In the lattices of hcp materials, the densest-packed lattice plane and lattice directions are {0001} and ⟨**a**⟩=⟨$2\bar{1}\bar{1}0$⟩/3, respectively. The easiest slipping of dislocations prolongs via these lattice planes and directions. In Mg, these are, more precise, {0001}⟨$2\bar{1}\bar{1}0$⟩ with Burgers vector of ⟨**a**⟩, which consists of three different variants, (0001)[$2\bar{1}\bar{1}0$], (0001)[$\bar{1}2\bar{1}0$] and (0001)[$\bar{1}\bar{1}20$]. These systems compose the basal slip systems ([$2\bar{1}\bar{1}0$] also denotes the inverse slipping direction to ⟨$2\bar{1}\bar{1}0$⟩). The basal slip systems can only accommodate plane strain in the basal plane. When the strain contains components along the *c* axis, the activation of other deformation modes are required for slip. These deformation modes include non-basal slip systems such as prismatic slip {$10\bar{1}0$}⟨$2\bar{1}\bar{1}0$⟩, {$10\bar{1}0$}⟨0001⟩, first-order pyramidal slip{$10\bar{1}1$}⟨$\bar{1}\bar{1}20$⟩, {$10\bar{1}1$}⟨$\bar{2}113$⟩, second-order pyramidal slip {$2\bar{1}\bar{1}2$}⟨$\bar{2}113$⟩, tensile twinning {$10\bar{1}2$}⟨$\bar{1}011$⟩, {$2\bar{1}\bar{1}1$}⟨$\bar{2}116$⟩ and compression twinning {$10\bar{1}1$}⟨$\bar{1}012$⟩, {$2\bar{1}\bar{1}2$}⟨$\bar{2}113$⟩. These deformation modes are listed in Table 3.1

Table 3.1 The independent deformation modes of Mg.

Modes	Plane	direction (Burgers vector)	Crystallographic elements	Variants number
Basal sip	basal {0001}	**a**=⟨2$\bar{1}\bar{1}$0⟩/3	{0001} ⟨2$\bar{1}\bar{1}$0⟩	3
prismatic slip	prismatic {10$\bar{1}$0}	**a**=⟨2$\bar{1}\bar{1}$0⟩/3	{10$\bar{1}$0} ⟨2$\bar{1}\bar{1}$0⟩	3
		c=⟨0001⟩	{10$\bar{1}$0} ⟨0001⟩	3
1st order pyramidal slip	1st order pyramidal {10$\bar{1}$1}	**a**=⟨$\bar{1}\bar{1}$20⟩/3	{10$\bar{1}$1} ⟨$\bar{1}\bar{1}$20⟩	6
		c+a =⟨$\bar{2}$113⟩/3	{10$\bar{1}$1}⟨$\bar{2}$113⟩	12
2nd order pyramidal slip	2nd order pyramidal{2$\bar{1}\bar{1}$2}	**c+a** =⟨$\bar{2}$113⟩/3	{2$\bar{1}\bar{1}$2}⟨$\bar{2}$113⟩	6
tensile twinning	TT1: {10$\bar{1}$2}	⟨$\bar{1}$011⟩	{10$\bar{1}$2}⟨$\bar{1}$011⟩	6
	TT2: {2$\bar{1}\bar{1}$1}	⟨$\bar{2}$116⟩/6	{2$\bar{1}\bar{1}$1} ⟨$\bar{2}$116⟩	6
compression twinning	CT1: {10$\bar{1}$1}	⟨$\bar{1}$012⟩/2	{10$\bar{1}$1}⟨$\bar{1}$012⟩	6
	CT2: {2$\bar{1}\bar{1}$2}	⟨$\bar{2}$113⟩/3	{2$\bar{1}\bar{1}$2} ⟨$\bar{2}$113⟩	6

The fact that hexagonal metals are crystallographically double-lattice structures implies that dislocation glide via non-basal slip modes goes along with a large Burgers vector, leaving high-energy stacking faults behind [43]. In principle, the non-basal slip systems are far more difficult to be activated compared with the basal slip systems. For example, 12 atomic bonds need to be broken to allow for pyramidal dislocation slip, while only 5 atomic bonds are required in the case of basal dislocation slip occurring on the close-packed plane [43]. Nevertheless, some experimental researches gave the evidence of the occurrence of non-basal slip such as pyramidal slip $\{2\bar{1}\bar{1}2\}\langle\bar{2}113\rangle$ at room temperature [4, 23, 24, 60]. However, the activity of non-basal slip at room temperature is generally very low due to the very high work hardening rate of this slip system below temperatures of 200 °C.

Twinning accommodates c-axis deformation by homogenous simple shear. The twins can easily nucleate and grow through the glide activities of free twin partial dislocations that spread a stable twin fault (see Section 3.4.2.2). Reported CRSS values for pure Mg, as listed in Table 3.2, directly reveal the relative relevance of different deformation modes at room temperature: Basal slip has the lowest value, spanning from 0.45 to 0.81 MPa, followed by tensile twinning $\{10\bar{1}2\}\langle\bar{1}011\rangle$ with approximately 2 MPa. In contrast, prismatic slip has a considerably higher CRSS of 41 MPa, and compression twinning has the highest value of 80-100 MPa. This indicates, confirming the experimental observation, that at room temperature deformation twinning is by far the most efficient, almost exclusively active deformation mode for the accommodation of strain components along the *c* axis. It should be noted that the

situation changes towards elevated temperature above 180 °C, where pyramidal slip can be easily activated, significantly improving the deformability of Mg [61].

Table 3.2 The CRSS (Critical Resolved Shear Stress) values for pure Mg and AZ31B [31, 62-64].

Samples	CRSS(MPa)				
	Basal	Prismatic	2nd Pyramidal	Tensile twinning	Compression twinning
Mg SC	0.45-0.81	39	44	2	30-100
AZ31B PC	10-45	55-100	100-180	10-30	-

3.4.2 Deformation twinning in Mg

3.4.2.1 Deformation twinning and microstructure

The main contrasting features of deformation twinning relative to slip are (1) polarity due to directionality of twin shear and (2) the abrupt or discontinuous reorientation of a part of the parent grain (see Fig. 3.18). The magnitude of volume depends on the characteristic twin shear and macro strain. Polarity makes at least two frequent modes necessary for the accommodation of both tensile and compressive deformation. In those materials with particularly distinct texture, such as extruded Mg bar, twinning is very favorable [12]. Due to reorientation by tensile twinning (see Fig. 3.18), the type and activity of operative deformation modes changes dramatically. As a consequence, significant twin hardening caused by abundant twin-twin interactions (see Fig. 3.19 (a)-(c)) together with strong mechanical anisotropy can initiate crack formation (see Fig. 3.19 (d)-(f)).

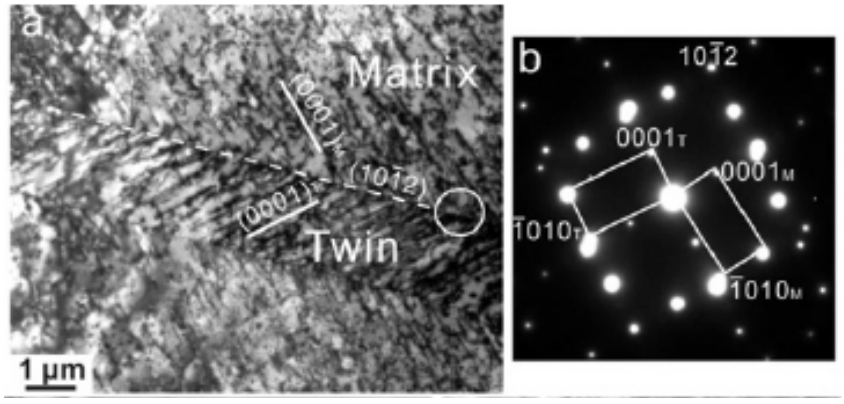

Fig. 3.18. TEM images of the tensile twins formed in Mg single crystals after compression along [0001], adopted from [65].

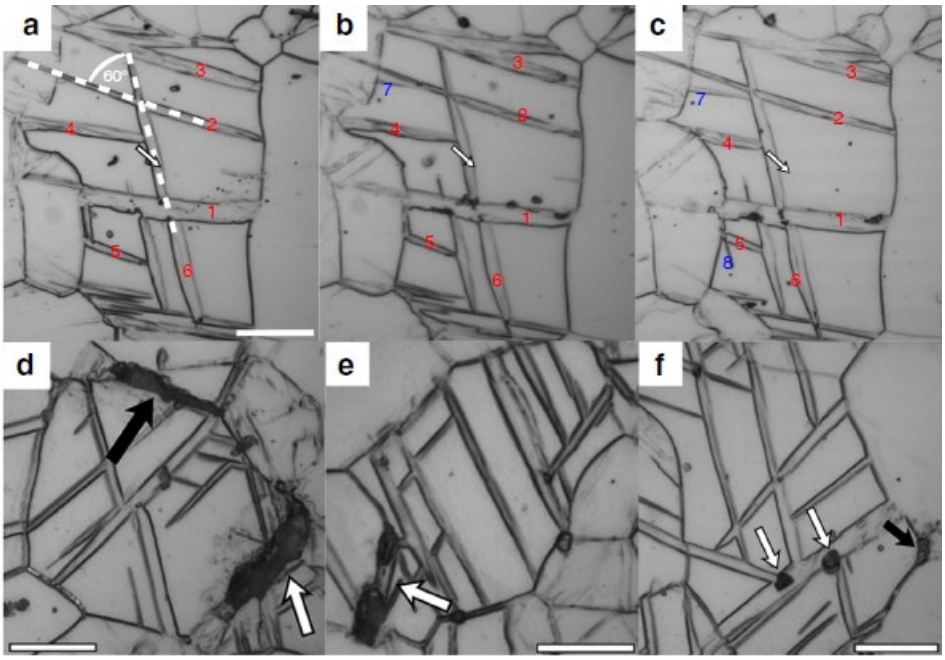

Fig. 3.19. 3D structure of contraction twin networks: the contraction twin network (a–c) and sites of crack and void formation (d-f) [66].

Detwinning, which denotes the disappearance of twins by thinning, has been occasionally observed in Mg [48, 67-68]. Existing, limited literature on detwinning mechanism treats exclusively face-centered cubic metals [69-70]. The mechanism of detwinning and the parameters, which govern its occurrence in Mg, are still unclear.

3.4.2.2 Geometric and crystallographic descriptions of deformation twins

Generally, the deformation twinning can be considered equivalent to a simple shear, which re-orients the original (parent) lattice, resulting in the re-oriented lattice (twinned part) to be the mirror image of the parent lattice (untwined part) in relation to a specific lattice plane. This simple shear of the lattice points is achieved by atom displacements on the specific plane (invariant plane). As shown in Fig. 3.20, the invariant plane of this shear is called $\boldsymbol{K_1}$ and the shear direction is $\boldsymbol{\eta_1}$; the second undistorted plane $\boldsymbol{K_2}$ is conjugated with the $\boldsymbol{K_1}$ plane. The plane containing $\boldsymbol{\eta_1}$ and normal to $\boldsymbol{K_1}$ and $\boldsymbol{K_2}$ is the plane of shear, here denoted by $\boldsymbol{P}$, and the intersection of $\boldsymbol{K_2}$ and $\boldsymbol{P}$ is the conjugate shear direction $\boldsymbol{\eta_2}$. Unlike slipping shear, the twinning shear has directionality, *i.e.*, twinning shear can only occur in one direction and cannot be inverted.

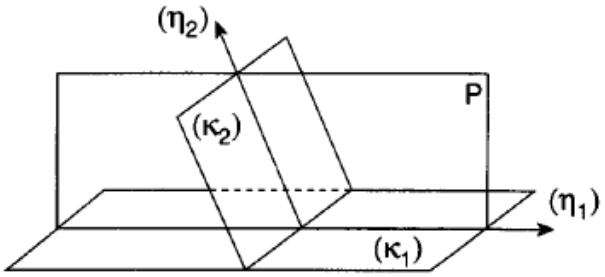

Fig. 3.20. The four twinning elements [71].

The specific shear of twin, $s_{0,}$, can be defined as s_0=s/d, where d is the distance between two adjacent twin planes $\boldsymbol{K_1}$ and s is the displacement of an atom moving form parent lattice position to its corresponding position in the twin lattice(see Fig. 3.21).

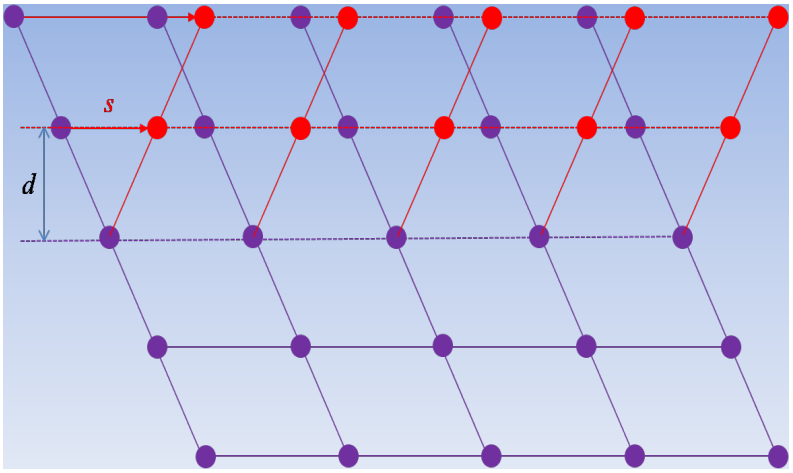

Fig. 3.21. The schematic figure of twin shear.

The affine deformation can be used to represent a homogeneous simple shear, which transforms a parent lattice vector $\boldsymbol{u}$ to a twin lattice vector $\boldsymbol{v}$ through a second rank transformation tensor $\boldsymbol{S}$ [71]:

$$\boldsymbol{v} = \boldsymbol{S}\boldsymbol{u} \ . \tag{3.47a}$$

In order to be applied in computer calculation, the component form of Eq. (3.47a) is favored. In one specific coordinate system A, its component form can be expressed as

$$^{A}v^{i} = {}^{A}S^{i}_{j} \cdot {}^{A}u^{j} \ . \tag{3.47b}$$

$^{A}v^{i}$ and $^{A}u^{j}$ are the contravariant (real space) components of the vectors $\boldsymbol{u}$ and $\boldsymbol{v}$ in coordinate system A (here Einstein summation convention is applied). The transformation tensor $\boldsymbol{S}$ can be further expressed as

$$\boldsymbol{S} = \boldsymbol{I} + s_0 \boldsymbol{lm} \ , \tag{3.48a}$$

where $\boldsymbol{lm}$ is the dyadic product of vector $\boldsymbol{l}$ and $\boldsymbol{m}$, which is the unit vector along the shear direction $\boldsymbol{\eta_1}$ and the unit normal vector to twinning plane $\boldsymbol{K_1}$, and $\boldsymbol{I}$ is the unit tensor. The component form of transformation tensor $\boldsymbol{S}$ in coordinate system A is

$$^{A}S^{i}_{j} = \delta^{i}_{j} + s_0 \cdot {}^{A}l^{i} \cdot {}^{A}m_{j} \ , \tag{3.48b}$$

where δ^{i}_{j} is the Kronecker delta, and $^{A}l^{i}$ are the contravariant components of a unit vector $\boldsymbol{l}$ and covariant components of a unit vector $\boldsymbol{m}$. Particularly, if we choose a special orthonormal coordinate system with the 1st and 2nd coordinate axis defined as $\boldsymbol{l}$ and $\boldsymbol{m}$, respectively, and the 3rd axis obtained by right hand rule, then the transformation tensor $\boldsymbol{S}$ will possess a very simple representation.

$$\boldsymbol{S} = \begin{bmatrix} 1 & s_0 & 0 \\ 0 & 1 & 0 \\ 0 & 0 & 1 \end{bmatrix} . \tag{3.48c}$$

It should be noted that the twin lattice vector $\boldsymbol{v}$ is expressed in coordinate system A, *e.g.* the parent crystal coordinate system, and normally has irrational components. However, $\boldsymbol{v}$ must have rational components when it is decomposed into the twin crystal coordinate system B. There are some rotation or reflection tensors, $\boldsymbol{L}$, which link the parent crystal coordinate system A and the twin crystal coordinate system B,

$$^{B}v^{i} = L^{i}_{j} \, {}^{A}v^{j} = L^{i}_{j} \, {}^{A}S^{j}_{k} \, {}^{A}u^{k} = C^{i}_{k} \, {}^{A}u^{k} \ , \tag{3.49}$$

where $^{B}v^{i}$ and $^{A}v^{j}$ are the contravariant components of the same vector $\boldsymbol{v}$ in different coordinate systems A and B. It should be noted that $^{B}\boldsymbol{v} = {}^{A}\boldsymbol{v}$, if vector $\boldsymbol{v}$ is expressed in entity form. Eq. (3.47) to Eq. (3.49) are very important for coordinate transformation in crystal plasticity studies. However, a more explicit formula, *i.e.*, a transformation/rotation matrix $\boldsymbol{Q}$ should be exploited when describing a vector in parent crystal lattice moved into its new position in the twin.

$$\boldsymbol{Q} = 2\boldsymbol{mm} - \boldsymbol{I} \ , \tag{3.50}$$

where $\boldsymbol{mm}$ is the dyadic product of unit normal $\boldsymbol{m}$ to the twin $\boldsymbol{K_1}$, and $\boldsymbol{I}$ is a unit two-rank tensor, whose component is Kronecker δ. The physical meaning of Eq. (3.50) is equivalent to the manipulation of rotating the upper half of the crystal by an angle π around the twin normal $\boldsymbol{m}$, as shown in Fig. 3.22.

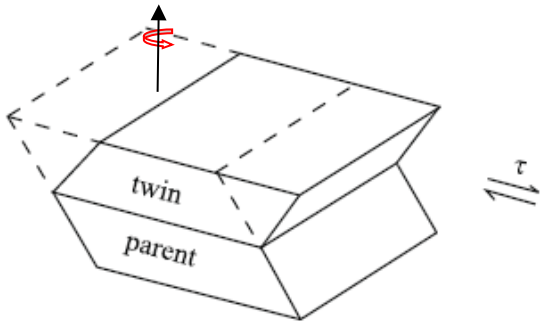

Fig. 3.22. Under the applied shear stress, one-half of the initial volume (dashed lines) shears to form a twin (solid lines).

For Mg comprising a double-lattice structure, twin formation requires atomic shuffles in addition to twin shear [4, 71]. Although atomic shuffles do not induce deformation, they cost energy. The most frequently observed twins in Mg and other hcp metals, such as Ti, Zr and Be, can be ascribed to the relatively low specific shear and simple atomic shuffle mechanisms of these twin modes. Table 3.3 lists twinning modes and the associated essential parameters in Mg. These parameters are widely used in polycrystal plasticity simulations and serve for twin identification in electron backscattered diffraction (EBSD) experimental results. Importantly, the tensile twin can significantly reorient the c axis of the crystal, which has profound effects on the texture evolution of Mg during deformation.

Table 3.3 Twinning modes and associated parameters in Mg [71].

Twinning mode	K_1	η_1	zone axis	Angle	Shear
Tensile twin	$\{10\bar{1}2\}$	$\langle\bar{1}011\rangle$	$\langle\bar{1}2\bar{1}0\rangle$	86.32	0.129
Compression twin	$\{10\bar{1}1\}$	$\langle\bar{1}012\rangle$	$\langle\bar{1}2\bar{1}0\rangle$	56.46	0.139

3.4.2.3 Nucleation and growth of deformation twins

It is known that nucleation of deformation twins requires the dissociation of a dislocation configuration into single- or multi-layered stacking faults, which serve as twin nuclei. These fault configurations are bounded by partial dislocations of the parent crystal, which can also be considered as twinning dislocations [71]. Therefore, the nucleation of deformation twins is closely related to the stacking fault energy (SFE) of metals and the stress state in the grain interior. The cooperative motion of a large number of these partial dislocations is required for

the successive growth of a deformation twin [72]. Two principle categories of twinning mechanisms have been distinguished: 1) The pole mechanism was first proposed by Cottrell and Bilby [73], in order to explain deformation twinning in bcc metals. The pole mechanism describes the strict dissociation of a perfect dislocation into two twinning partials. One twinning partial is lying in the twin plane, whose Burgers vector is precisely the same as the specific shear of the involved twin system. The second partial is lying outside of the twin plane (pole dislocation), whose Burgers vector is normal to the interface equal to the inter-plane spacing of the twin planes. 2) The double-cross-slip mechanism was proposed by Pirouz (1987) [74]. This mechanism assumes the dissociation of a perfect screw dislocation segment into a leading partial, which lies in the twinning plane and can easily move under an applied stress, and an almost "stationary" trailing partial, which also lies in the twinning plane. When the applied stress on the leading partial allows it to overcome the critical radius, the leading partial will leave a partial dislocation loop, which is similar to a Frank-Read source. The loop extends, forming one layer of twin. Simultaneously, the leading partial proceeds, regenerating the original perfect screw segment with the trailing partial. Because the perfect dislocation segment is screw, it may double cross-slip to the adjacent twin plane and repeat the process above.

Double-cross-slipping seems to represent the more likely twinning mechanism in Mg alloys. First, in low symmetry structures with several active twinning modes, suitable pole dislocations are difficult to find and even do not exist. Second, the calculated twinning stress according to pole mechanism, which is needed to overcome the attractive forces between the partials involved in the dissociation reaction, is much larger than the experimentally determined twinning stresses. Even though there is still no direct proof for the precise nucleation and growth mechanism of deformation twins in Mg, there is general agreement that nucleation and growth of deformation twins is related to the SFE and the stress state in the grain interior [71, 75].

Statistical EBSD analyses of deformation twinning in magnesium suggests that the grain boundary misorientation angle strongly influences twin nucleation and growth [76]. Khosravani [77] studied nucleation and propagation of tensile twins in magnesium alloy AZ31 by high-resolution electron backscatter diffraction (HREBSD) and found the following relations of twin types to misorientation angle distribution: (1) Slip-assisted twins that apparently nucleated without influence from nearby twins are frequently observed at high-angle boundaries. (2) Twin-assisted twin formation spread from twins propagating across a grain boundary usually took place at low-angle boundaries.

The weak relationship between crystal orientation and twin variant selection and the strong correlation between grain size and the number of twins formed per grain are frequently observed

in Mg and other hcp metals. Proper modeling of the nucleation of deformation twins contains the consideration that twins originate from a statistical distribution of defects on the grain boundaries and are activated by local stresses at the grain boundaries. This further suggests the significance of stress fluctuations generated at grain boundaries for experimentally observed dispersion in the twin variant selection [78].

Twin-twin interaction has been frequently observed in EBSD images. Studying twin-twin interactions, including their influence on hardening and detwinning, by materials modeling tools at meso- and micro-scales, particularly by crystal plasticity models, complement feasible microstructural and mechanical modeling packages of Mg alloys. Yu et al. [48] revealed the features of the twin-twin boundary and distinguished three kinds of twin-twin structures in single crystal Mg (see Fig. 3.23), which was subjected to a cyclical loading in [0001] and directions. (1) Quilted-looking twin structure consisting of twins arrested at other twin boundaries; (2) An "apparent crossing" twin structure, which links twins impinging independently on each side of twin lamella and (3) a double twin structure that results from secondary twins being nucleated at twin-twin interfaces.

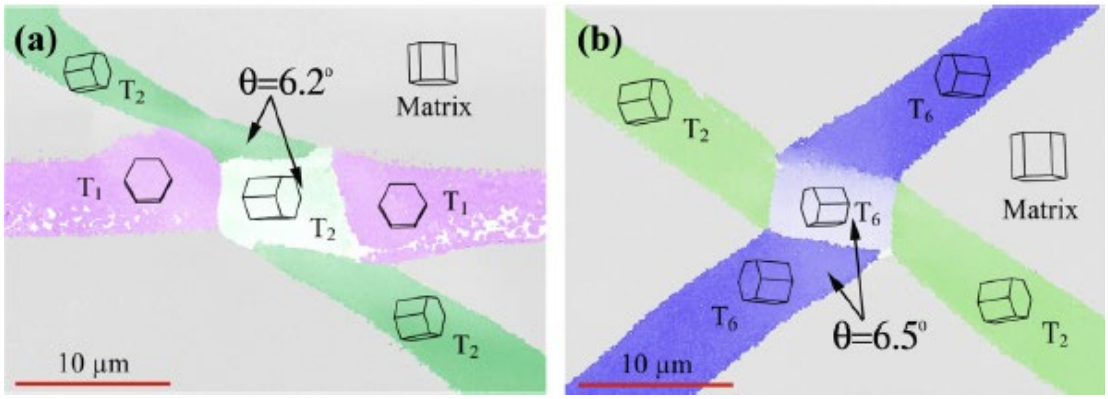

Fig. 3.23. "Cross structures" of different tensile twin variants in Mg: (a) two T1 twins and one T2 twin and (b) two T2 twins and one T6 twin [48].

3.5 Basics of crystal plasticity

3.5.1 Kinematics of crystal plasticity

In this chapter, some basic concepts in continuum mechanics, which are essential for crystal plasticity, are introduced, such as, deformation gradient, displacement gradient and velocity gradient. These concepts comprise important prerequisite for understanding different crystal plasticity models, such as, Taylor-type models, self-consistent models and crystal plasticity finite element methods.

3.5.1.1 Material points and spatial points

In continuum mechanics, the basic property of a body is that it may occupy regions of Euclidean point space E. The body and the spatial region ***B*** it occupies at a specific moment are called a reference configuration. For specificity, ***B*** is referred to as the *reference body* and a point ***X*** in ***B*** is referred to as a *material point* or *particle*. Via a smooth function χ, a point is assigned to each material point X at time t

$$\mathbf{x} = \boldsymbol{\chi}(\mathbf{X},\ \mathrm{t})\ . \tag{3.51}$$

x is referred to as the *spatial point* occupied by **X** at time t. χ(**X**, t) is a function of **X** and describes the deformation configuration at time t. A basic hypothesis of continuum mechanics is that χ (**X**) is one-to-one in X, so that no two material points may occupy the same spatial point at a given time, or, more descriptively, so that the body cannot penetrate itself. The region of space occupied by the body at time t, $\boldsymbol{B}_t = \chi_t(\mathbf{B})$ is referred to as the deformed body at time *t*, as shown in Fig. 3.24.

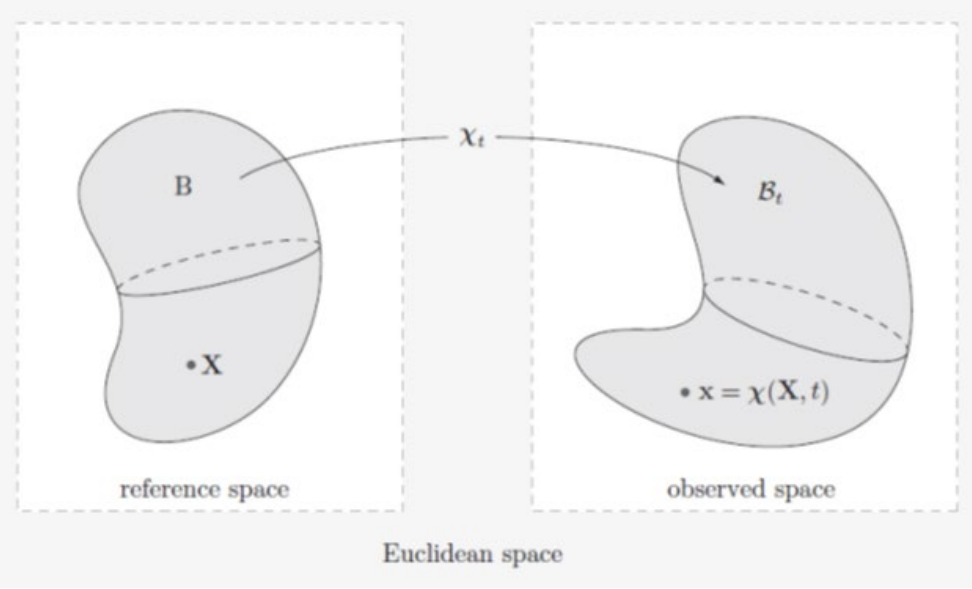

Fig. 3.24. The reference body *B* and the deformed body B_t [79].

In all kinds of continuum field modeling of the crystal plasticity, a material point refers to a representative volume element (RVE). Only over the volume of the material point, the micro-stress field and the micro-strain field can be considered as homogeneous. In other words, because plastic deformation is locally discrete and inhomogeneous, the applicability of continuum field is only limited to volume elements not smaller than the RVE [80].

3.5.1.2 Deformation gradient

The deformation gradient tensor field is defined as

$$\mathbf{F} = \nabla \boldsymbol{\chi} \ , \tag{3.52}$$

$$d\mathbf{x} = \mathbf{F} \cdot d\mathbf{X} = d\mathbf{X} \cdot \mathbf{F}^{\mathrm{T}} \ . \tag{3.53}$$

Keep in mind that the deformation gradient **F** is defined relative to the reference configuration ***B***, which provides the relationship between a material line d**X** before deformation and the line *d***x**, which consists of the same material as *d***X** after deformation**.**

R_0 and R denote regions within the body in the reference (undeformed) configuration and current (deformed) configuration, respectively. Further, let **N** be a unit vector embedded within the body in the reference configuration. The deformation transforms **N** to **n** in the deformed state. The square of the stretch of N, λ(N), can be calculated as

$$\lambda^2(\mathbf{N}) = (\mathbf{F}\cdot\mathbf{N})\cdot(\mathbf{F}\cdot\mathbf{N}) = \mathbf{N}\cdot\mathbf{F}^{\mathbf{T}}\cdot\mathbf{F}\cdot\mathbf{N} \ . \tag{3.54}$$

Define $\mathbf{C} \equiv \mathbf{F}^{\mathbf{T}} \cdot \mathbf{F}$ as the right Cauchy-Green deformation tensor

$$\mathbf{E} = \frac{1}{2}(\mathbf{C} - \mathbf{I}) \ . \tag{3.55}$$

which is known as the Lagrangian strain tensor

3.5.1.3 Velocity gradient

The spatial tensor field

$$\mathbf{L} = \nabla \mathbf{v} \ , \tag{3.56}$$

is called the velocity gradient, where ***v*** is the velocity. It should be noted that the gradient operation is considered relative to the current configuration. The velocity gradient can be also expressed as

$$\mathbf{L} = \dot{\mathbf{F}} \cdot \mathbf{F}^{-1} \ . \tag{3.57}$$

If we decompose **L** into its symmetric and antisymmetric parts as

$$\mathbf{L} = \frac{1}{2}\left(\mathbf{L} + \mathbf{L}^T\right) - \frac{1}{2}\left(\mathbf{L} - \mathbf{L}^T\right) \ , \tag{3.58}$$

the symmetric tensor **D** is called the rate of deformation or simply the deformation rate

$$\mathbf{D} = \frac{1}{2}\left(\mathbf{L} + \mathbf{L}^T\right) \ . \tag{3.59}$$

$$\mathbf{W} = \frac{1}{2}\left(\mathbf{L} - \mathbf{L}^T\right) \ . \tag{3.60}$$

If the current state is taken as the reference state, we refer to the tensor fields **W** and **D**, respectively, as the spin and the stretching tensors. The spin tensor is responsible for the texture evolution, and will be used in Chapter 6. In most cases, only the lattice rotation caused by plastic strain rate components is considered, while the lattice rotation caused by elastic strain component is ignored, which is the so-called rigid plastic idealization.

3.5.2 Kinetics of crystal plasticity

As mentioned in Section 3.1.1, only if the driving force on the dislocation lines attain a critical value, the shear of the crystal can be activated. In the extreme case, where a nearly perfect crystal is subjected to increasing levels of shear stress at 0K, the shear strain rate will experience an abrupt rise, which is schematically shown in Fig. 3.27. When the shear stress σ is less than a definite value $\hat{\tau}(0)$, no shear strain rate $\dot{\gamma}$ can be detected. $\hat{\tau}(0)$ is the *mechanical threshold* for initiating deformation by a specific mechanism at T = 0K [81].

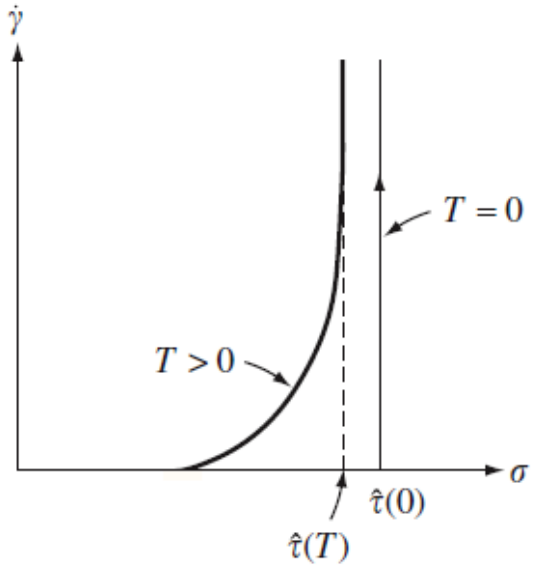

Fig. 3.25. The strain rate $\dot{\gamma}$ blows up at mechanical threshold $\hat{\tau}(0)$ at 0K [81].

However, real materials with the usual internal variability of defect structure must have a smooth transition from no deformation to a high rate of deformation at *T*>0K. $\hat{\tau}(T)$ refers to the rate-independent (athermal) reference mechanical threshold at *T*. Namely, at non-zero temperature, the local energy barriers for the dislocation glide process can be overcome at lower resolved shear stresses with the help of thermal activation, the physics of which can be expressed by an Arrhenius law.

$$\dot{\gamma}_i^s = \dot{\gamma}_0 \exp\left(-\frac{\Delta G\left(\tau^s, \hat{\tau}\right)}{kT}\right), \tag{3.61}$$

where τ^s is the applied shear stress and $\Delta G\left(\tau^s, \hat{\tau}\right)$ is the required activation energy. The required activation energy decreases with increasing τ^s, resulting in a higher strain rate. Furthermore, only in the extreme case at 0K, the deformation process shows a strict "rate independence," because the strain rate is undetermined in this case, as shown in Fig. 3.25. In

most realistic cases, where thermal activation takes effect, the actual curve of $\dot{\gamma}-\hat{\tau}$ is even much steeper than that shown in Fig. 3.25, indicating that the yield of the crystal is rate insensitive albeit not rate independent [82]. The frequently used alternative choice is the power law

$$\dot{\gamma}_i^s = \dot{\gamma}_0 \left| \frac{\tau_i^s}{\tau_0^s} \right|^m \operatorname{sgn}\left(\boldsymbol{\sigma}:\mathbf{m}^s\right) = \dot{\gamma}_0 \left| \frac{\boldsymbol{\sigma}:\mathbf{m}^s}{\tau_0^s} \right|^m \operatorname{sgn}\left(\boldsymbol{\sigma}:\mathbf{m}^s\right) , \tag{3.62}$$

where τ_0^s is the shear stress at the reference shear strain rate $\dot{\gamma}_0$. It should be noted that the rate independency corresponds to *m* approaching ∞. Then in the individual grain of polycrystal aggregates, the kinetics can be described as

$$\mathbf{D}^c = \dot{\gamma}_0 \sum_s \left| \frac{\boldsymbol{\sigma}:\mathbf{m}^s}{\tau_0^s} \right|^m \mathbf{m}^s \operatorname{sgn}\left(\boldsymbol{\sigma}:\mathbf{m}^s\right) . \tag{3.63}$$

Eq. (3.63), extensively used in crystal plasticity, gives the relation between the strain tensor in the crystal scale $\mathbf{D}^c$ and the crystal-level stress.

3.6 Reviews on modeling method of crystal plasticity

3.6.1 Taylor type model

In 1938, Taylor proposed a model, which simply assumed that the deformation gradient in each grain in a polycrystal aggregate is the same, *i.e.*, the microscopic strain rate is the same as the macroscopic strain rate [27]. This model was initially proposed to describe deformation in Al and other fcc metals, which possess 12 independent slip systems. In the original version of the Taylor model (also called full constraints Taylor model, in short FC model), five independent slip systems must be simultaneously activated to accommodate any arbitrary strain, because there are 5 independent components in any strain tensor. The key of the Taylor model is to select a combination of slip systems, which not only satisfies the geometry condition but also, in coupling with strain tensor, an energetic condition. He showed that the active five slip systems have the minimum absolute sum of shear. The Taylor model has witnessed a conspicuous success in the prediction of the mechanical response and texture evolution of fcc metals during deformation processes in a wide range of applications.

In 1951, Bishop and Hill presented a theory of the plastic deformation of a polycrystalline material based on the maximum work principle [30]. In his theory, Bishop generalized Taylor´s energetic condition of minimum absolute sum of shear in his minimum work conclusion

$$\sum_s \tau_s \left| d\gamma_s \right| \le \sum_s \tau_s \left| d\gamma_s^* \right| , \tag{3.64}$$

where $d\gamma_s$ is the shear of a set of active slip systems, and $d\gamma_s^*$ represents any set of shears, which are geometrically equivalent to the prescribed strain. Particularly, when the critical shear stress in every slip system is the same (equal hardening in all directions), Eq. (3.64) can be simplified to

$$\sum_s \left| d\gamma_s \right| \leq \sum_s \left| d\gamma_s^* \right| , \tag{3.65}$$

which is exactly the energy condition in Taylor's original paper. The Taylor model remains a suitable tool for first order approximations via fast calculation (at least 2 orders of magnitude faster than more recent VPSC and CPFEM developments, see following chapters). The Taylor model is expected to fail in those cases, where the plastic heterogeneity is too large [83]. For instance, during deep rolling, the shape of grains is severely distorted and becomes plate-like. As a consequence, the required relaxation of one direction in the FC model cannot be satisfied and the model cannot be applied. Advanced Taylor type model like ALAMEL model with relaxed constraint proposed can produce feasible results [29].

3.6.2 Self-consistent Method

As mentioned in Section 3.6.1, the Taylor model simply assumes that the strain in the individual grain (local strain) is the same as the overall strain in a polycrystalline metal, assuring the compatibility condition across the grain boundaries [84]. However, this implies that the equilibrium condition between grains cannot be satisfied. Not so in the case of a self-consistent model, which relates the local strain, local plastic strain and local stress (ε, ε^p, σ) in the individual grain to the overall strain, overall plastic strain and overall stress (ε^*, ε^{*p}, σ^*), as first proposed by Kröner in 1961 [85] and then by Budiansky and Wu in 1961 [86]. In their model, the interaction of an individual grain with its surrounding material consisting of a polycrystalline aggregate was simplified to the case of an elastically isotropic sphere embedded in a homogeneous matrix of the polycrystalline aggregate, as shown in the Fig. 3.26.

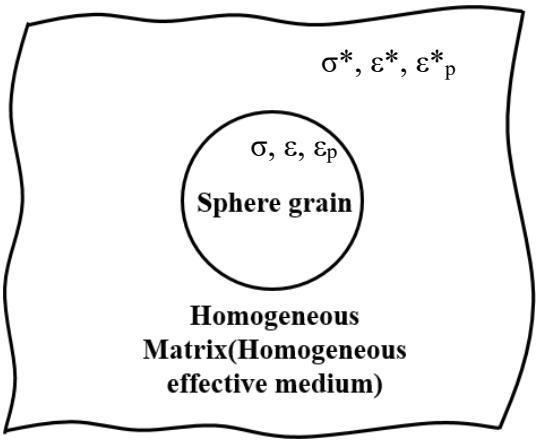

Fig. 3.26. Schematical representation of the Kröner, Budiansky and Wu's [86] model setting.

The following three conditions have to be met in Kröner, Budiansky and Wu's model: 1) The averages of local stress and local strain over the whole polycrystal must yield overall stress and overall strain. 2) Strain compatibility must prevail on the grain boundary. And 3) stress equilibrium on the grain boundary must hold[84]. The Eshelby's solution for inclusion problems [87, 88] was used in the self-consistent approach to determine the relation between local quantities (ε, ε_p, σ) and global quantities (ε^*, ε^*_p, σ^*). For Eshelby´s solution for the elastic inclusion problem, matrix and inclusion properties need to be known beforehand. In contrast, in the self-consistent approach, these properties are being obtained during numerical iteration by imposing the condition that the averages of local stress and local strain over the whole polycrystalline must yield overall stress and overall strain.

Other self-consistent methods have been proposed by Hill [89] and Lebensohn et al. [90]. Recently, self-consistent methods, and, hereby, especially the VPSC method, have been extensively used to predict the texture evolution and plastic response of hcp metals, including Mg, Zr and Ti [5, 93- 94]. Self-consistent methods are statistical, in which an inclusion with a particular orientation is the representative of all grains with the same orientation, and the homogeneous matrix represents the average surrounding of such set of grains [95]. This further means that self-consistent methods exhibit the feature of a mean field approach, and local stress and local strain inhomogeneities in the individual grain are not described. This shortcoming needs to be considered critically when it comes to large grain size. The assumption of a homogeneous effective medium might also become invalid when the discontinuity across the grain boundary is large [95], and of course in cases where local effects contribute considerably to the microstructural evolution. The latter situation is found in Mg alloys for twin-dislocations and twin-twin interactions.

3.6.3 Crystal Plasticity Finite Element Method

CPFEM is another method used in modeling and simulating of deformation processes and plasticity anisotropy. An increment of deformation in a crystalline solid can be imagined to happen in two steps. The first step is that a process of simple shears on slip systems occurs by starting from the reference state. The second step is that a process of lattice deformation occurs [96]. The basic kinematic scheme is shown in Fig. 3.27.

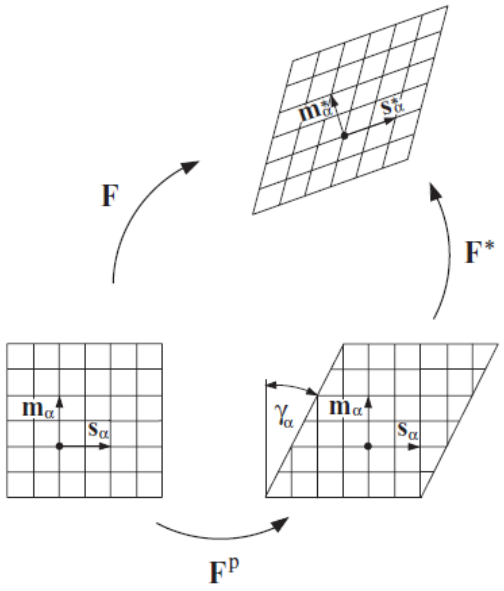

Fig. 3.27. Kinematic model of elastoplastic deformation of a single crystal [96].

Based on this scheme, the deformation gradient and velocity gradient can be decomposed into two parts, the plastic deformation gradient tensor and non-plastic deformation gradient tensor including rigid rotation and elastic distortion of the lattice. In CPFE, this understanding of crystal plasticity is embedded in the finite element method. The iterative calculation of node displacement yields the deformation gradient, and the mechanical response and the texture evolution is obtained by updating the slip plane's normal and slip direction in each simulation step. One can define the constitutive law and materials properties by himself, making this method versatile to a wide range of materials and compatible to diverse deformation mechanisms, such as, dislocation slip, martensite formation, twinning, grain boundary shear and deformation via shear banding [28].

Different to mean field methods, such as, Taylor type models and self-consistent models, CPFE, as a full field method, can tackle local effects and capture the physics of local twin-twin and twin-precipitate interaction mechanisms. On the other hand, CPFEM may meet limitations when it comes to predictions of flow curve and texture evolution of polycrystalline material due

to its high computational cost. This is the case when the required number of grains for prediction is large, *i.e.*, beyond 5000 grains. In turn, and in the spirit of multi-scale computational materials design, CPFE delivers valuable properties, such as, the local stress caused by twinning, which can serve as input parameter or calibration number for physical refinement of texture evolution models and flow curve simulations.

4 Experimental study and modeling on tensile twinning in AZ31 Mg alloy

Tensile twins, as the most frequently observed twin mode in Mg, play an important role in accommodating the strain components along the *c* axis of Mg. In this chapter, we focus on studying the tensile twinning by EBSD analysis and computational modeling. Section 4.1 summarizes the experimental observations on tensile twinning in as-extruded AZ31 Mg alloy by EBSD. The contribution of $\{10\bar{1}2\}\langle 10\bar{1}1\rangle$ tensile twinning to strain is studied in Section 4.1. The contribution of $\{10\bar{1}2\}\langle 10\bar{1}1\rangle$ tensile twinning to the strain can be divided into two parts: one is the contribution of twin nucleation and the other is the contribution of twin growth, which can be described by Eq. (4.5), later. Combining the experimental observations of tensile twinning in AZ31 alloy (Section 4.2) and the consideration on twin nucleation and growth (Section 4.3), Eq. (4.5) can be simplified. With this simplified equation and the experimental observation, the velocity of twin partial dislocations at the stages of twin nucleation and twin growth is estimated in Section 4.4. Based on the features of evolution of twin volume fraction and the saturation of twinning observed in Section 4.1, a semi-empirical law capturing twin growth is proposed in Section 4.5 and a brief summary on tensile twinning is given in Section 4.6.

4.1 Experimental observations of twinning in AZ31 alloy

As-extruded AZ31 Mg alloy bar samples with extrusion temperature of 350 °C are chosen for studying tensile twinning. Fig. 4.1 shows the initial texture of the as-extruded sample. In Fig. 4.1, the conventional "rolling direction" (RD) represents the direction of extruding, and the conventional "normal direction" (ND) represents an arbitrary direction, which is perpendicular to the RD direction in regard of the sample symmetry to the extruding axis.

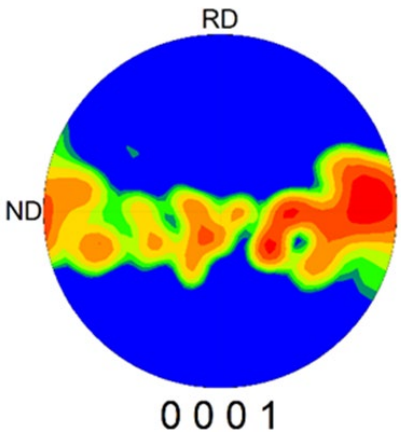

Fig. 4.1. The initial texture of as-extruded AZ31 alloy.

The pole figure reveals that the *c* axis of most grains is perpendicular to the extruding axis. This is consistent with typical extrusion textures of AZ31 reported in literature [2]. The as-extruded bar sample is subjected to a compression test. There, the compression axis is parallel to the direction of extruding, *i.e.*, the RD. Due to the strong initial texture, where the [0001] axis of almost all grains lies perpendicular to the compression direction, basal slip can hardly occur during compression.

Fig. 4.2 shows EBSD images of the AZ31 samples with different compression strain. The samples are labeled as S1 (ε=0.0015), S2 (ε=0.015), S3 (ε=0.02) and S4 (ε=0.065), with regard to their strain.

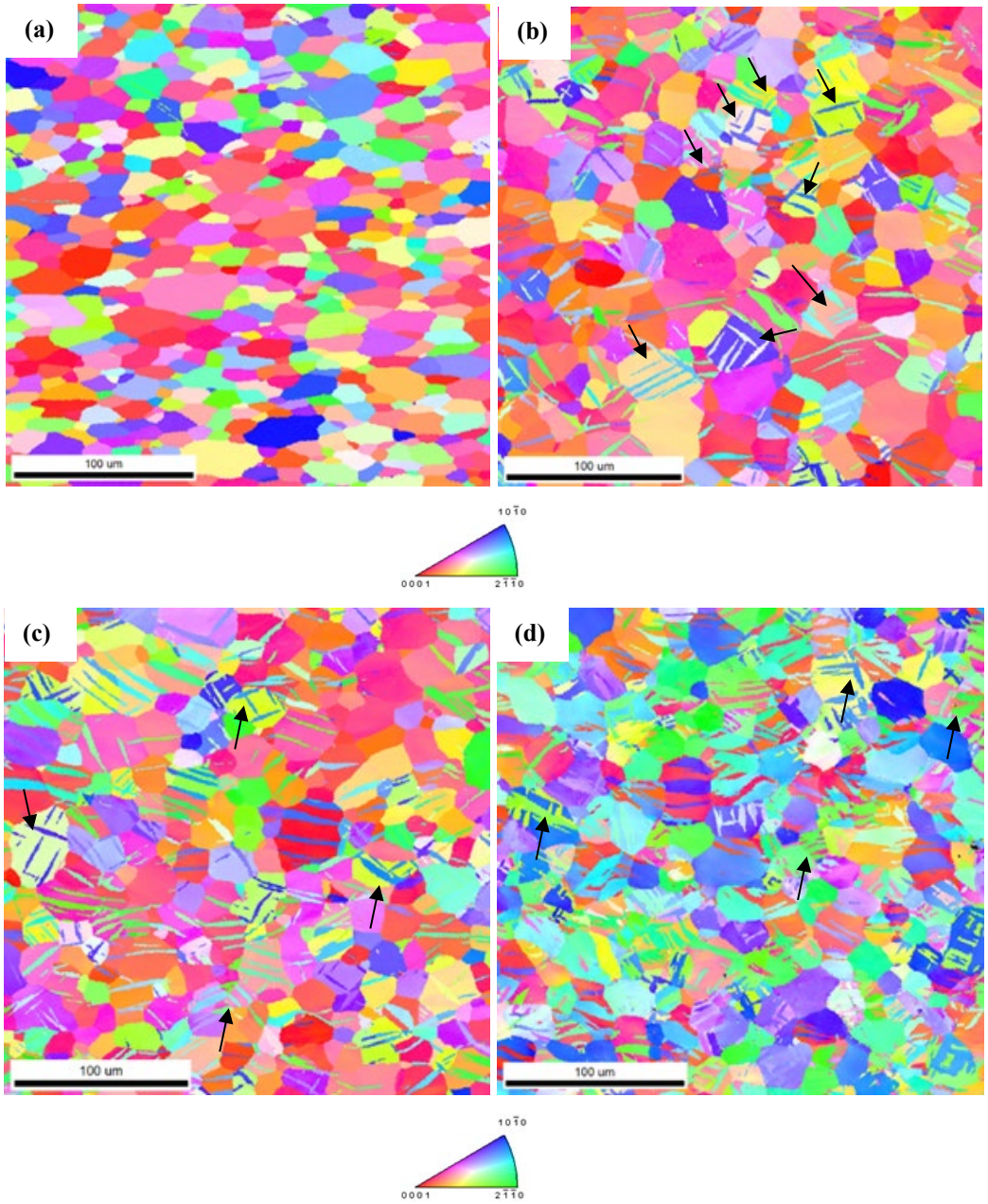

Fig. 4.2. EBSD images of the as-extruded AZ31 specimens with different strain: (a) ε=0.0015(S1); (b) ε=0.015(S2); (c) ε=0.02(S3); (d) ε=0.065(S4).

Since slip on the pyramidal plane can proceed only at a relatively high temperature (above 180 °C), the contribution of slipping to strain and stress can be neglected at all in the studied strain range. Therefore, the main deformation mode "left" to accommodate the strain is tensile twinning (see Section 3.4.). In fact, by further examining the misorientation angles of twin boundaries, the twins in Fig. 4.2 can be identified as tensile twins, since the tensile twin has a fixed orientation relation with the matrix, see Table 3.3. The relative activities of different

deformation modes will be studied by simulation in Chapter 6. As shown in Fig. 4.2 (a), even after a very small strain (0.15%), tensile twinning is activated in specimen S1. It is obvious from Fig. 4.2 (b) to (c) that almost all twins nucleate at the grain boundary (GB).

The local stress concentration at grain boundaries and the high number of grain boundary dislocations, which may dissociate into partial dislocations, make GB the favorable sites for twin nucleation. The twin number density and twin volume fraction is so small that the twining can hardly change the texture at this strain. As deformation commences, tensile twins become profuse in the sample, as shown in Fig. 4.2 (b) to (d), and a large amount of twin-twin joints were observed, as indicated by the black arrows in the Fig. 4.2. Twin-twin joints make the further growth of twins increasingly difficult. As a result, twin growth stops and the twin volume becomes saturated.

Under increased compression strain, in S4 (see Fig. 4.2 (d)), the twins are not only observed at the GB, but also between the two parallel pre-existed twins. This goes along with the assumption of previous research, where the nucleation of twins has been divided into two types, the one being the “normal nucleation” at the GB, the other representing the “interaction nucleation” stimulated by other twinning events [97]. The twin nucleation may be driven by the twin-twin interaction, which causes changes of the local stress field. These changes caused by twin-twin interaction can be quantified by simulation by full-field simulation methods, such as CPFEM or the phase field approach (ongoing research).

Fig. 4.3 illustrates the statistically calculated mean twin number per grain with increasing strain, obtained from the experimentally obtained EBSD data. As strain increases, the twin number increases drastically. The mean twin numbers per grain, N_T, raises rapidly with strain until it reaches a saturation value. By statistical calculation, N_T is 0.085 in S1 and saturates rapidly to 2.7 in S3. From Fig. 4.3, the increase of the twin number N_T stops at a strain of 2%, despite the fact that twin volume continues to experience a rapid increase beyond this strain, as shown in Fig. 4.2 (c) and (d). The statistically evaluated twin volume fraction from EBSD data of samples with different strain is used to validate the modeled twin volume fraction in the semi-empirical growth law presented in Section 4.5.

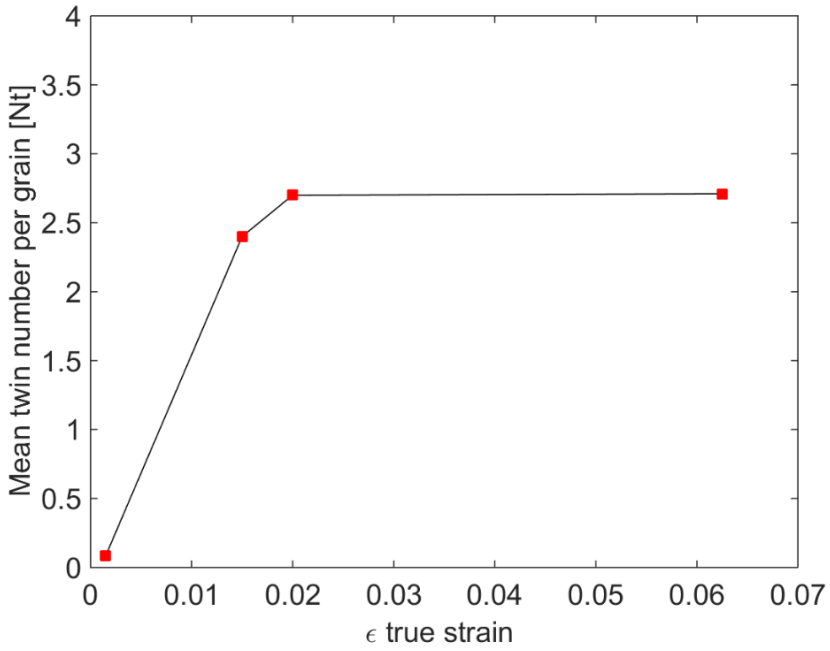

Fig. 4.3. Statistically calculated mean twin number per grain, N_t, in S1, S2, S3 and S4 from EBSD data.

4.2 Contribution of tensile twinning to strain

Based on this geometrical feature of twins, a simple model on the contribution of tensile twins to the strain accommodation under compression is postulated. Here, for simplicity, we neglect the effects of twin-twin interaction and assume that all the twins completely penetrate the grain. Fig. 4.4 shows the tensile twinning mode in the Mg lattice, which has the 'ABABABAB....' stacking order. According to the crystallographic features of tensile twins and the initial texture, the Taylor factor of tensile twins can be calculated.

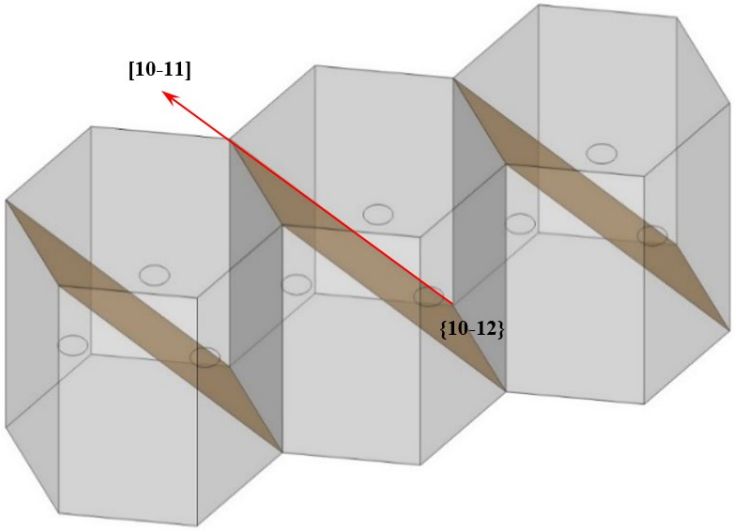

Fig. 4.4. The tensile twinning mode in Mg lattice: The 'B' layer atoms are schematically represented by the circles in the middle of the lattice.

The contribution of twinning to the strain can be expressed as

$$\varepsilon = \frac{\gamma_0}{M_t} f_T \ , \tag{4.1}$$

where f_T is the twin volume fraction, M_t is the Taylor factor and γ_0 is the specific shear of $\{10\bar{1}2\}<10\bar{1}1>$ tensile twinning, which equals 0.13. The $\{10\bar{1}2\}<10\bar{1}1>$ tensile twinning is the predominant mode in the present case. Therefore, the strain rate can be expressed as

$$\dot{\varepsilon} = \frac{d\varepsilon}{dt} = \frac{0.13}{M_t} \frac{df_T}{dt} \ . \tag{4.2}$$

An elliptic shape of deformation twins is often found by metallography of Mg. It is inferred here that the three-dimensional shape of deformation twins is oblate spheroid, in line with observations made in previous studies [97-99]. Then, the twin volume fraction follows as

$$f_T = N_T \cdot \frac{4\pi}{3}\left(\frac{l}{2}\right)^2 \cdot \bar{e} \Big/ \left[\frac{4\pi}{3}\left(\frac{\bar{d}}{2}\right)^3\right] , \tag{4.3}$$

where l is the twin length and $\bar{e}$ is the mean twin thickness. N_T is the mean twin number per grain, $\bar{d}$ is the mean grain size. N_T is defined as $N_T = n_t / n_g$, n_t is the total number of twins, and n_g is the total number of grains. $\bar{e}$ is defined as $\bar{e} = e_t / n_t$, with e_t being the total thickness of all twins. The twinning process is actually very fast. Brunton and Wilson have studied the kinetics of twinning in zinc and tin crystals, finding that the velocity of twin partial dislocations during twin formation can be as high as 600 m/s [100]. It is thus reasonable to assume that the twin transverses the whole grain instantaneously at the moment of onset of plastic strain. Consequently, the twin length l can be assumed equal to the mean grain size, and then Eq. (4.3) simplifies to

$$f_T = 2N_T \cdot \bar{e} / \bar{d} \ . \tag{4.4}$$

Eq. (4.4) indicates that the evolution of deformation twins can be considered solely dependent on the thickening of twins, and the strain rate can be rewritten as

$$\dot{\varepsilon} = \frac{d\varepsilon}{dt} = \frac{0.13}{M_t} \frac{d\left(2N_T \cdot \bar{e}/\bar{d}\right)}{dt} = \frac{0.26N_T}{M_t \cdot \bar{d}} \cdot \frac{d\bar{e}}{dt} + \frac{0.26\bar{e}}{M_t \cdot \bar{d}} \cdot \frac{dN_T}{dt} \ . \tag{4.5}$$

The physical meaning of Eq. (4.5) is that the contribution of deformation twinning to the strain in one crystal consists of two parts: (1) The nucleation of new twins, which possess a distinct, initial twin volume, indicated by the second term of Eq. (4.5) and (2) thickening of the twins, which corresponds to the growth of twins, indicated by the first term of Eq. (4.5).

4.3 Considerations on twin nucleation and twin thickening based on experimental observation

Dislocation theory suggests that nucleation and growth of deformation twins involves the cooperative motion of a large number of twin partial dislocations on the twin plane along the twin direction. The twin nucleation processes are driven by elastic energy release. Haitham [50] suggested that slipping or twinning will increase the stress field in the grain and this increasing stress field can be released by new twinning events. In line with these findings, we believe that newly formed twins merge with each other, resulting in extraordinarily thick twins(see Fig. 4.2 (d)). Since the resolution of EBSD is not sufficient to discern whether a twin is originated from one nucleus or several nuclei, the thickening process may be envisaged either as process following some order, in which each layer is added successively to the twin, or as the random accumulation of embryonic twin faults [71]. Twin nucleation is determined by dislocation reaction, therefore, it is reasonable to suppose that the number of nuclei at the onset of twinning is related to the dislocation density.

In the present hot-extruded specimens, the order of magnitude of dislocation density is between that for completely annealed metal ($\sim 10^{10}$ m^{-2}) and for typical cold worked crystal ($\sim 10^{16}$ m^{-2}). Therefore, the order of magnitude of dislocation length is about 10m in one grain in the present study (the grain size is about 20 μm). Previous research has estimated the order of magnitude of a critical radius of a twinning nucleus approximately 1~10 nm [71, 63]. On comparison of the dislocation length in one grain and critical twinning nucleus radius, it can be inferred that one grain can provide a large number of sites for potential twin nuclei. However, the experimentally observed mean twin number is orders of magnitude lower, only 2.7 on average in our present experiments. This indicates that only very few of the potential nuclei can experience the subsequent growth. As deformation proceeds, some nuclei may be activated locally, when the stress on them is sufficiently high to overcome the attraction of two partial dislocations bordering a stacking fault. In fact, the nucleation process of twins remains unclear due to the difficulty of its experimental examination. As an alternative and complementary way to experimental methods, modeling showed to be promising in unveiling the nucleation process of twins. Recently, a probabilistic model based on the famous Poisson distribution in statistical mechanics has been applied to study the nucleation of twins [15, 78].

Overall, the measured saturated twin number per grain is in the same order of magnitude as found in other studies [97]. As shown in the Fig. 4.3, the mean number of twins per grain becomes saturated in the very early stage of deformation, where the compression strain is about

2%. Therefore, the thickening or growth of twins is the main part of contribution of twins to strain accommodation compared with the nucleation after a strain over 2%. Fig. 4.5 displays the schematic representation of nucleation and growth of deformation twins by extracting and abstracting the main information of Fig. 4.2. Fig. 4.5 (a)-(b) schematically represent twinning in the early stage and Fig. 4.5 (c)-(d) the later stage.

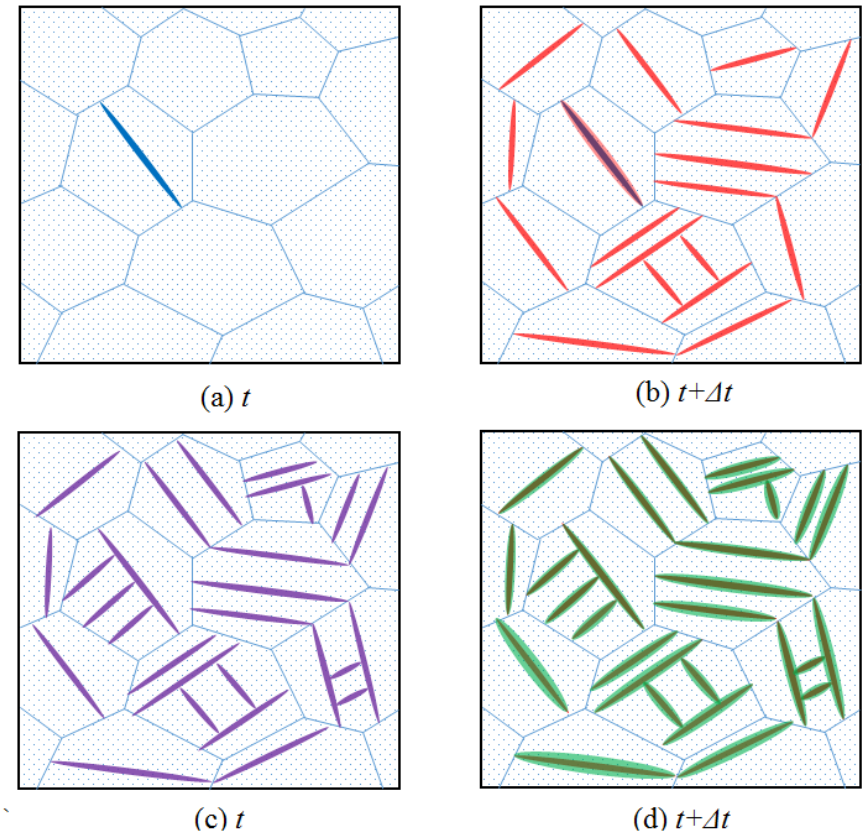

Fig. 4.5. Schematic representation of nucleation and growth of deformation twins: (a), (b) for nucleation and (c), (d) for growth.

Here we define the *early stage* of deformation when strain is less than 2%, the *later stage* of deformation when strain is large than 2%.

A large amount of new twins form (red in Fig. 4.5 (b)) during the interval of time Δt after initiation of twinning (Fig. 4.5 (a)), and it can be supposed that the number of these new twins is *n-1*. If these new twins have the same starting thickness, e_0, at the moment t, and the thickening of the initial twin can be neglected due to the short time interval Δt, then the mean twin thickness follows as

$$\overline{e}_{t+\Delta t} = \frac{e_1 + (n-1)e_0}{n} \approx e_0 \ . \tag{4.6}$$

where the e_1 is the thickness of initial twins ($e_1 \approx e_0$).

Eq. (4.6) suggests that the mean thickening rate would be zero at the earliest stage, and the contribution of the thickening of twins to strain can be ignored compared with the nucleation of new twins. The first term on the right side of Eq. (4.5) can be neglected in the early stage of deformation. Therefore, at the initial stage of deformation, the strain accommodation is mainly contributed by twin nucleation.

On the other hand, in the later stage of deformation, where the twin number does not change any more (due to the rapid saturation of the twin number per grain), the contribution of deformation twinning to strain accommodation stems solely from twin growth and can be simplified as

$$\dot{\varepsilon} = \frac{0.26 N_T}{M_t \cdot \bar{d}} \cdot \frac{d\bar{e}}{dt} \ . \tag{4.7}$$

4.4 Evaluation of the velocity of twin partial dislocations

4.4.1 Velocity of twin partial dislocations during twin nucleation

Defining t_0 as the time needed for the partial dislocations transmitting from one twinning plane to its adjacent twinning plane (during t_0, simultaneously, the partial dislocation sweeps the twinning plane at once), the area swept by a partial dislocation can be simplified as a circle with a constant radius R_c during this period. Thus, $t_0 = R_c/v$ follows, where v is the dislocation velocity. In Section 4.3, we have already assumed that the thickening rate of twins is zero in the earlier deformation stage (see Eq. (4.6)). Strictly speaking, this thickening rate is the "*instantaneous*" thickening rate. However, there is also an "*average*" thickening rate of twins. After a certain time period Δt, the twin nucleus emerges with an initial thickness e_0, then the "*average*" thickening rate of twins can be expressed as $e_0/\Delta t$. During this time period Δt, the partial dislocation sweeps over the twin plane for n times, thus Δt is equal to n times t_0. Meanwhile the twin thickness should be n times, where d_0 is the interspace of two adjacent twinning plane. Therefore, the "*average*" thickening rate of twins can be rewritten as

$$\frac{e_0}{\Delta t} = \frac{n \cdot d_0}{n \cdot t_0} = \frac{d_0}{R_c} v \ . \tag{4.8}$$

From this simple equation, the velocity of twin partial dislocations can be evaluated once the initial thickness of twins is measured (Fig. 4.2(a)).

Based on the present EBSD data, the *"average"* thickening rate is measured as 1.3×10^{-6} m/s. Inserting into Eq. (4.8) yields

$$\frac{d_0}{R_c} v = 1.3 \times 10^{-6} \text{ m/s} \tag{4.9}$$

and, with the interspace of two adjacent twinning planes, d_0=0.2 nm, and the radius of the circle swept by twin partial dislocation, R_c=20 μm, inserted in Eq. (4.9), a twin partial dislocation velocity of 0.13 m/s is obtained.

It should be noted that this value is actually much smaller than the twin dislocation velocity reported by J.H. Brunton, which was as high as 600 m/s [100]. However, these reference data was measured in etched Zinc and Tin. Further, it should be pointed out that determination of the dislocation velocity by using high-resolution experimental techniques, such as, *in-situ* TEM would be more reliable [63, 67]. Nevertheless, the calculated velocity value by the present, simple model (0.13 m/s) is also much higher than that of ordinary dislocations.

4.4.2 Velocity of twin partial dislocations for twin thickening

Fig. 4.6 shows the true strain rate of sample S4 during the compression test. In Fig. 4.6, the true strain rate fluctuates seriously during the earlier stage of deformation, this stage corresponding to the nucleation of tensile twins. In the later stage of deformation, the strain rate becomes much more stable except for a jump around 125 s due to some instabilities of the measurement (see Fig. 4.6). Nevertheless, the mean true strain rate in the later half deformation stage of deformation, excluding this incontinuity, is approximately 5×10^{-4} /s This true strain rate can be inserted into Eq. (4.7) to estimate the velocity of twin partial dislocation in the later stage of compression.

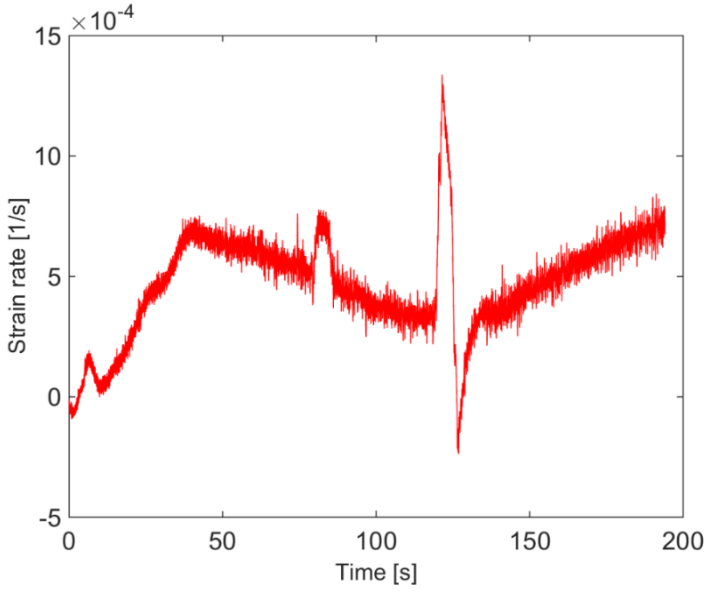

Fig. 4.6. The true strain rate of the sample S4 during compression test.

Since the mean twin number, N_T, is saturated and will not change, the contribution of twinning to the strain accommodation arises solely from thickening. Accordingly, Eq. (4.7) can be rewritten as

$$\dot{\varepsilon} = \frac{0.26 N_T}{M_t \cdot \overline{d}} \cdot \frac{d\overline{e}}{dt} = \frac{0.26 N_T}{M_t \cdot \overline{d}} \cdot \frac{d_0}{R_c} v \ . \tag{4.10}$$

Inserting $\dot{\varepsilon}$ =5×10^{-4} /s, $\overline{d}$ =20μm, N_t =2.7, d_0 =0.2 nm, R_c =20 μm and M_t =2 (reflecting the strong initial texture and supposing constant Taylor factor of twinning system in the matrix), the dislocation velocity is calculated as 1.4×10^{-3} m/s. This indicates that the twin partial dislocations velocity after N_t saturation is only 1/100 of that one before saturation. This considerable difference can be discussed in the light of free dislocation path. Before N_t becomes saturated, the twins have abundant space to grow. Furthermore, lack of twin-twin interaction suggests that the twin partial dislocations will not meet obstacles and can move freely (see Fig. 4.2 (a)). The considerably slower dislocation velocity after N_t saturation can be explained by twin-twin interactions, impeding the movement of twinning partial dislocations (see Fig. 4.2 (b)-(d)). When twins encounter each other, a twin-twin boundary forms, leaving the twinning dislocations of the incoming twin blocked by the twinning boundary and forming boundary dislocations by dislocations reaction [48]. The back-stress caused by the pile-up of these boundary dislocations is believed to be responsible for the impedance of motion of twinning partials.

The dislocation motion is considered as quasi-viscous when the drag resistance predominates, which happens if the dislocation speed is close to 10^{-2} of the speed of sound in materials [101]. Normally the order of magnitude of the speed of sound in metals at room temperature is 10^3 m/s. Therefore, the contribution of the deformation twin to strain rate follows as

$$\dot{\varepsilon} = \frac{0.26 N_T}{M_t \cdot \overline{d}} \cdot \frac{d\overline{e}}{dt} = \frac{0.26 N_T}{M_t \cdot \overline{d}} \cdot \frac{d_0}{R_c} v = \frac{0.26 N_T}{M_t \cdot \overline{d}} \cdot \frac{d_0}{R_c} v_0 \tau^m \exp\left(-\frac{Q}{RT}\right) . \tag{4.11}$$

This is similar to the power law of Eq. (3.63). Eq. (4.11) justify that the power law can be used in the study of the anisotropy and texture modeling of hcp metals, where deformation twinning happens.

4.5 Semi-empirical model of twin volume fraction evolution

In this section, a simple model is proposed to capture the twin volume fraction evolution. It takes into account the main observed characteristics of twin evolution after nucleation, twin thickening and twin volume saturation with strain. Hereby, we denote the volume fraction of twins as, f_{tw}, which is equal to V_{tw}/V_0. V_{tw} is the volume of twins and V_0 is the volume of the grain. If the crystal grain is completely twinned, which happens only theoretically (*i.e.*, the twin volume fraction reaches 100%), the corresponding twin shear strain, γ_{tw}, becomes the specific twin shear, which is 0.13 for the tensile twin $\{10\bar{1}2\}\langle\bar{1}011\rangle$ (see Table 3.3).

In order to build a semi-empirical model capturing twin growth, the following assumptions are made, in part being based on our experimental observations by EBSD:

1) The growth rate of the twins dV_{tw}/dt depends on the untwinned part of a grain $V_0\cdot(1-f_{tw})$. Apparently, the larger the untwinned volume (the *"free"* space for twin growth) is, the faster the twins grow. The larger the untwinned volume is, the easier the local stress by twinning can be relaxed. This local stress impedes the further growth of twins. In addition, the probability of the event of a twin-twin interaction is lower than in the grains with large untwinned volume. Here, the twin-twin interaction is assumed to impede the further growth of existing twins. For example, in the limiting case where there is no twin in one grain at one specific deformation moment, this grain will have the largest untwinned part, and there will be no twin-twin interaction in this grain at this moment.
2) The growth rate of the twins also depends on the twinned volume. It can be assumed that the whole untwinned volume $V_0\cdot(1-f_{tw})$ can be reserved for the further twin growth, but the untwinned volume can only in part be transformed into twins during twin grow. We assume that the remaining volume in the untwinned zone for the further growth of twins is $V_0\cdot(1-f_{tw})\cdot f_{tw}$.The probability of twinning event in the untwinned part per unit time is assumed to be α, which is assumed to be constant for simplicity and will be discussed later. During the infinitesimal time interval dt, the probability of twinning is then $\alpha\cdot dt$. Therefore, in the volume $V_0\cdot(1-f_{tw})\cdot f_{tw}$, the new twinned volume dV_{tw} during *dt* will be $\left[V_0\cdot(1-f_{tw})\cdot f_{tw}\right]\cdot\alpha$.

3) There is an initial twin volume fraction f_0 at the commencement of twin growth, which can be set as a very small number but not 0, because the twin nuclei also have a volume.

4) There is as saturated twin volume fraction f_s, which can be statistically evaluated from experiment (see Section 4.1).

These assumptions represent a sound simplification of the real case of twin growth and, importantly, imply that the rate of evolution of twin volume fraction $dV_{tw}/(V_0 dt)$ in one grain is not only dependent on the volume of the twinned part but also on the untwinned part. Then the following equation holds

$$\frac{dV_{tw}}{V_0 dt} = \frac{df_{tw}}{dt} = \alpha f_{tw}\left(1 - f_{tw}\right) , \tag{4.12}$$

where α is an a-priori unknown constant. Eq. (4.12) can be further reasoned by expanding the right side.

The derivative of Eq. (4.12) can be solved by separating variables and integration, and the solution is

$$f_{tw}(t) = \frac{1}{1 + \left(\frac{1}{f_0} - 1\right)\exp(-\alpha t)} \tag{4.13}$$

where f_0 represents the initial volume at the beginning of twin growth. There is another formulation which is similar to Eq. (4.13) (mathematically called "*S*" growth curve)

$$f(t) = \frac{A}{1 + \left(\frac{A}{B} - 1\right)\exp(-\alpha t)} , \tag{4.14}$$

where A and B are constants and $A > B$. It can be easily checked that A is the limit number of $f(t)$ when $t \to \infty$, while B is the limit number of $f(t)$ when $t \to 0$.

It should be noted that in the Eq. (4.13) the "limit" value of f_{tw} is 1 when t approaches infinity. However, this is not true. The saturated volume fraction of twins cannot reach 100%, and one should define a saturated twin volume fraction f_s which is smaller than 1, the twin volume faction then reads

$$f_{tw}(t) = \frac{f_s}{1 + \left(\frac{f_s}{f_0} - 1\right)\exp(-\alpha t)} . \tag{4.15a}$$

Replacing time t with the accumulated twin shear strain, γ_{tw} , Eq. (4.15a) becomes

$$f_{tw}(\gamma_{tw}) = \frac{f_s}{1+\left(\frac{f_s}{f_0}-1\right)\exp(-\alpha\gamma_{tw})} \quad . \tag{4.15b}$$

In order to examine the influence of parameter α , we prescribe parameters f_0 and f_s to 5×10^{-4} and 0.25, respectively and change the value of α. The shape of the calculated twin volume fraction curves are shown in Fig. 4.7, where the value of α corresponding to red, blue and green line are 400, 300 and 250, respectively.

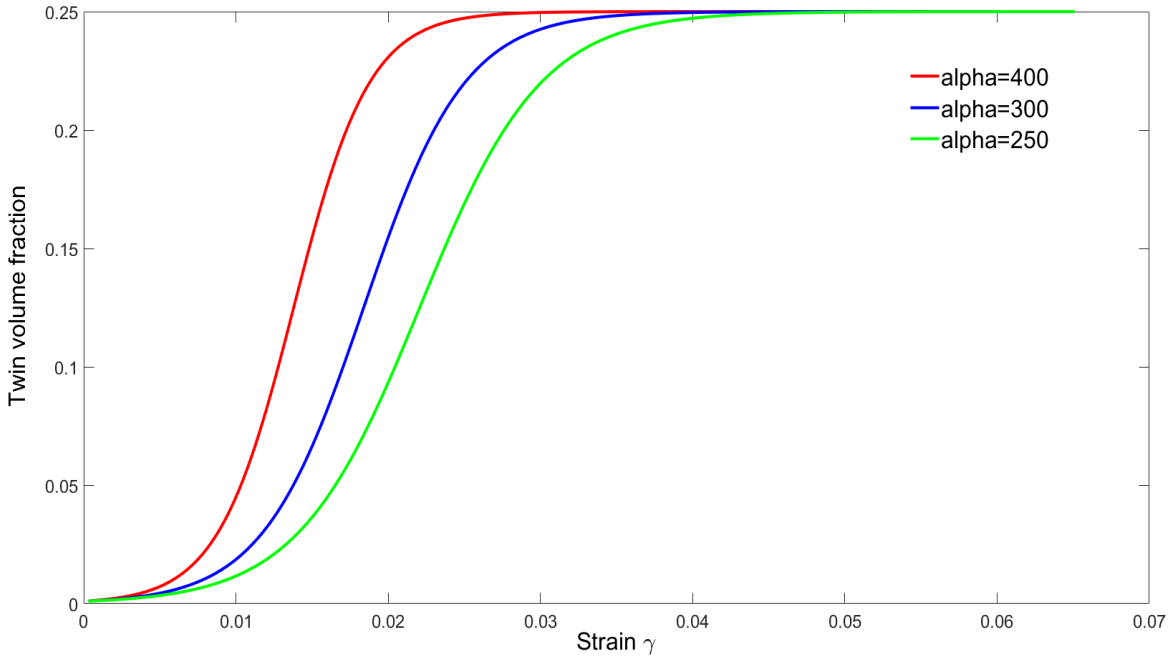

Fig. 4.7. The curve of twin growth with different parameters of α.

Eq. (4.15b) is used to fit the experimental data. Based on the EBSD data obtained by experiments, the volume fraction of twins is statistically calculated. The twin volume fraction f_{tw} was 0.0032, 0.26, 0.5, 0.63 and 0.79 at the compression strain of 0.005, 0.015, 0.02, 0.023 and 0.065, respectively. Fig. 4.8 shows the experimental twin volume fraction using Eq. (4.15), with fitted parameter α=340, f_0=0.001, and f_s=0.251.

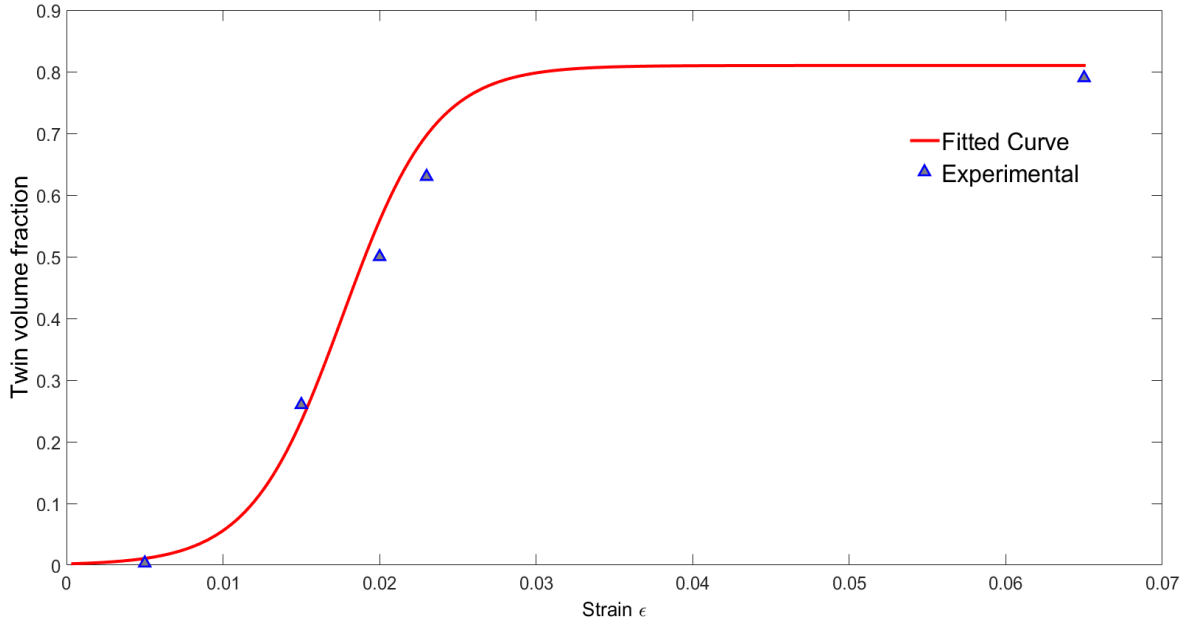

Fig. 4.8. The twin volume fraction evolution of sample S4.

This shows that, in principle, Eq. (4.15) can properly reflect twin growth for the experimentally tested strain range, thus confirming our preceding discussion on the relations among the twinned and un-twinned zones. The proposed twin growth function here is continuous and has less fitted parameters than usually required to capture the growth of twin volume fraction and can be extended for use in crystal plasticity modeling. For instance, Yuichi *et al.* [102] have studied the volume fraction of deformation twin in pure Mg by crystal plasticity modeling in pure Mg with resulting twin growth behavior being comparable to the present results. In contrast, they used a purely phenomenological equation to capture the growth of twin volume fraction, with a probabilistically determined threshold volume fraction.

The physics of α:

Indeed, some potential of improvement of the present growth function remains, particularly concerning the fitting parameter α in Eq. (4.15). Its physical meaning is, in essence, the speed of twin saturation. This is influenced by several factors, such as, the stress state, strain rate, temperature, grain size and the orientation. Among these, the resolved shear stress factors, τ , on the twinning plane is expected to play a major role, since it acts as the driving force for twin growth and is related to the stress state and the orientation of the grain. Larger resolved shear stress, thus corresponding to a faster saturation process of twin growth, will then relate to a larger value of the parameter α.

Temperature increase is expected to influence the twin evolution due to the thermal activation of twin dislocations (compare with Section 3.4.2, twin growth involves the cooperative motion of dislocations on the twin plane). Indeed, the motion of slip dislocations is assisted by temperature as well. Thus, the relative activities of twinning and slip will determine the temperature-dependent competition between slip and twinning. The stress for slip dislocation motion decreases with increasing temperature and the temperature-sensitivity of slip dislocations is larger than that of twin dislocations. Consequently, the activity of dislocation slip outweighs that of twinning above a critical temperature. Below the critical temperature, twinning is then the predominant deformation mode, which is confirmed by many studies [71]. The effects of temperature on the twin stress are a remaining debate. Both, positive and negative temperature dependence of twin stress, was reported [71]. The measured twin stress decreased slightly with decreasing temperature for most twin modes in hcp metals. However, in these studies [103], the distinction between stress during twin nucleation or twin growth has not pursued. The twin stress differs significantly between these two stages.

The dependence of α on grain size can be explained as follows. In the case of large grain size of polycrystals, twin saturation should be slower compared to smaller grain size, simply based on the lower probability of two twins to intersect with each other in the former case. De-twinning may also play a role in twin growth. The back-stress due to the twin-twin interaction and twin-grain boundary interaction is thought to be responsible for de-twinning [63, 67]

In fact, the stress state at twin joints is rather complex. In order to analyze the local stress caused by twin-twin joints, ongoing research employing full field methods is promising to "raise" α from a fitting parameter to an optimizable model variable.

4.6 Summary on tensile twinning in Mg alloy

1) The mean twin number per grain, N_t, saturates fast in present compression tests of AZ31 Mg alloys, indicating the significant role of twin-twin interactions. The small computed number of twin nuclei compared to the theoretically probable number suggests that only few twin nuclei were activated during compression testing.
2) Twin nucleation plays a dominant role in accommodating strain at the early deformation stage, where a large amount of new twins result in almost zero mean twin thickening rate. Twin growth dominates the accommodation of strain at later stages of deformation, *i.e.*, after the mean twin number per grain has reached its saturated value.
3) In the nucleation-dominated stage, the evaluated partial dislocation velocity by the present model is approximately 0.13 m/s. The velocity of twinning partial dislocation in the later

stage is only 1.4×10^{-3} m/s, indicating that the twin-twin interactions strongly affect the thickening of twins.

4) A semi-empirical twin growth law considering the initial twin volume fraction after nucleation and the saturated twin volume fraction is proposed. The growth factor α determines the speed of twin volume fraction increase. Microstructural and state parameters which influence the free path for twin partials movement will also influence α.

5 Weakening basal texture in AZ31 Mg alloy observed by experiment

Tensile twinning $\{10\bar{1}2\}<10\bar{1}1>$ is profuse in room temperature deformed Mg and its alloys, accommodating *c* axis strain during the deformation. The influence of deformation twinning on plasticity consists of two parts:

- Deformation twinning serves as supplementary room temperature deformation mode to basal slip.
- Deformation twinning provokes a strong reorientation effect on the lattice. $\{10\bar{1}2\}<10\bar{1}1>$ tensile twinning reorients the c axis by rotating round $<10\bar{1}0>$ direction by about 86°. By this reorientation, the resolved stress on the slip systems is influenced.

However, strain accommodation by deformation twinning is limited. Even if the grain is completely twinned by $\{10\bar{1}2\}<10\bar{1}1>$ tensile twinning, the plastic strain is calculated to be only 6.5%. As the easiest deformation mode at room temperature, basal slip plays a dominant role in accommodation of strain. This further means that, in order to obtain technologically desirable amount of plastic strain, basal slip has to be promoted as much as possible. Unfortunately, during deforming of Mg alloys at room temperature and even at elevated temperature, it tends to a strong basal texture, *i.e.*, all the c axis grains are oriented perpendicular to the extrusion axis or parallel with the normal direction in rolling.

The Mg alloy with strong basal texture has very poor deformability. In the previous compression tests reported in Section 4.1, further deformation becomes essentially impossible after strains above 10%. Moreover, cracks are initiated close to the compression strains of about 12%. The question of how to “weaken” the basal texture is thus of great significance for improving the deformability of Mg alloys. The addition of rare earth elements (REE) in Mg can significantly reduce the tendency of developing a basal texture [104], even though the underlying mechanism is not fully understood. However, the cost of RE is often too high for mass industry application. Reducing the twin number in samples via thermal mechanical treatment may pose a promising method to enhance deformability. In order to weaken the strong texture by recrystallization, proper heat treatments are intended to be designed. Studies on the influence of static and dynamic recrystallization on the texture evolution were conducted [105-108]. Modifying the basal texture by heat treatment is still challenging. The optimization of process parameters of heat treatment, time, the choosing of temperature is subtle. For instance, it was found that a large amount of tensile twins hardly change at medium temperature

annealing or only re-orientate by rotating around its *c* axis [106-108]. Even though, during high temperature annealing, tensile twinning disappeared, resulting in randomization of the *c* axis orientation of the Mg lattice,, this happened at the cost of appreciable grain coarsening. Hence, the best compromise has to be obtained between controlling grain size and basal texture elimination. In this framework, pre-straining represents a promising strategy to weaken the basal texture [109]. In this section, pre-strain was imposed on AZ31 Mg alloy to boost recrystallization of deformed samples and subsequently eliminate the undesirable strong basal texture. Pre-straining has been designed to initialize <c+a> pyramidal slip modes. The<c+a> dislocations have a longer Burgers vector than the basal dislocations and are expected to yield more distortion energy and, thus, a higher driving force for recrystallization.

5.1 Experimental

At 350 °C, hot extruded AZ31 magnesium alloy with strong initial fiber texture is chosen. Three different deformation modes are selected in order to investigate the influence of strain modes on the recrystallization process. Under the first deformation mode, the sample is directly compressed to a strain of 10% at 180 °C (S1). Sample S2 is also compressed to a strain of 10%, but with the first half strain (5%) performed at 180 °C and the second half strain (5%) subsequently performed at RT. For S3, the same overall strain is chosen as for the previous two samples, with the first half strain (5%) performed at RT and the second half strain (5%) performed at 180 °C. All samples are subsequently subjected to isothermal aging at 300 °C for 6 hours (S1H, S2H and S3H). An initially strong basal texture is found, as shown in Fig. 4.1 on page 44.

The following hypotheses assisted the choice of deformation paths and temperatures:

S1: A strain of 10% at the relatively high temperature of 180 °C is expected to promote high activity of <c+a> pyramid slip mode take place during the deformation [110].

S2: During the first half deformation at 180 °C, the <c+a> pyramidal slip mode should be activated, whereas the contribution of deformation twinning is supposed to be small. In the subsequent half strain, at RT, the tensile twin and basal slip are expected to become important, while the amount of <c+a> may be retained.

S3: At the first half strain, the main deformation mode is thought to be tensile twinning, in the following half strain, <c+a> pyramid slip is speculated to occur in both, matrix and twins,

and considerable amount of <c+a> dislocations may be stored in the previously formed tensile twin.

The subsequent isothermal heat-treatment step following the pre-strain was imposed on S1, S2, S3, yielding the sample SH1, SH2 and SH3, respectively. The compression tests are performed on a Gleeble 1500 machine with a strain rate of 10^{-3}/s. The texture evolution during heat treatment is examined by the EBSD technique (FEI Quanter 200 FEGSEM).

5.2 Texture modifications

5.2.1 Texture modifications after compression testing

Fig. 5.1 shows the pole figure and the EBSD image of samples S1, S2 and S3, respectively

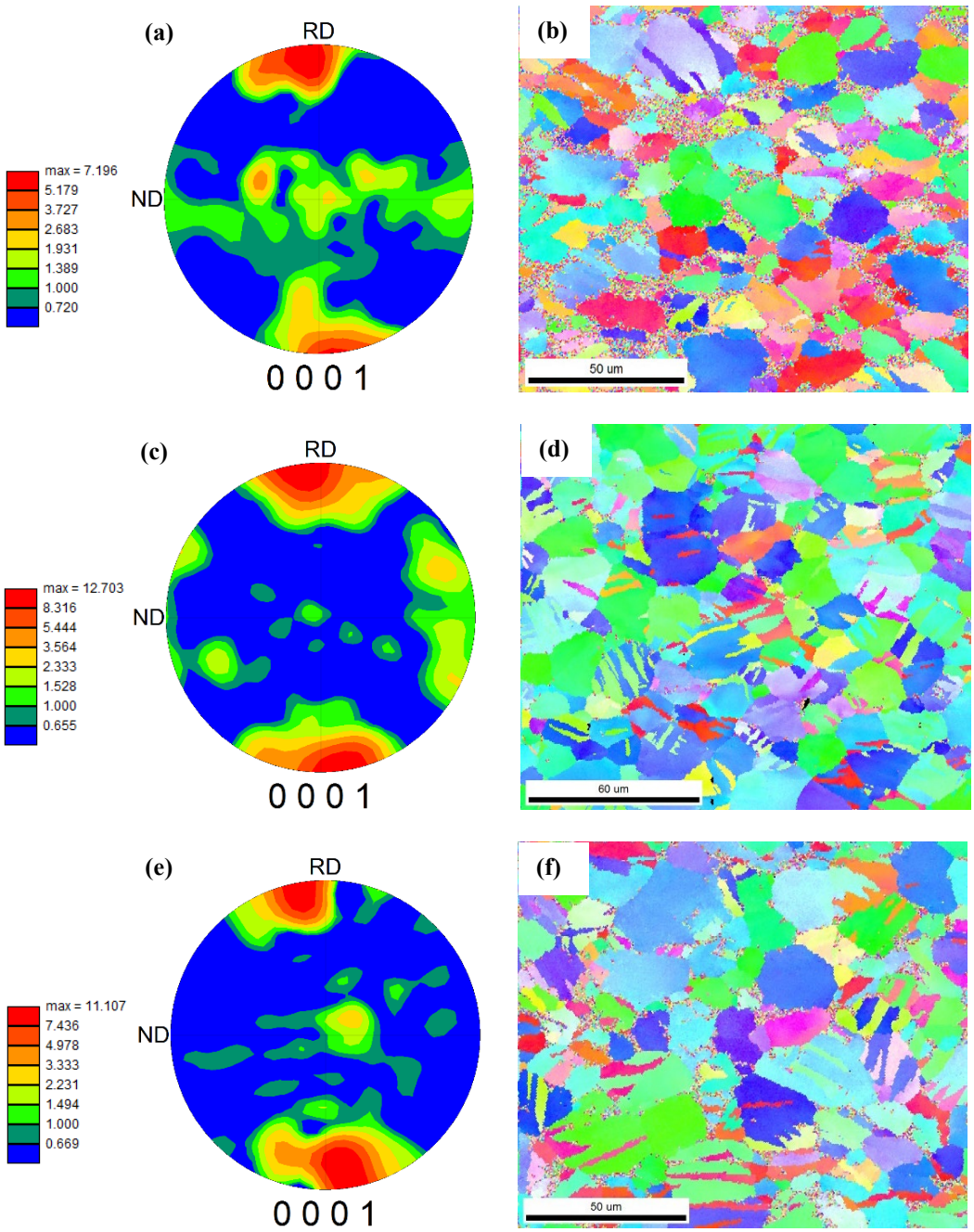

Fig. 5.1. Textures and microstructures of samples: (a) (b) S1; (c) (d) S2; (e) (f) S3.

In sample S1 (Fig. 5.1 (a)), tensile twins are observed in some of the grains. The grain size distribution of those grains being twinned is relatively heterogeneous. Compared with the RT compression shown in the Fig. 4.2 on page 46, the twin number is much smaller. The number

of twin-twin joints is reduced relative to the number after RT compression due to the competing activity of <c+a> pyramidal slip. Due to active <c+a> pyramidal slip, the grain orientation is partially changed. The pole figure of S1 shows that the *c* axis of some grains is aligned with the RD (compression axis of compression tests), while the *c* axis of remaining grains being almost perpendicular to the RD, distributing around the equator of the projection sphere. During compression, the normal of the pyramidal plane, acting as the slip plane of the <c+a> slip, tends to align with the compression axis, making the c axis disperse around the equator. Even slight tilt of the *c* axis, even approx. 1 to 2° (see Chapter 6) relative to the compression axis, seems to reduce the probability of the simultaneous activation of different twin variants in the grains, as revealed by reduced twin-twin interactions. Such effects of the initial orientation of grain crystal on selection of tensile twin variant will be simulated in Section 6.1.

The texture comparison between 180 °C compression and RT compression is shown in Fig. 5.2. In the case of RT compression, the scattering distribution of the *c* axis is lower than that in the 180 °C compression, suggesting the much lower activity of <c+a> slip. In RT compression, the initial texture of the samples is such that the *c* axis of most grains is almost perpendicular to the compression axis. The Schmid factors of different tensile twin variants, in this case, are the same, resulting in the same possibility of activation for different twin variants. Therefore, different twin variants are very likely activated simultaneously, provoking twin-twin intersect joints.

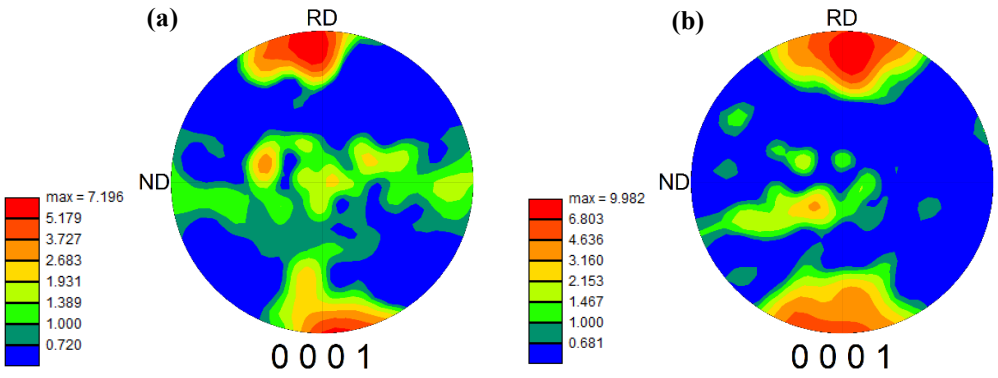

Fig. 5.2. Texture resulting from (a) 180 °C compression(strain=10%) S1 and (b) RT compression (strain=6.5%).

Fig. 5.1 (d) shows the EBSD images of S2. Pronounced twinning is observed in S2 compared with S1. During the first half strain of 5% compressed at 180 °C, the <c+a> pyramidal slip takes place, making the pyramidal slip plane tend to be perpendicular with the

compression axis and, equivalently tilting the *c* axis slightly. After this first half deformation, the *c* axis of most grains is not perpendicular with the compression axis any more. In the next half compression at RT, these grains with tilted *c* axis experience tensile twinning. Therefore, the Schmid factors for different tensile twin variants in these grains are different, making their simultaneous activation difficult. This is supported by the evidence of only few observed twin-twin insect joints (Fig. 5.1 (d)). Most twins are parallel with each other. The pole figure of S2 is clearly different from the one of S1. The center zone of the pole figure of S2, as shown in Fig. 5.1 (c), is obviously blank, while there is a scattering distribution of *c* axis for S1, as seen in Fig. 5.1 (a). This can be ascribed to tensile twinning during the second half compression at RT in S2. Tensile twins, thereby, reorient those grains whose initial *c* axis was located in the center of the projection circle to a new orientation where their c axis aligns with the compression axis. In addition, a weak texture component can be extracted from Fig. 5.1 (d), likely caused by basal slip during the second half compression at RT. Basal slip may act in those grains that inherited a favorable orientation after the first half compression at 180 °C.

Fig. 5.1 (f) shows the EBSD image of sample S3. Obviously, S3 and S2 have similar microstructures. Twin fraction, distribution and morphologies are similar in S2 and S3, *i.e.* most of the twins are parallel to each other and twin-twin interaction rarely occur. Still, S3 exhibits a different texture than S2, as shown in Fig. 5.1 (e). The texture of S3 is indeed very similar to that of the sample compressed at RT to 6.5%, which is also illustrated in Fig. 5.3. In the first half RT compression (5%) of S3, the *c* axis of most grains is reoriented and aligned with the compression axis. In the subsequent half 180℃ compression (5%), the texture is almost unchanged, indicating that the <c+a> pyramidal slip $\{2\bar{1}\bar{1}2\}\langle\bar{2}113\rangle$ has limited effects on the texture evolution in this case.

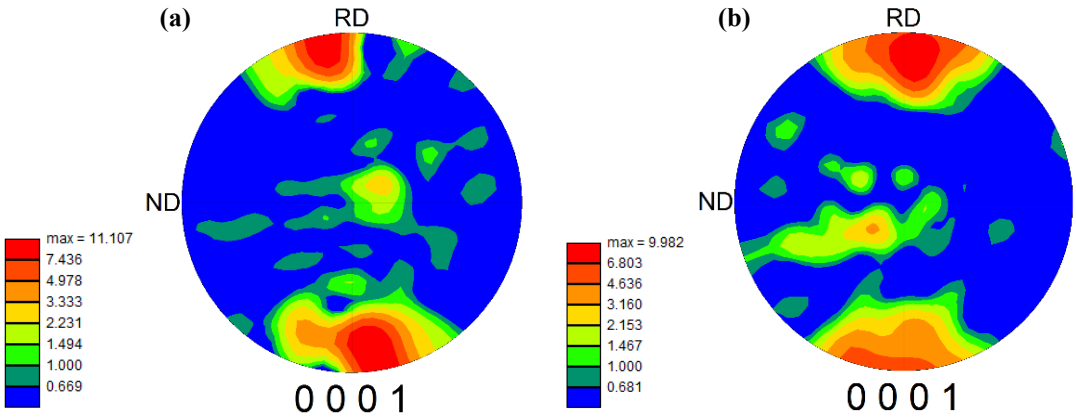

Fig. 5.3. Texture of (a) S3 and (b) RT compression samples (strain=6.5%).

5.2.2 Effects of heat-treatment

EBSD images of SH1, SH2 and SH3 are shown in Fig. 5.4. As a result of the isothermal heat-treatment, twins disappear in all these three samples. SH1 shows obviously larger mean grain size than SH2 and SH3.

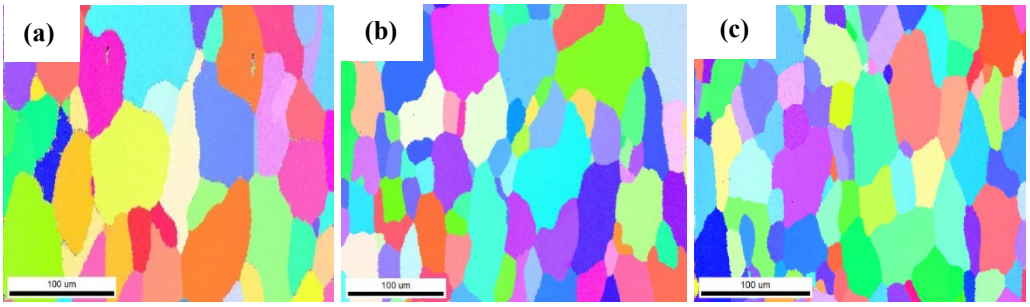

Fig. 5.4. The EBSD microstructure of samples: (a) SH1, (b) SH2, (c) SH3.

In SH1, SH2 and SH3, some fine grains are enclosed by coarse grains. The mean grain size of SH1 is obviously larger than of S1, while the grains of SH2 and SH3 experience no significant growth during isothermal annealing at 300 °C. Large <c+a> pyramidal slip activity in S1 has larger strain accommodation ability than tensile twin, resulting in higher storage capacity for distortion strain energy in the crystal, leading to the higher driving force for recrystallization. This is reflected by the larger mean grain size of SH1 compared to the other samples. Furthermore, since grain boundary mobility is considered to be impeded by tensile twins, this influence should be lower in S1. The present texture analysis is actually qualitative. The quantitative study of the relative activities of different deformation via the crystal plasticity simulation will be conducted in Chapter 6.

5.2.3 Texture comparison of as-compressed and heat-treated samples

Fig. 5.5 shows the texture comparison between SH1, SH2, SH3, as well as S1, S2, S3. After heat-treatment, the texture experiences a significant change due to recrystallization of deformed grains for S1.

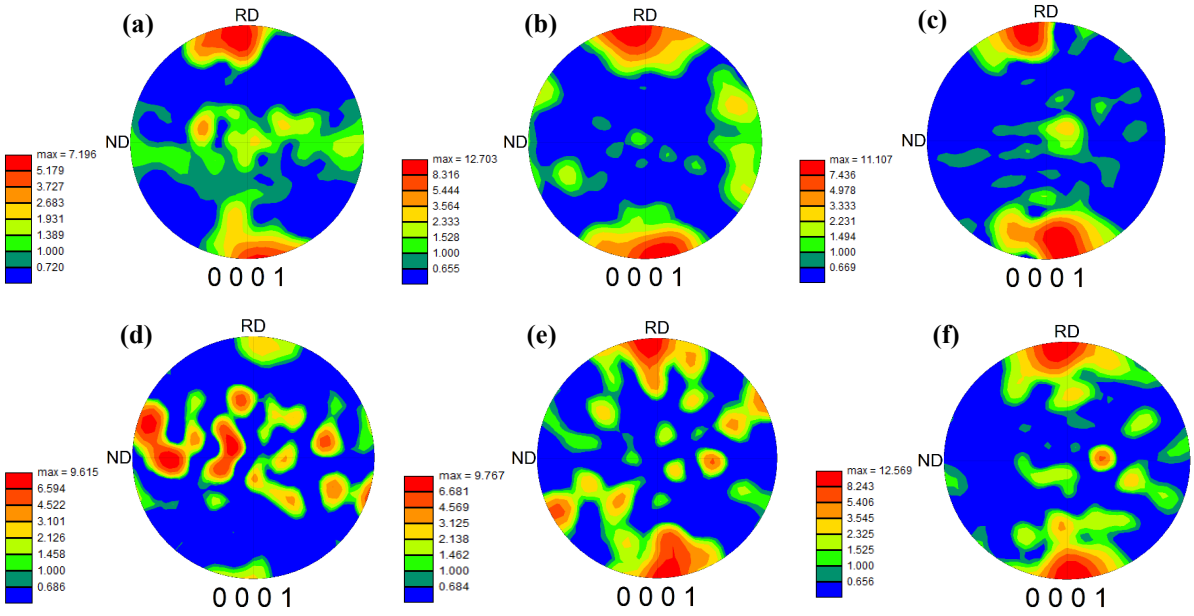

Fig. 5.5. The texture comparison between samples: (a) S1; (b) S2 and (c) S3; (d) SH1; (e) SH2 and (f) SH3.

The smallest texture change occurred in S3 during heat-treatment. In Fig. 5.5 (a) and Fig. 5.5 (d), the texture component located in the center of the pole figure represents the matrix, while the texture components locating along the RD represents tensile twins. The relative intensity between twin and matrix has changed significantly after heat-treatment. The comparison between Fig. 5.5 (a) and Fig. 5.5 (d) suggests that, after heat-treatment, the tensile twin is absorbed by the matrix and the texture is disperse in the center part of the pole figure. In S1, the number and volume fraction of twins is significantly less than in samples S2 and S3. The volume of the twinned zone is obviously smaller than that of the untwined zone in S1 (see Fig. 5.1 (b)) and more distortion energy is stored in untwined part. Therefore, in the subsequent heat treatment, the twin boundary emigrated toward the side of the twins and then these tensile twins appears to be “eaten up” by the matrix.

The sharpness of the tensile texture of SH2 is weaker than that of S2, a new texture component arises during isothermal annealing, and the texture seems to become more randomized. This indicates that, after the heat-treatment, only a part of the tensile twins are transformed into new grains with new orientation.

In SH3, the sharpness of texture corresponding to tensile twinning is slightly enhanced compared to S3, and no new texture components arise. This experimental observation suggests that, during heat-treatment, the matrix partially transforms into tensile twins, which is just the opposite trend than in SH1. In S3, a large amount of tensile twins was formed at the first half compression conducted at RT. During the second half compression (5%) at 180 °C, these tensile

twins, together with the matrix, experience <c+a> pyramidal slipping. This likely results in a relatively high stored distortion energy in the twins, allowing for twin boundary migration into the matrix during isothermal aging.

Summarizing, textures and microstructures of heat-treated samples, SH2 reveals more random texture and favorable grain size, SH3 reveals the sharpest structure, whereas SH1 has the largest mean grain size.

6 Mean field-simulation of texture and yield strength evolution

In this chapter, the anisotropy of single crystal Mg is described by calculation of the activation stresses for different deformation modes in the framework of Schmid´s law (Section 6.1). Mg exhibits strong anisotropy and the simulation results confirm that basal slip is the easiest deformation mode in Mg at room temperature. The reorientation of slip and tensile twinning in single crystals is also simulated, the results supporting the subsequent discussion in Section 6.2. Based on the knowledge introduced in Section 3.1, the texture evolution of polycrystalline Mg is simulated in the framework of the iso-work mean field method (Section 6.2). The conceptual limitations of this method are overcome by the development of a Taylor mean field model, which is applied for the simulation of texture evolution, relative activity and flow curve of as-extruded AZ31 Mg is simulated in Section 6.3.

6.1 Crystal Plasticity Framework for single crystal Mg

6.1.1 Anisotropy of yield stress

In calculating the yield stress of single crystal Mg based on the Schmid´s law, the commonly used four axial coordinates of hcp crystals are transformed into three orthogonal axes, first. In the present work, all crystal plasticity calculations are performed in the Cartesian coordinates system. Usually, the $\mathbf{a}_1$ axes $[2\bar{1}\bar{1}0]$, $[01\bar{1}0]$ and the **c** axis [0001] of the four-axial coordinate system are used as **X**, **Y** and **Z** axes of the three-axial coordinate system, which is shown in Fig 6.1.

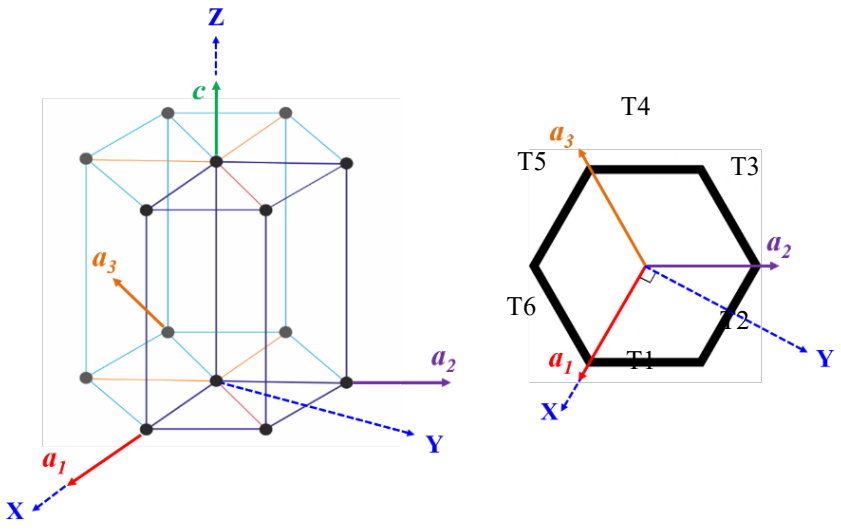

Fig. 6.1. Schematic representation of coordinate transformation from 4 axial coordinates to 3 axial coordinates.

The index of one lattice direction ***d*** in the three orthogonal axial coordinate system **X-Y-Z** can be transformed from its index in the four axial coordinate system (**a**$_1$-**a**$_2$-**a**$_3$-**c**), the transformation rule follows:

$$\begin{bmatrix} U \\ V \\ W \end{bmatrix} = \begin{bmatrix} 1/2 & 0 & 0 \\ \sqrt{3}/2 & \sqrt{3} & 0 \\ 0 & 0 & c/a \end{bmatrix} \begin{bmatrix} u \\ v \\ w \end{bmatrix}, \tag{6.1}$$

where [U V W] is the index of lattice direction ***d*** expressed in the **X-Y-Z** coordinate system and [u v t w] is its index expressed in *four* axial coordinates. t= -(u+v) and t is not an independent component of four indexes. In Mg, c/a is 1.6242, thus, the transformation matrix **Q** can be expressed as

$$\boldsymbol{Q} = \begin{bmatrix} 1/2 & 0 & 0 \\ \sqrt{3}/2 & \sqrt{3} & 0 \\ 0 & 0 & 1.624 \end{bmatrix}. \tag{6.2}$$

Similarly, the transformation between the indices of a lattice plane ***p*** expressed in **X-Y-Z** coordinates and a *four* axial coordinate system (**a**$_1$-**a**$_2$-**a**$_3$-**c**) can be written as

$$\begin{bmatrix} H \\ K \\ L \end{bmatrix} = \begin{bmatrix} 1 & 0 & 0 \\ 1/\sqrt{3} & 2/\sqrt{3} & 0 \\ 0 & 0 & a/c \end{bmatrix} \begin{bmatrix} h \\ k \\ l \end{bmatrix}, \tag{6.3}$$

where (*H K L*) represents the indices of lattice plane ***p*** expressed in **X-Y-Z** coordinates and (*h k i l*) are its indices expressed in the *four* axial coordinate system (**a**$_1$-**a**$_2$-**a**$_3$-**c**). i= -(h+k) and i is not an independent component of four indices. For Mg, the transformation matrix ***S*** is expressed as

$$\boldsymbol{S} = \begin{bmatrix} 1 & 0 & 0 \\ 1/\sqrt{3} & 2/\sqrt{3} & 0 \\ 0 & 0 & 1/1.6242 \end{bmatrix}. \tag{6.4}$$

With this transformation matrix known, the yield stress can be calculated for Mg single crystal at room temperature.

Fig. 6.2 illustrates the yield strength of single crystal Mg with different orientations. For simplification, here, only basal slip is considered first, which comprises three variants: (0001) $[2\bar{1}\bar{1}0]$, (0 0 0 1)$[\bar{1}2\bar{1}0]$ and (0 0 0 1) $[\bar{1}\bar{1}20]$, denoted here as B1, B2 and B3. The critical shear stress, τ_c, for basal slip is set to be 0.8 MPa (refer to Table 3.2). Here, the Kocks definition of Euler angles is chosen. Ψ and Φ are fixed to zero and θ varies from 5° to 85°. When θ approaches

0° or 90°, the yield stress approaches infinity. It is apparent that the crystal with orientation of λ and φ being 45° has the lowest yield strength.

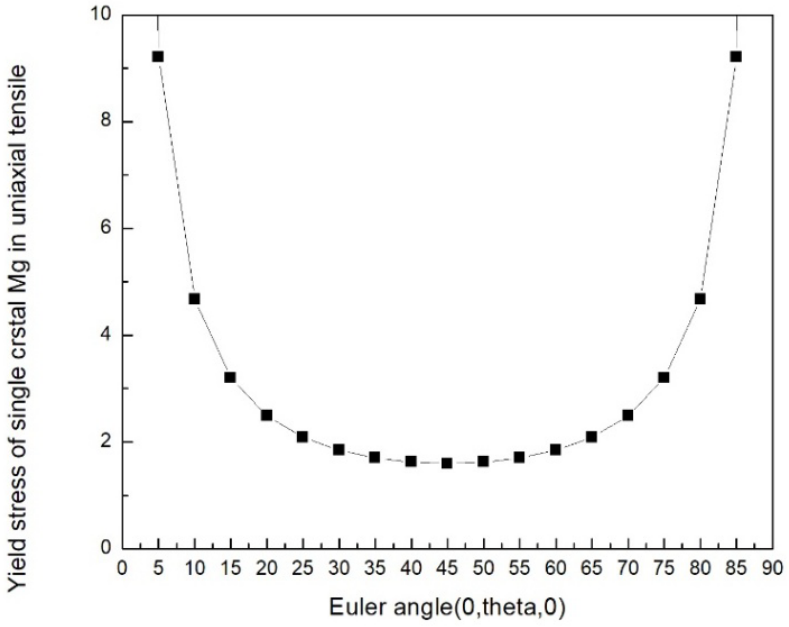

Fig. 6.2. Yield stress(MPa) of single crystal Mg in uniaxial tension with only the basal slip systems considered.

It is well known that five deformation mechanisms can act in Mg, *i.e.*, slip $\{0001\}\langle 2\bar{1}\bar{1}0\rangle$, prismatic slip $\{10\bar{1}0\}\langle 2\bar{1}\bar{1}0\rangle$, 2nd order pyramidal slip $\{2\bar{1}\bar{1}2\}\langle\bar{2}113\rangle$, tensile twinning $\{10\bar{1}2\}\langle\bar{1}011\rangle$ and compression twinning $\{10\bar{1}1\}\langle\bar{1}012\rangle$. When calculating the yield stress of single crystal Mg, all of these five mechanisms should be considered. Crystallographically, this yields 24 types of deformation variants in total, which are listed in Table 6.1 including slip planes and slip directions. Accordingly, the basal slip system has three variants, the prismatic slip system has three variants, and the 2nd pyramidal slip, tensile twin and compression twin system have six variants, respectively. Table 6.1 also summarizes the Miller indices of all slip systems and twin variants in the usual deformation modes of Mg. The expression of all these deformation modes can be conveniently transformed from the four index scheme to three indices based on Eqs. (6.1)-(6.4).

Table 6.1 Deformation variants in Mg

Deformation modes	Miller Index					
Basal sip	B1: (0001) $[2\bar{1}\bar{1}0]$		B2: (0001) $[\bar{1}2\bar{1}0]$		B3: (0001) $[\bar{1}\bar{1}20]$	
Prismatic slip	P1: $(01\bar{1}0)[\ 2\bar{1}\bar{1}0]$		P2:$(\ 10\bar{1}0)$ $[\bar{1}2\bar{1}0]$		P3: $(1\bar{1}00)$ $[\bar{1}\bar{1}20]$	
2nd pyramidal slip<c+a>	PY1: $(2\bar{1}\bar{1}2)$ $[2\bar{1}\bar{1}\bar{3}]$	PY2: $(11\bar{2}\bar{2})$ $[11\bar{2}\bar{3}]$	PY3: $(\bar{1}2\bar{1}2)$ $[\bar{1}2\bar{1}\bar{3}]$	PY4: $(\bar{2}112)$ $[\bar{2}11\bar{3}]$	PY5: $(\bar{1}\bar{1}22)$ $[\bar{1}\bar{1}2\bar{3}]$	PY6: $(1\bar{2}12)$ $[1\bar{2}1\bar{3}]$
Tensile twin	TT1:$(10\bar{1}2)$ $[\bar{1}011]$	TT2: $(01\bar{1}2)$ $[0\bar{1}11]$	TT3: $(\bar{1}102)$ $[1\bar{1}01]$	TT4: $(\bar{1}012)$ $[10\bar{1}1]$	TT5: $(0\bar{1}12)$ $[01\bar{1}1]$	TT6: $(1\bar{1}02)$ $[\bar{1}101]$
Compression twin	CT1:$(10\bar{1}1)$ $[10\bar{1}\bar{2}]$	CT2: $(01\bar{1}1)$ $[01\bar{1}\bar{2}]$	CT3: $(\bar{1}101)$ $[\bar{1}10\bar{2}]$	CT4: $(\bar{1}011)$ $[\bar{1}01\bar{2}]$	CT5: $(0\bar{1}11)$ $[0\bar{1}1\bar{2}]$	CT6: $(1\bar{1}01)$ $[1\bar{1}0\bar{2}]$

The τ_c values for basal slip, prismatic slip, 2nd order pyramidal slip, tensile twinning and compression twinning are chosen as 0.8 MPa, 39 MPa, 44 MPa, 2 MPa and 88 MPa, respectively (refer to Table 3.2 on page 29).

Tensile yield stress:

Fig. 6.3 shows the yield stress of single crystal Mg in uniaxial tension with all deformation mechanisms considered (red curve), compared to the yield stresses calculated with basal slip only (black curve). It can be seen from Fig. 6.3 that the yield stress values are the same as those depicted in Fig. 6.2 for the same orientations, except in the orientations with θ equals to 5°, 10° and 85°. The according difference arises from the activation of tensile twinning. In these three orientations, the tensile twinning is easier to be activated than basal slipping. In Fig. 6.3, as in Fig. 6.2, the yield stress of single crystal Mg shows remarkable differences with varying orientations, indicating the strong mechanical anisotropy of single crystal Magnesium.

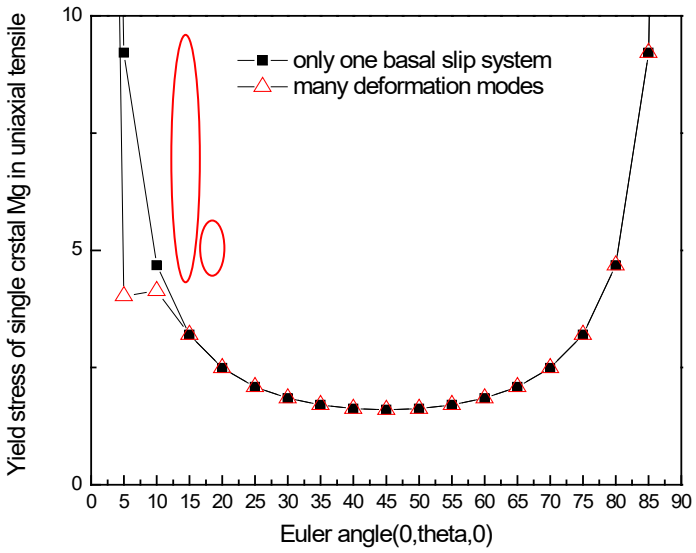

Fig. 6.3. Yield stress of single crystal Mg in uniaxial tensile with all deformation mechanisms considered

In order to represent the mechanical anisotropy of single crystal Mg in a more convenient way, the yield stress is plotted in Fig. 6.4 along three typical directions, $[2\bar{1}\bar{1}0]$, $[10\bar{1}0]$ and $[0001]$. The corresponding Euler angles are (Ψ=0°, θ=90°, φ=180°), (Ψ=0°, θ=90°, φ=210°) and (Ψ=0°, θ=0°, φ=0~360°), respectively. Fig. 6.4 shows that the tensile yield stresses are different when uniaxial tensile stress (the stress tensor has only one axial component , σ_{zz} is non-zero) is applied along these three directions.

The tensile yield stress along $\langle 0001 \rangle$ direction is calculated to be 4 MPa and is related to tensile twinning $\{10\bar{1}2\}\langle\bar{1}011\rangle$. Indeed the possibility of the 6 variants of tensile twins $\{10\bar{1}2\}\langle\bar{1}011\rangle$ being activated is the same because the six fold symmetry of Magnesium single crystal. The calculated tensile yield stress along $\langle 2\bar{1}\bar{1}0 \rangle$ direction is 90 MPa, which corresponds to the activation of the prismatic slip systems. When single crystal experiences a tensile along $\langle 10\bar{1}0 \rangle$, the yield stress is also 90 MPa, and the prismatic slip system will be activated. Fig. 6.4 reveals that single crystal Magnesium exhibits very strong anisotropy when subjected to tensile test.

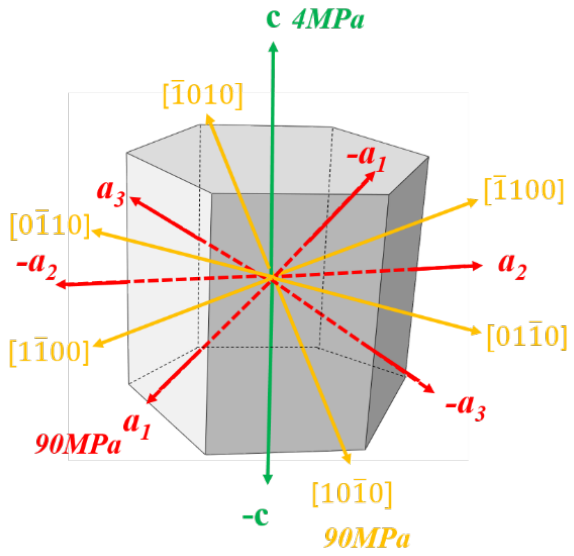

Fig. 6.4. The tensile yield stresses of single crystal Magnesium along the three directions ([2$\bar{1}\bar{1}$0], [10$\bar{1}$0] and[0001]).

In Table 6.2 (a), the tensile stresses needed to activate all 24 deformation variants are listed, assuming that the tensile stresses are applied along [2$\bar{1}\bar{1}$0]. It can be seen from Table 6.2 (a) that the tensile stress needed to activate the basal slip is infinitive, simply because the stress direction is parallel with the basal plane. In terms of prismatic slip, the stress for activating P1 (P=prismatic) (01$\bar{1}$0)[2$\bar{1}\bar{1}$0] variants is infinitive, while the stress for P2: (10$\bar{1}$0) [$\bar{1}$2$\bar{1}$0] and P3: (1$\bar{1}$00) [$\bar{1}\bar{1}$20] is the same, which is 90.06 MPa. The slip direction of the P1 variant coincides with the tensile direction, resulting in no resolved stress on the P1 slipping plane. As, for P2 and P3, their slip planes are symmetric relative to the $\mathbf{a}_1$ direction. The 2nd pyramidal (PY) slip has 6 variants, for intrinsic symmetry reason of the lattice, the stress for PY1: (2$\bar{1}\bar{1}$2) [2$\bar{1}\bar{1}$3] and PY4: ($\bar{2}$112)[$\bar{2}$113] are the same, which are 98.5 MPa. Besides, PY2:(11$\bar{2}$2)[11$\bar{2}\bar{3}$], PY3: ($\bar{1}$2$\bar{1}$2) [$\bar{1}$2$\bar{1}\bar{3}$], PY5: ($\bar{1}\bar{1}$22)[$\bar{1}\bar{1}$2$\bar{3}$] and PY6: (1$\bar{2}$12)[1$\bar{2}$1$\bar{3}$] have the same activating tensile stress value of 394.2 MPa, being substantially larger than for PY1 and PY4. The tensile twinning will not be activated under this orientation because of the mono-directional feature of twinning, *i.e.*, twin shear can only happen in one direction but not in its opposite direction. Nevertheless, compression twinning can take place. For symmetry reason, the CT1 (compression twinning): ($10\bar{1}1$)[$10\bar{1}\bar{2}$], CT3: ($\bar{1}101$)[$\bar{1}10\bar{2}$], CT4: ($\bar{1}011$)[$\bar{1}01\bar{2}$], CT6: (1$\bar{1}$01)[1$\bar{1}$0$\bar{2}$] has the same activation stress, which is 282.6 MPa, while the stresses for CT2: (01$\bar{1}$1)[01$\bar{1}\bar{2}$] and CT5: (0$\bar{1}$11)[0$\bar{1}\bar{1}\bar{2}$] are infinitive.

When extending the single-crystal Mg along $[10\bar{1}0]$ direction, as shown in Table 6.2 (b), the tensile stress needed to activate the basal slip is infinitive. The stress for activating P2: $(10\bar{1}0)$ $[\bar{1}2\bar{1}0]$ is infinitive, while the stress for P1 $(01\bar{1}0)[2\bar{1}\bar{1}0]$ and P3: $(1\bar{1}00)[\bar{1}\bar{1}20]$ is 90.06 MPa. PY1: $(2\bar{1}\bar{1}2)[2\bar{1}\bar{1}\bar{3}]$, PY2:$(11\bar{2}2)[11\bar{2}\bar{3}]$, PY4: $(\bar{2}112)[\bar{2}11\bar{3}]$ and PY5: $(\bar{1}\bar{1}22)[\bar{1}\bar{1}2\bar{3}]$ have the same activating stress of 131.4 MPa, which is much smaller than that in the case of extending along $[2\bar{1}\bar{1}0]$ (394.2 MPa). Similar to the case in Table 6.2 (a), tensile twinning is absent at this orientation. All of the compression twin variants have finite stress values, activation stress for CT1: $(10\bar{1}1)[10\bar{1}\bar{2}]$ and CT4: $(\bar{1}011)[\bar{1}01\bar{2}]$ are the same, which is 211.9 MPa, for CT2: $(01\bar{1}1)[01\bar{1}\bar{2}]$, CT3: $(\bar{1}101)[\bar{1}10\bar{2}]$, CT5: $(0\bar{1}11)[0\bar{1}1\bar{2}]$ and CT6: $(1\bar{1}01)[1\bar{1}0\bar{2}]$ the stress is 847.8 MPa. The yield stress is marked in red in the table and it is 90.06 MPa. When the tensile stress is applied along [0001] direction, it is interesting to see that the yield stress is only 4 MPa and all of the tensile twin variants can be activated simultaneously. However, compression twinning is absent.

Table 6.2 (a) The tensile stresses (MPa) needed to activate the 24 deformation variants along [$2\bar{1}\bar{1}0$]

Deformation modes	Deformation variants					
Basal sip	B1:Infinitive		B2: Infinitive		B3: Infinitive	
Prismatic slip	P1:Infinitive		P2:**90.06**		P3:**90.06**	
2nd pyramidal slip <c+a>	PY1: 98.5	PY2: 394.2	PY3: 394.2	PY4: 98.5	PY5: 394.2	PY6: 394.2
Tensile twin	TT1: Absent	TT2: Absent	TT3: Absent	TT4: Absent	TT5: Absent	TT6: Absent
Compression twin	CT1:282.6	CT2: Infinitive	CT3: 282.6	CT4: 282.6	CT5: Infinitive	CT6: 282.6

Table 6.2 (b) The tensile stresses (MPa) need to activate the 24 deformation variantsalong [$10\bar{1}0$]

Deformation modes	Deformation variants					
Basal sip	B1:Infinitive		B2: Infinitive		B3: Infinitive	
Prismatic slip	P1:**90.06**		P2:Infinitive		P3:**90.06**	
2nd pyramidal slip<c+a>	PY1: 131.4	PY2: 131.4	PY3: Infinitive	PY4: 131.4	PY5: 131.4	PY6: Infinitive
Tensile twin	TT1: Absent	TT2: Absent	TT3: Absent	TT4: Absent	TT5: Absent	TT6: Absent
Compression twin	CT1: 211.9	CT2: 847.8	CT3: 847.8	CT4: 211.9	CT5: 847.8	CT6: 847.8

Table 6.2 (c) The tensile stresses (MPa) need to activate the 24 deformation variants along [0001]

Deformation modes	Deformation variants					
Basal sip	B1:Infinitive		B2: Infinitive		B3: Infinitive	
Prismatic slip	P1:Infinitive		P2:Infinitive		P3:Infinitive	
2nd pyramidal slip <c+a>	PY1: 98.5	PY2: 98.5	PY3: 98.5	PY4: 98.5	PY5: 98.5	PY6: 98.5
Tensile twin	TT1:**4.0**	TT2: 4.**0**	TT3: **4.0**	TT4: **4.0**	TT5: **4.0**	TT6: **4.0**
Compression twin	CT1: Absent	CT2: Absent	CT3: Absent	CT4: Absent	CT5: Absent	CT6: Absent

Compression yield stress:

As a comparison with Fig. 6.4, the compressive yield stress of single crystal Mg, when it is subjected to the compression along the [$2\bar{1}\bar{1}0$], [$10\bar{1}0$]and[0001] directions, is examined (see Fig. 6.5). When compression acts along the c axis, the yield stress is 98.5 MPa, which is caused by the activation of the 2nd pyramidal slip system, while the activation stress for compression

twin is 211.9 MPa, indicating that compression twins do not occur. When single crystal Magnesium experiences compression along $[2\bar{1}\bar{1}0]$, the calculated yield stress is 5.34 MPa, caused by tensile twinning. Compared with the tensile case along the same direction of $[2\bar{1}\bar{1}0]$, the compression yield stress is much lower almost 1/22 of that for the extension case. In terms of compression along $[10\bar{1}0]$, the yield stress is 4 MPa, also caused by tensile twinning.

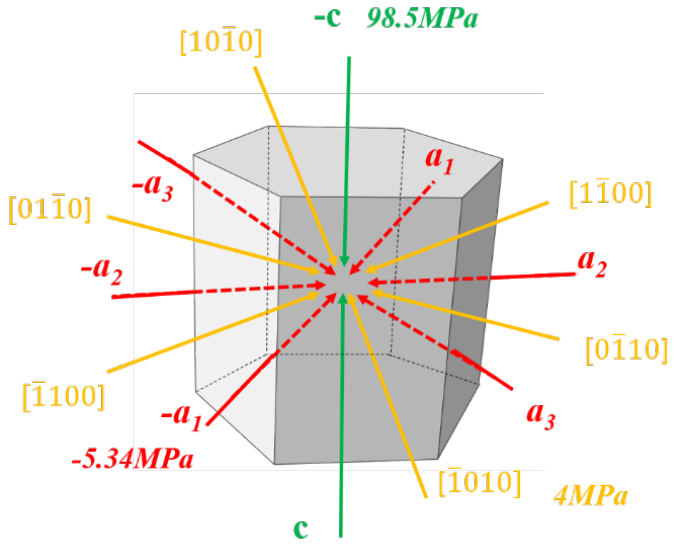

Fig. 6.5. The compression yield stresses of single crystal Magnesium along these three directions ($[2\bar{1}\bar{1}0]$,$[10\bar{1}0]$and[0001]).

Summarizing the simulation results for tension and compression, it is obvious that single crystal Mg exhibits strong anisotropy, which not only depends on the orientation of the single crystal but also on the applied tress state. Even at applied stresses along the same direction, tension stress is much different form the compression yield stress. The reason for this significant difference is that deformation twins play a very important role in single crystals, whose shear is mono-directional (polarity). Besides, the CRSS of different deformation modes is very different.

Keeping the Euler angles Ψ and Φ equal to zero, and changing θ from 5° to 85°, the axial stresses (tensile or compression stress) required to activate the basal slip mode, prismatic slip mode, 2nd pyramidal slip mode, tensile twinning and compression twinning are displayed in Fig. 6.6. In Fig. 6.6 (a), the activation stress for $\mathbf{a}_1(0001)[2\bar{1}\bar{1}0]$, variant of basal slip exhibits a "U" shape as the orientation changes, where θ alters from 5° to 85° with Ψ and φ being 0. Because of the symmetry of lattice, $\mathbf{a}_2(0001)[\bar{1}2\bar{1}0]$, and $\mathbf{a}_3(0001)[\bar{1}\bar{1}20]$ variants have the same activation stress under all these different orientations. For all of the basal slip system variants,

orientations with Euler angle (Ψ=0°, θ=45°, φ=0°) correspond to the lowest activation, where the Schmid factor is 0.5. In terms of prismatic slip, the activation stress of the $\mathbf{a}_1(0001)[2\bar{1}\bar{1}0]$ variant is calculated to be infinitive. Apparently, this result is reasonable, because in all orientations involved in Fig. 6.6, the applied stress axis is parallel with the slip plane. The curves of $\mathbf{a}_2$ (0001) $[\bar{1}2\bar{1}0]$ and $\mathbf{a}_3$ (0001) $[\bar{1}\bar{1}20]$ coincide with each other, showing monotonous decrease.

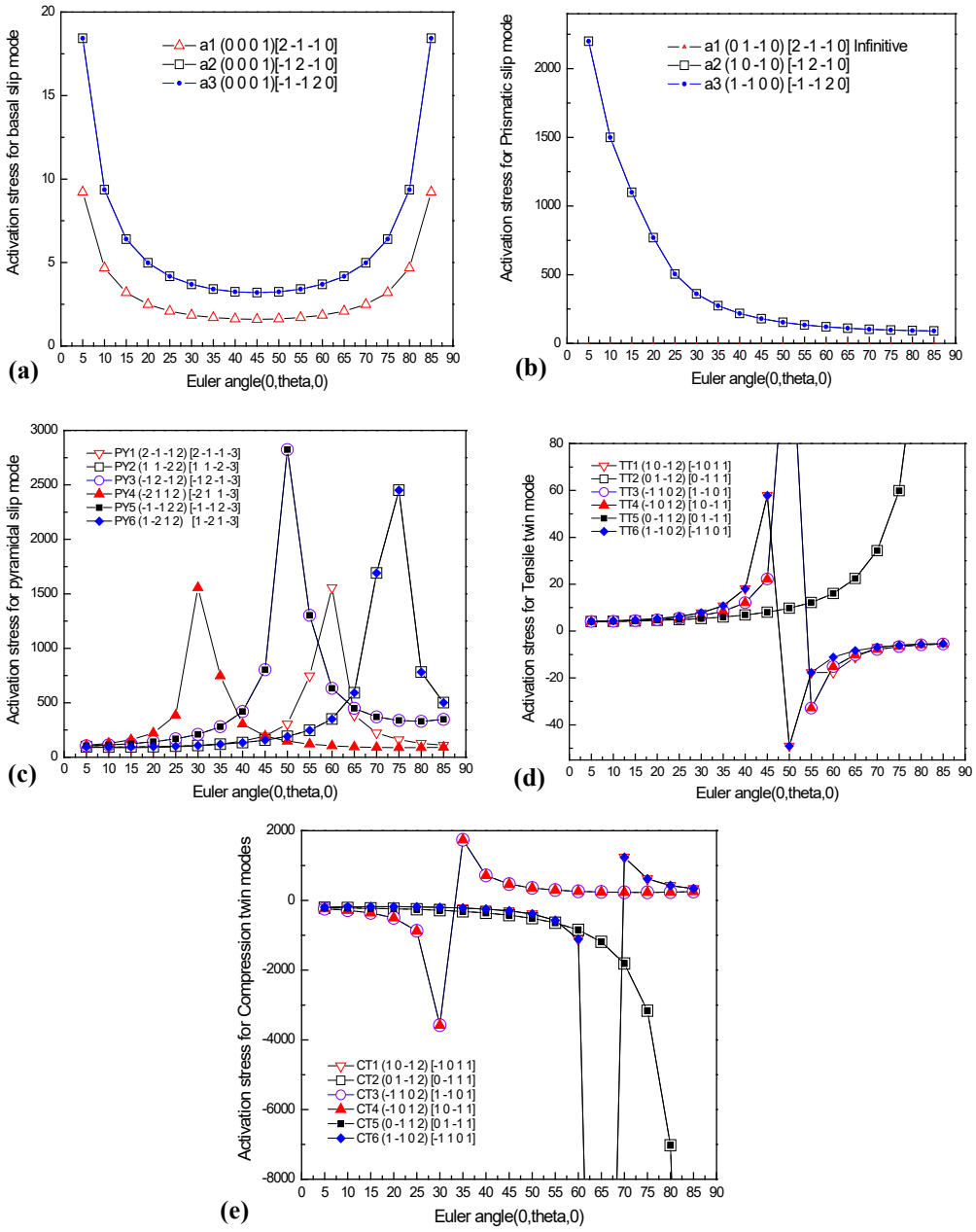

Fig. 6.6. The applied axial stress required to activate the 6 different deformation modes: (a) basal slip; (b) prismatic slip; (c) pyramidal slip; (d) tensile twinning; (e) compression twinning.

In fact, compared with basal slip systems, the prismatic slip (Fig. 6.6 (b)) requires much higher activation stress under the same orientation. For example, with the orientation (Ψ=0°, θ=5°, φ=0°), the activation stress for $\mathbf{a}_1(0001)[2\bar{1}\bar{1}0]$ variant of basal slip is 9.2 MPa, while the activation stress for $\mathbf{a}_2(10\bar{1}0)[\bar{1}2\bar{1}0]$ variant of prismatic slip is 11857 MPa, which is 1200 times higher than that for basal slip. Even the lowest activation stress in prismatic slip is 10 times as high as that of basal slip with Euler angle (Ψ=0°, θ=85°, φ=0°), indicating that the prismatic slip can be generally neglected relative to the basal slip.

As for pyramidal slip modes, the shape of curves of all prismatic slip variants exhibit a peak feature, although these peaks occur at different position in Fig. 6.6 (c), which corresponds to the different orientation. In Fig. 6.6 (c), the activation stress for the pyramidal slip variant PY1 $(2\bar{1}\bar{1}2)[2\bar{1}\bar{1}\bar{3}]$, has the highest value (1556.9 MPa) when the single crystal is orientated as (Ψ=0°, θ=60°, φ=0°). For symmetry reason, the variants PY2 $(11\bar{2}2)[11\bar{2}\bar{3}]$, and PY6 $(1\bar{2}12)[1\bar{2}1\bar{3}]$ have the same activation value in the whole span of the change of θ. Similarly, PY3 $(\bar{1}2\bar{1}2)[\bar{1}2\bar{1}\bar{3}]$, and PY5 $(\bar{1}\bar{1}22)[\bar{1}\bar{1}2\bar{3}]$ also shows coinciding curves. For the activation stress curves of PY3 and PY5, the Euler angle (Ψ=0°, θ=50°, φ=0°) corresponds to the occurrence of peak which is 5423.4 MPa. The curve of PY4 $(\bar{2}112)[\bar{2}11\bar{3}]$ is very similar to that of PY1 and the peak occurs at (Ψ=0°, θ=30°, φ=0°). Actually the curve of PY4 is symmetric to that of PY1 in relation to the (Ψ=0°, θ=45°, φ=0°). The required stress for activating tensile twins and compression twins is displayed in Fig. 6.6 (d) and Fig. 6.6 (e) respectively. Fig. 6.6 can directly deliver the information on the relative easiness of activation among these 5 different modes.

6.1.2 Reorientation of single crystal Mg

In this section, Eq. (3.14) is applied to simulate the reorientation of single crystal Mg. In order to represent the orientation evolution of single crystal Mg, simulation samples with three initial orientations are selected. For simplification, only basal slip is involved in these orientations. The *initial Euler angles* of orientation 1, 2 and 3 are (Ψ=0°, θ=15°, φ=0°), (Ψ=0°, θ=30°, φ=0°) and (Ψ=0°, θ=45°, φ=0°) respectively, assuring that there is only one active basal slip variant $\mathbf{a_1}(0001)[2\bar{1}\bar{1}0]$ during tensile testing. Fig. 6.7 illustrates the schematic representation of a single crystal Mg sample. In the three chosen initial orientations, the normal to the slip plane [0001], the slip direction $[2\bar{1}\bar{1}0]$ and tensile axis are coplanar vectors, which means that only θ evolves during tensile testing.

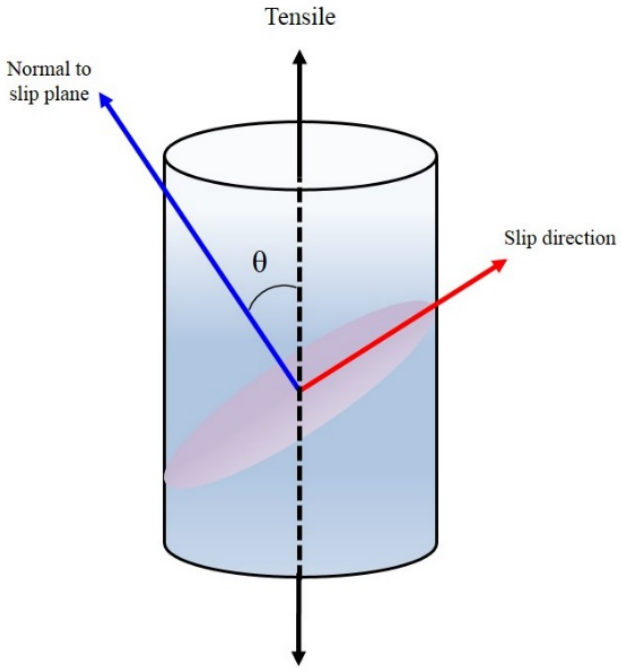

Fig. 6.7. Schematic representation of tension of a single crystal Mg sample.

Table 6.3 lists the evolution of θ angles with tensile strain for the three samples. The strain is set to 20% in order to observe a significant change of the θ angle. Here, only 10 sets of data are selected from the large number of calculation data. For the sample with initial orientation 1, after experiencing a tensile strain of 20%, the θ angle changes from 15° to 37.7°, which is an increase by 22.7°. The θ angle of the sample with an initial orientation 2 increases from 30° to 44.8°, by 14.7°. Similarly, the θ angle of the sample with an initial orientation 3 changes from 45° to 54.6°, by 9.6°. Fig. 6.8 shows the continuous change of θ angle with strain. From Fig. 6.8, even though the total strain is the same for all initial orientation samples, the change of θ is different. This directly shows that the overall texture evolution depends not only on strain, but also on initial texture.

Table 6.3 The evolution of θ angle with tensile strain

Strain	Orientation 1	Orientation 2	Orientation 3
	Evolution of θ		
0.01	16.99929	30.97336	45.56736
0.03	20.38667	32.81489	46.66943
0.05	23.2494	34.53484	47.73059
0.07	25.76338	36.15079	48.75367
0.09	28.02295	37.67633	49.74117
0.11	30.08577	39.12221	50.69532
0.13	31.99015	40.49717	51.61811
0.15	33.76315	41.80837	52.51134
0.17	35.42471	43.06181	53.37663
0.19	36.99006	44.26257	54.21546
0.2	37.74049	44.84457	54.62537

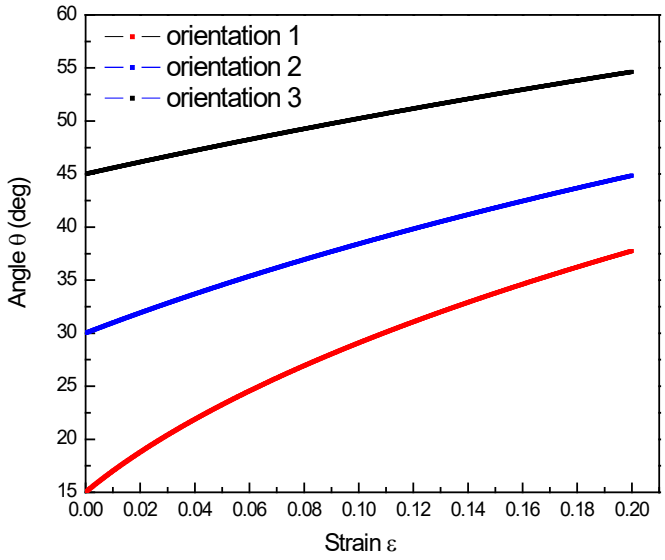

Fig. 6.8. The evolution of θ angle with tensile strain.

When the slip direction normal to the slip plane and the tensile axis are not coplanar, then, during the deformation, not only θ evolves, but also Ψ and φ evolve. In order to illustrate the change of Ψ and φ with strain, another set of three samples with different initial orientation are chosen, whose initial Euler angles are (Ψ=0°, θ=15°, φ=5°), (Ψ=0°, θ=15°, φ=15°) and (Ψ=0°, θ=15°, φ=25°). Table 6.4 lists the evolution of orientation of a Mg single crystal with three different initial orientations. Fig. 6.9 shows the evolution of orientations of a Mg single crystal with initial orientation (Ψ=0°, θ=45°, φ=150°).

Table 6.4 The evolution of orientation angle with tensile strain

strain	(Ψ=0°, θ=15°, φ=5°)			(Ψ=0°, θ=15°, φ=15°)			(Ψ=0°, θ=15°, φ=25°)		
	Ψ	θ	φ	Ψ	θ	φ	Ψ	θ	φ
0.01	-0.59	16.99	4.38	-1.81	16.99	13.11	-2.46	17.00	17.44
0.02	-1.01	18.77	3.93	-3.09	18.77	11.77	-4.18	18.78	15.64
0.03	-1.33	20.38	3.60	-4.04	20.38	10.76	-5.46	20.39	14.28
0.04	-1.58	21.86	3.33	-4.80	21.86	9.94	-6.47	21.87	13.20
0.05	-1.78	23.24	3.11	-5.41	23.24	9.29	-7.28	23.25	12.32
0.06	-1.95	24.54	2.93	-5.91	24.54	8.74	-7.96	24.54	11.58
0.07	-2.09	25.76	2.77	-6.34	25.76	8.26	-8.53	25.76	10.95
0.08	-2.21	26.92	2.63	-6.71	26.92	7.85	-9.02	26.92	10.40
0.09	-2.32	28.02	2.51	-7.03	28.02	7.49	-9.45	28.02	9.92
0.1	-2.42	29.07	2.40	-7.31	29.07	7.16	-9.82	29.08	9.49
0.11	-2.50	30.08	2.31	-7.57	30.08	6.88	-10.16	30.09	9.10
0.12	-2.58	31.05	2.22	-7.79	31.05	6.61	-10.46	31.06	8.75
0.13	-2.64	31.99	2.14	-8.00	31.99	6.37	-10.73	31.99	8.44
0.14	-2.71	32.89	2.06	-8.18	32.89	6.16	-10.97	32.89	8.15
0.15	-2.76	33.76	2.00	-8.35	33.76	5.95	-11.20	33.76	7.88
0.16	-2.81	34.60	1.93	-8.50	34.60	5.77	-11.40	34.61	7.63
0.17	-2.86	35.42	1.88	-8.6	35.42	5.60	-11.59	35.42	7.40
0.18	-2.91	36.21	1.82	-8.78	36.21	5.43	-11.76	36.22	7.19
0.19	-2.95	36.99	1.77	-8.90	36.99	5.28	-11.92	36.99	6.99
0.2	-2.98	37.74	1.72	-9.01	37.74	5.14	-12.07	37.74	6.80

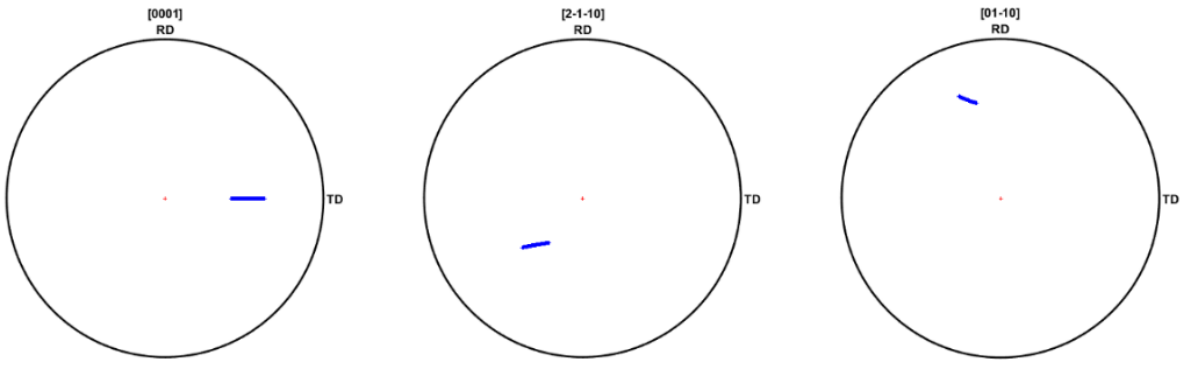

Fig. 6.9. Rotation of single crystal Mg with initial orientation (Ψ=0°, θ=45°, φ=150°).

Obviously two slip systems are simultaneously activated in this case, which means that only θ evolves, as can be seen in Fig. 6.9. From the present test calculations, it can be concluded that the present code for basal slip in Mg yields reasonable results.

Fig. 6.10 illustrates the reorientation effects caused by tensile twin variant T1 in single crystal Mg with different initial orientations (T1 tensile twin variant is schematically represented in Fig. 6.1 on page 70). When we only consider the T1 twin variant, there exists an orientation relation between T1 and matrix (see Table 3.3). By simple geometry calculation (based on Eq. (3.50)), we can conclude that the tensile twin rotates the parent grain (matrix)

around the zone axis $\langle 2\bar{1}\bar{1}0\rangle$ by about 86°. Since the initial orientation of the single crystal is different, the twins have different orientation. Since the hcp crystal has six-fold symmetry, there will be some equivalence between different twin variants with some particular initial orientations.

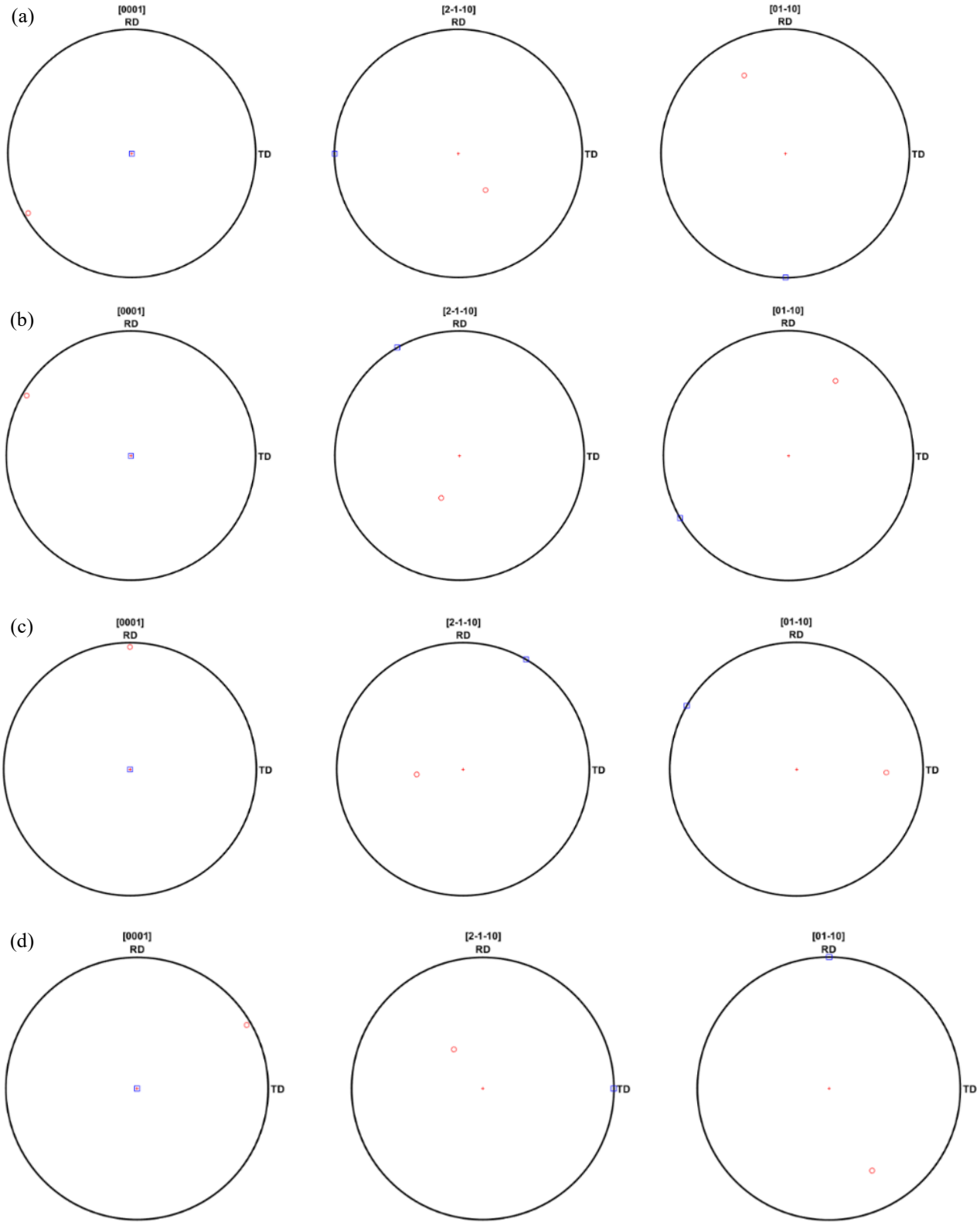

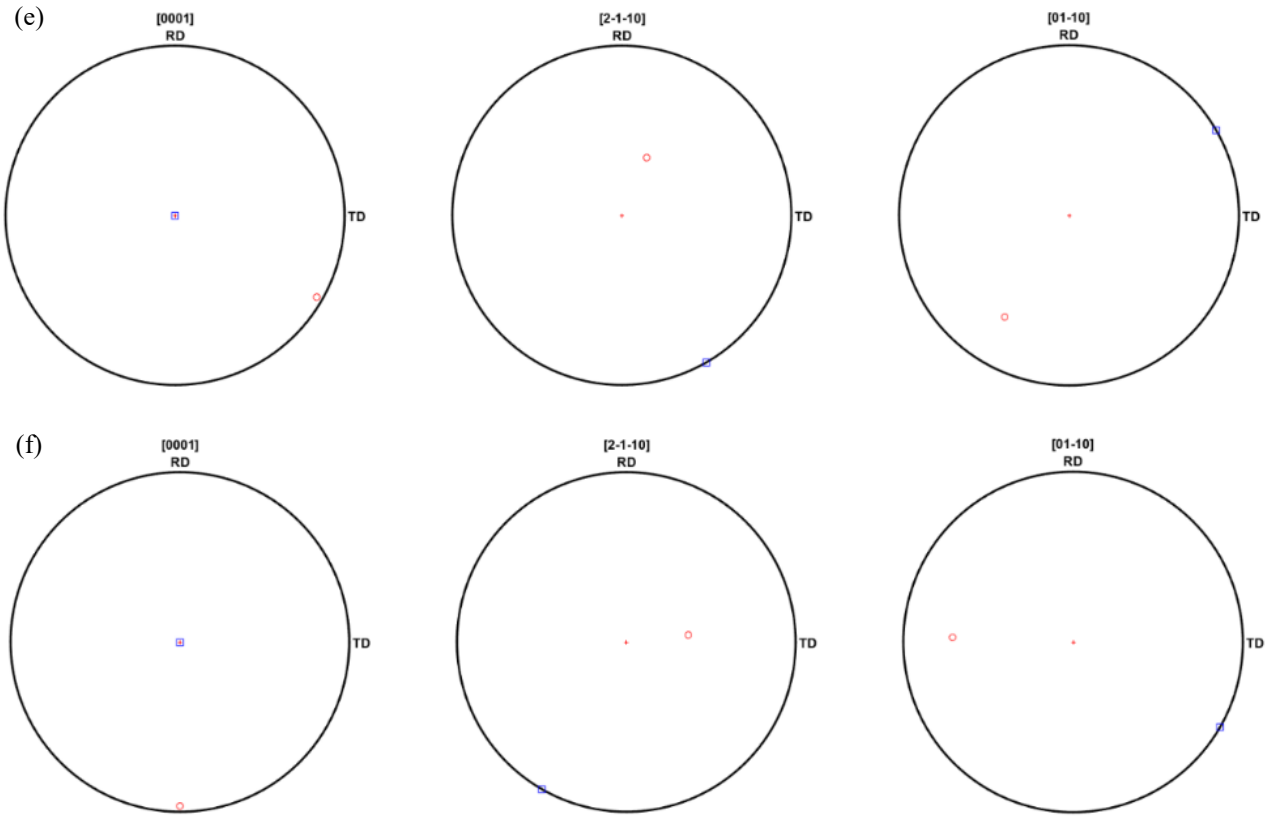

Fig. 6.10. Reorientation of single crystal Mg caused by tensile twin variant T1:The initial orientations of single crystal are (Ψ=0°, θ=0°, φ=0°), (Ψ=0°, θ=0°, φ=60°), (Ψ=0°, θ=0°, φ=120°), (Ψ=0°, θ=0°, φ=180°), (Ψ=0°, θ=0°, φ=240°) and (Ψ=0°, θ=0°, φ=300°).

Fig. 6.11 shows the reorientation effects caused by tensile twin variants T1, T2, T3, T4, T5 and T6 in single crystal Mg with the same initial orientation (Ψ=0°, θ=0°, φ=60°).

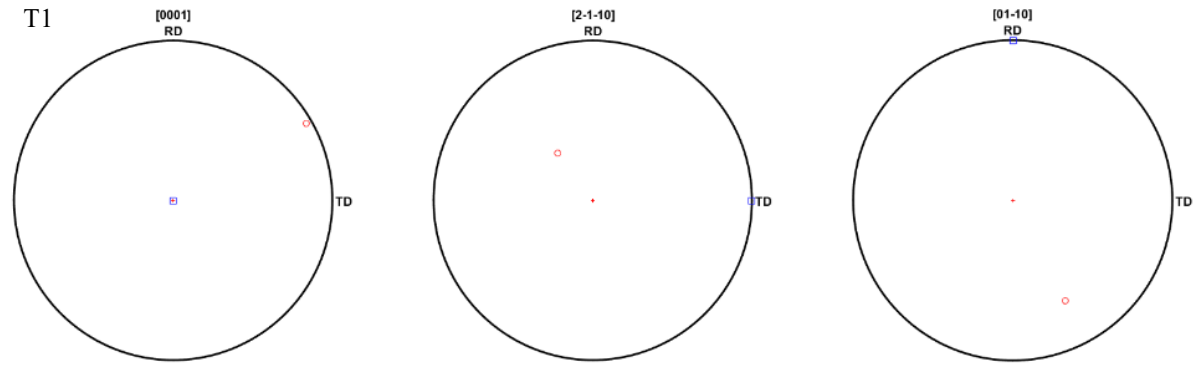

T2

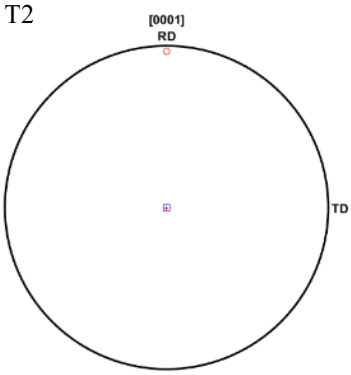
[0001]
RD
TD

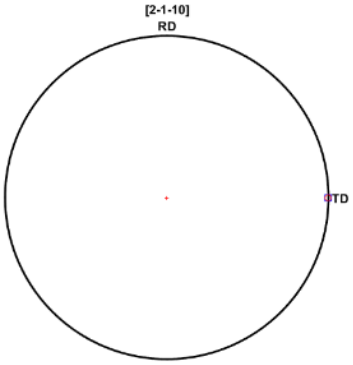
[2-1-10]
RD
TD

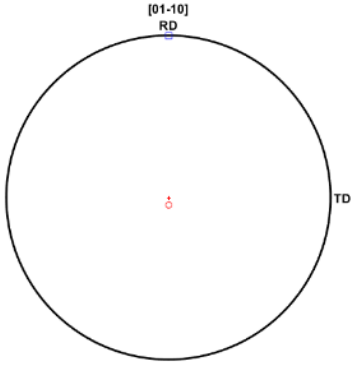
[01-10]
RD
TD

T3

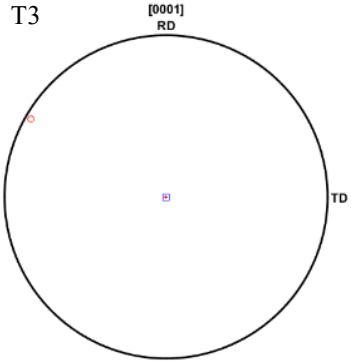
[0001]
RD
TD

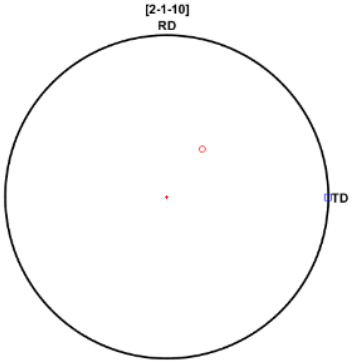
[2-1-10]
RD
TD

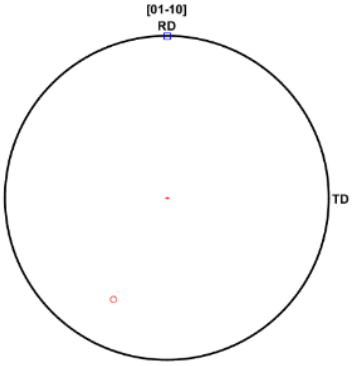
[01-10]
RD
TD

T4

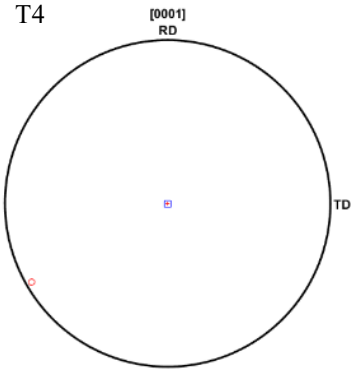
[0001]
RD
TD

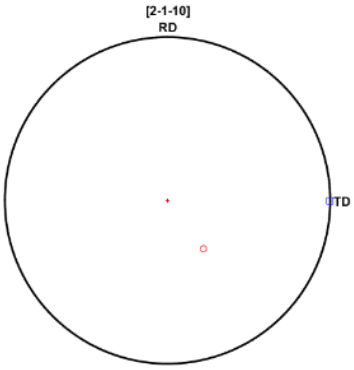
[2-1-10]
RD
TD

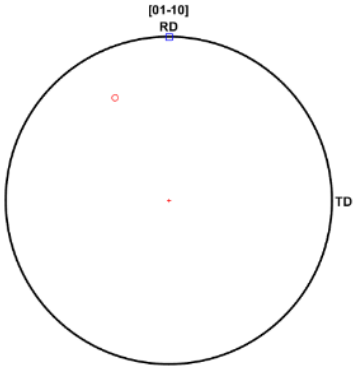
[01-10]
RD
TD

T5

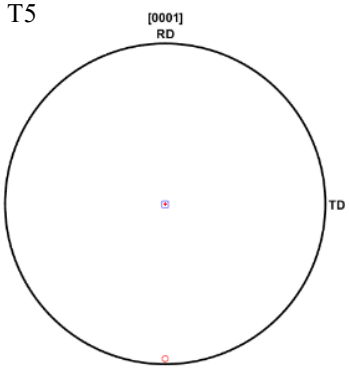
[0001]
RD
TD

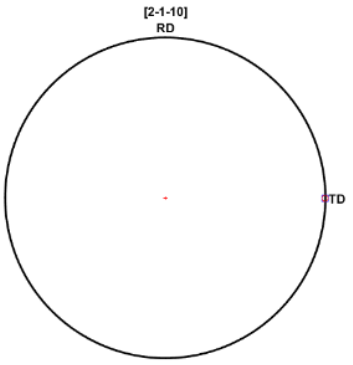
[2-1-10]
RD
TD

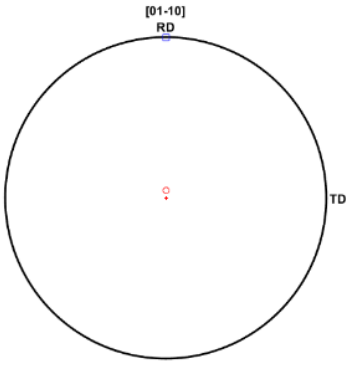
[01-10]
RD
TD

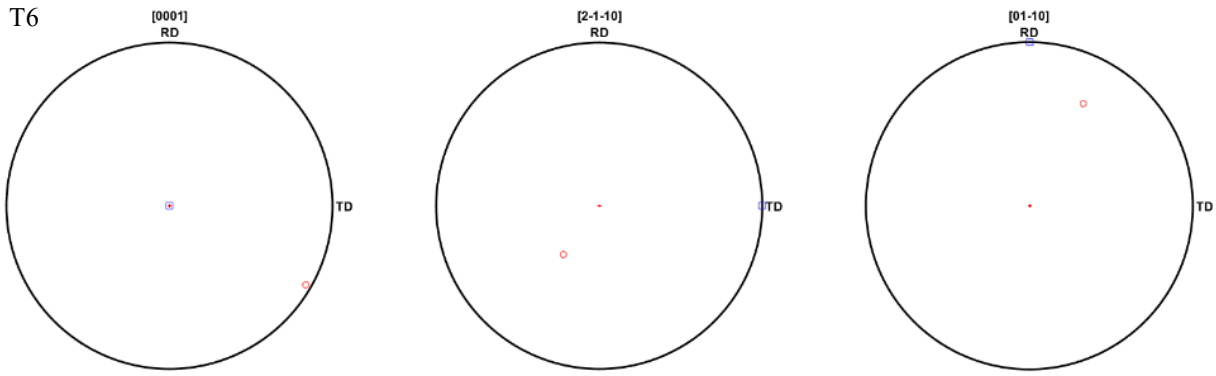

Fig. 6.11. Reorientation of single crystal Mg with same initial orientations (Ψ=0°, θ=0°, φ=180°) caused by different tensile twin variants: T1, T2, T3, T4, T5 and T6.

It can be seen from Fig. 6.11 that, after twinning, the angle distance between the *c* axis of tensile twin and that of the parent grain is about 86°. However, the tensile twin variants rotate around different zone axes. T1 and T4 twin variants share the same zone axis $[\bar{1}2\bar{1}0]$, but rotate around opposite direction by 86°, indicating that the corresponding crystal coordinate axis of T1 twin should be almost in the inverse direction of that of T4 twins. Similarly, there are still other tensile twin variants sharing the same zone axis. For example, the T2 and T5 twins share zone axis $[2\bar{1}\bar{1}0]$ and T3 and T6 twins share zone axis $[\bar{1}\bar{1}20]$. In Fig. 6.10 (b) and (e), after twinning caused by T2 and T5 tensile twin variants, the $[2\bar{1}\bar{1}0]$ axis of twins and the parent crystal coincide with one another. Therefore, when this code is applied to a polycrystalline case, we can estimate the frequency of the T2 and T5 twin activation by simply checking how many $[2\bar{1}\bar{1}0]$ axes of twins and the parent crystal coincide with each other. It should be noticed that, here, we do not consider the crystal symmetry. When considering crystal symmetry, there must be one specific $\langle 2\bar{1}\bar{1}0\rangle$ direction of twins, which is aligned with one $\langle 2\bar{1}\bar{1}0\rangle$ direction of the parent crystal. Therefore, the best way to determine, whether tensile twin is activated, is just to check the c axis orientation but not the $[2\bar{1}\bar{1}0]$ axis. Nevertheless, examining the reorientation is still useful for validating the code.

Now, we consider simultaneously T1, T2, T3, T4, T5 and T6 tensile twin variants. For different orientation of the single crystal, different tensile twin variants are active, which is shown in Fig. 6.12.

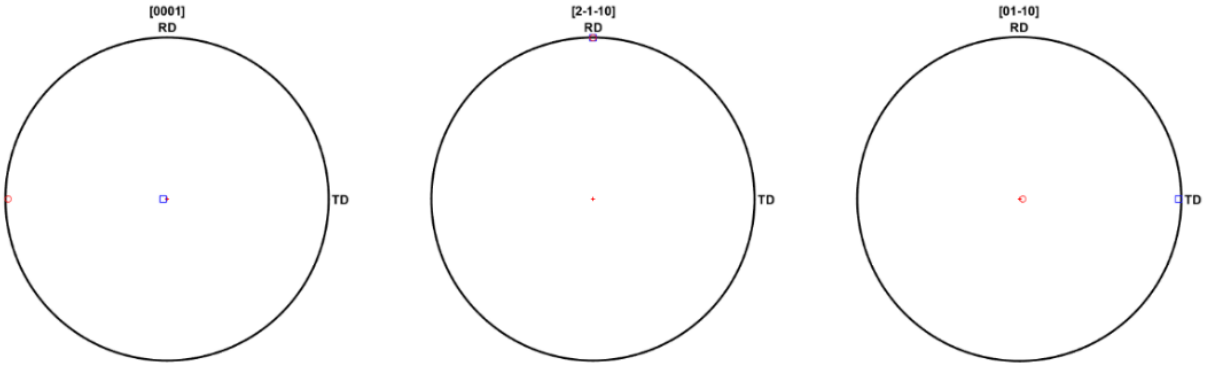

(Ψ=180°, θ=2°, φ=270°) T2, m=0.5

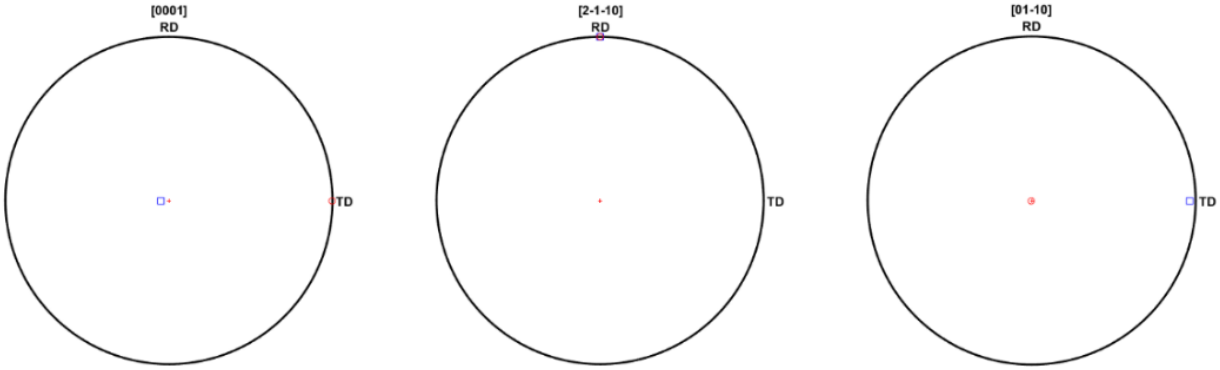

(Ψ=180°, θ=4°, φ=270°) T2, m=0.4986

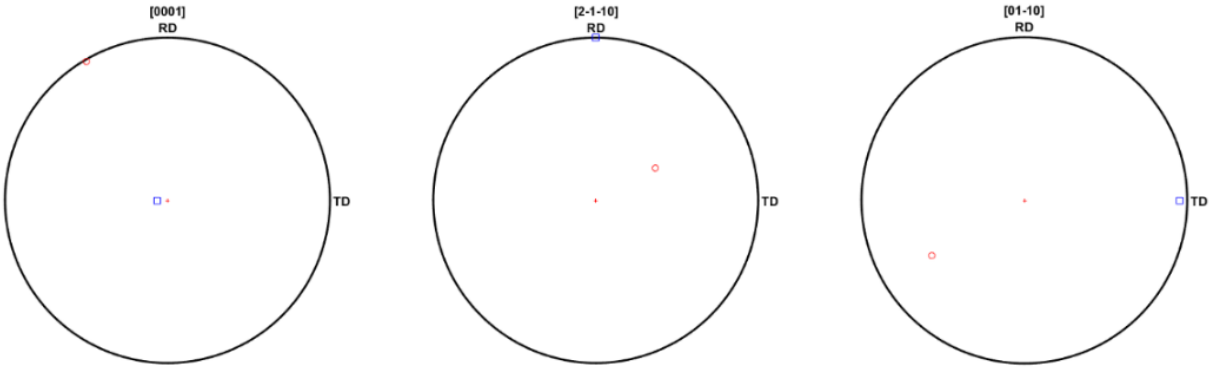

(Ψ=180°, θ=5°, φ=270°) T1, m=0.4970

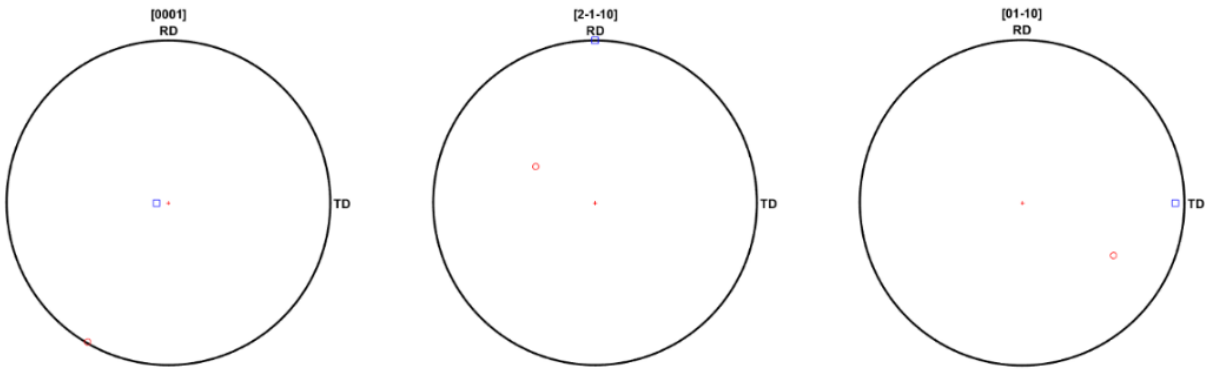

(Ψ=180°, θ=6°, φ=270°) T3, m=0.4955

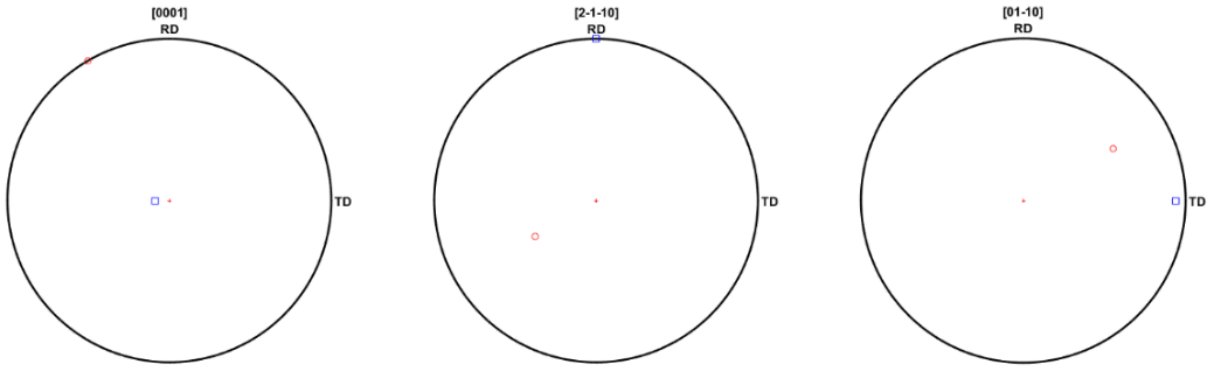

(Ψ=180°, θ=7°, φ=270°) T1, m=0.4936

Fig. 6.12. Reorientation of tensile twin variants in single crystal Mg with initial orientations.

It can be concluded form Fig. 6.12 that the tensile twin variant selection is very sensitive to the initial orientation. Even with a slight tilt of the c axis, the twin variant is different. This also explains that there is no twin-twin joints in S1, S2 and S3 in Section 5.2.

6.2 Texture simulation of Mg polycrystal based on iso-work principle

6.2.1 Iso-work principle

The iso-work increment assumption has been proposed by Bouaziz [111]. For a disordered microstructure, the mechanical work increment is assumed to be equal in each constituent as expressed by:

$$\sigma^{(I)} \cdot d\varepsilon^{(I)} = \sigma^{(J)} \cdot d\varepsilon^{(J)} \quad . \tag{6.5}$$

The iso-work principle has been applied to dual-phase steel, which consists of one soft phase and one hard phase. The modeling results for Fe-Ag 18% composite are also reasonable[111]. The assumption of iso-work principle is that the hard phase experiences small strain increments, while the soft phase would experience larger ones.

Since the iso-work principle yields good results in mechanically heterogeneous systems, it seems likely to be applicable to the case of polycrystalline deformation, too. We need to keep in mind, however, that, in the original application, both hard and soft phases underwent deformation, whereas in the case of deformation of polycrystals, some grains might not experience deformation but only pure rigid rotation. If this happens, no mechanical work will be done and the iso-work principle will be inapplicable to these particular grains. However, viewing deformation of polycrystal as statistical feature, the iso-work principle "acts" within the statistical average of all grains (1 cm^3 of polycrystal metal contains almost 10^9 grains,

supposing the grain size is 1000 μm^3), so that the effect of a few undeformed grains on the overall mechanical properties should be negligible. Furthermore, when deformation proceeds, the mechanical work can be assumed to be equal in every grain, no matter of its orientation. For hard orientated grains, the stress in the grain is big, while the strain increment in the grain is small. By contrast, for soft oriented grains, the stress is small, while the strain increment in the grain is big.

In this section, we combine crystal plasticity in the single crystal introduced in Section 6.1 with the iso-work principle. First, we assume that the stress state is the same in every grain and the reference strain rate of each grain is equal to the macro strain rate of the polycrystalline aggregate. Then we get the initial stress of each grain based on Schmid law and the volume average of the microstress in each grain is equal to the macrostress of the polycrystalline aggregate. This reference strain rate is used to calculate the work rate done in each grain. Since the microstrain rate in each grain is, in general, not the same as the macrostrain rate, the realistic microstrain rate in each grain has to be recalculated by applying the iso-work principle. The mean value of the work done by each grain can be calculated(details see the Fig. 6.13 and its interpretations). Based on iso-work assumption, the microstrain increment in each grain is calculated. and the macrostrain increment of the polycrystal aggregate will be the volume average of the microstrain increments in each grain. The basic idea and flow chart of calculation steps is illustrated in Fig. 6.13,

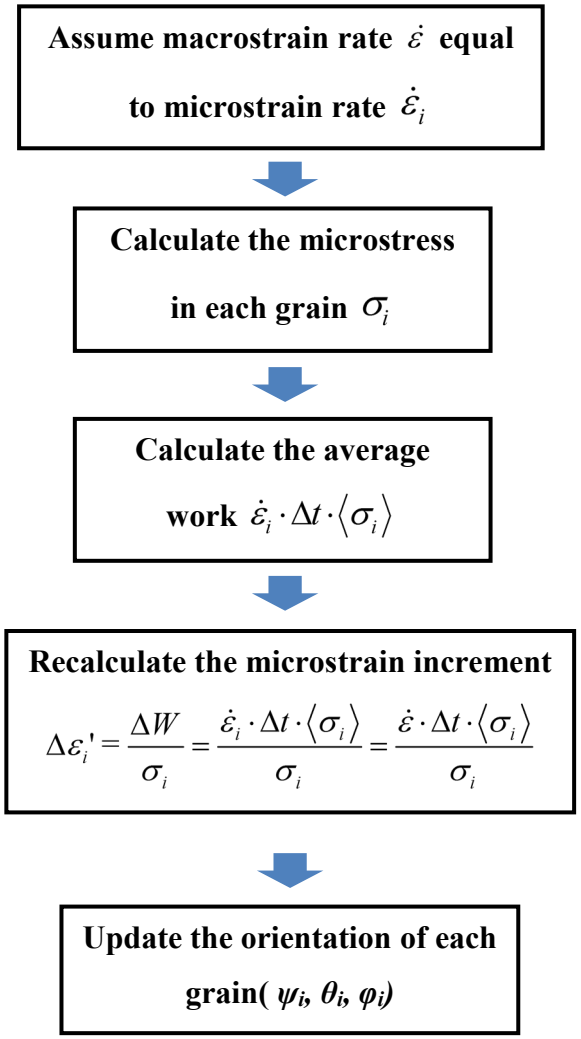

Fig. 6.13. Flow chart of the algorithm of iso-work mean field method.

The detailed algorithm based on the flow chart in Fig. 6.13 can be explained in the following steps. These steps happen in the time interval Δt between t_n moment and t_{n+1} moment.

Step 1: calculate the yield strength in each grain σ_i : We assume that the reference microstrain rate $\dot{\varepsilon}_i$ is the same as the macrostrain rate $\dot{\varepsilon}$ and the stress state is the same in every grain. Based on this assumption and Schmid's law, the yield strength, σ_i , in each grain can be calculated.

Step 2: Calculate *the mean work* ΔW in the time interval Δt : The work in each grain is equal to $\sigma_i \cdot \dot{\varepsilon}_i \cdot \Delta t$. By assuming that each grain has the same volume, the volume mean is

transformed to equal the arithmetic mean. Therefore, the mean work can be calculated by using following equation, where N is the number of grains

$$\Delta W = \frac{\sum_{i}^{N} \sigma_i \cdot \dot{\varepsilon}_i \cdot \Delta t}{N} = \dot{\varepsilon}_i \cdot \Delta t \cdot \langle \sigma_i \rangle = \dot{\varepsilon} \cdot \Delta t \cdot \langle \sigma_i \rangle$$

Step 3: recalculate the micro-strain increment $\Delta\varepsilon_i'$ of each grain corresponding to *the mean work*

$$\Delta\varepsilon_i' = \frac{\Delta W}{\sigma_i} = \frac{\dot{\varepsilon}_i \cdot \Delta t \cdot \langle \sigma_i \rangle}{\sigma_i} = \frac{\dot{\varepsilon} \cdot \Delta t \cdot \langle \sigma_i \rangle}{\sigma_i}$$

Step 4: calculate the *statistical mean value* (macrostrain increment) of micro-strain increment in each grain

$$\Delta\varepsilon = \frac{\sum_{i}^{N} \Delta\varepsilon_i'}{N} = \langle \Delta\varepsilon_i' \rangle = \left\langle \frac{\dot{\varepsilon} \cdot \Delta t \cdot \langle \sigma_i \rangle}{\sigma_i} \right\rangle = \dot{\varepsilon} \cdot \Delta t \cdot \langle \sigma_i \rangle \cdot \left\langle \frac{1}{\sigma_i} \right\rangle = \dot{\varepsilon} \cdot \Delta t \cdot \alpha$$

Normally $1/\langle \sigma_i \rangle$ is not the same as $\langle 1/\sigma_i \rangle$, therefore $\Delta\varepsilon \neq \dot{\varepsilon} \cdot \Delta t$.

Step 5: update the orientation of each grain by applying Eq. (3.14)

6.2.2 Texture evolution of Mg without initial texture

The random texture is of high significance for the simulation of texture evolution of polycrystalline samples without initial texture. Fig. 6.14 (a) and (b) illustrate the representation of random texture of a polycrystalline sample consisting of 8000 grains by using the stereographic projection scheme and equal area map scheme, respectively. It should be kept in remind that the random texture does not mean the random distribution of the three Euler angles (Ψ, θ, φ), *but rather* the random distribution of (Ψ, cosθ, φ). This is just because of the non-homogeneity of orientation space. The random distribution of (Ψ, cosθ) assures the homogenous pole density on the spherical surface, and thus leads to a random orientation distribution together with the random distribution of φ. Fig. 6.14 indicates that the random texture is better represented by the equal area map scheme.

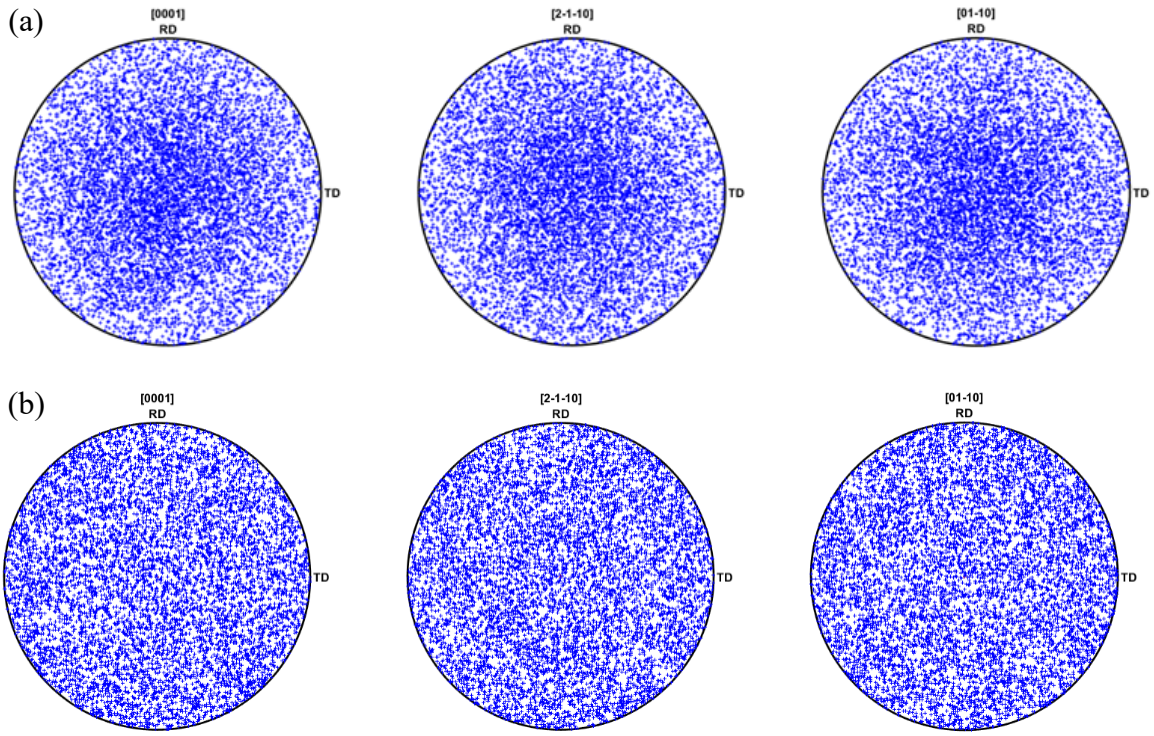

Fig. 6.14. Representation of random texture of polycrystalline sample consisting of 8000 grains: (a) stereographic projection scheme; (b) equal area map scheme.

Fig. 6.15 shows the texture evolution of a polycrystalline Mg sample consisting of 800 grains with random texture during tensile deformation. The entire *c* axis of grains after deformation deviates from the tensile axis, however, grains with hard orientation rotated much slower than those with soft orientation. As elongation goes on, the texture on the brim of the circle becomes sharper and the center of the circle becomes blank, which means that, after deformation, all of the grains tend to reorientation of their *c* axis perpendicular to the tensile axis.

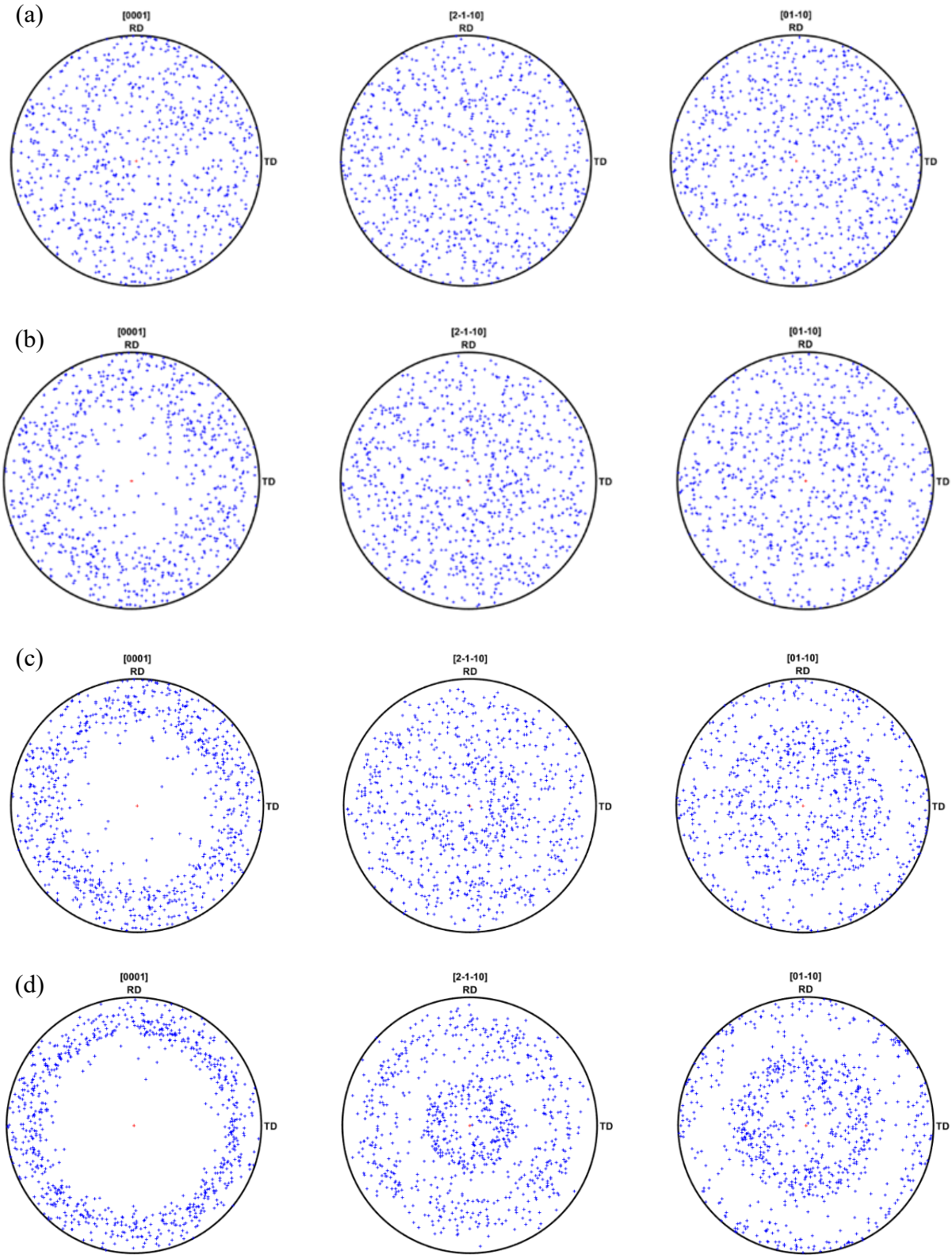
(a)
[0001]
RD
TD
[2-1-10]
RD
TD
[01-10]
RD
TD
(b)
[0001]
RD
TD
[2-1-10]
RD
TD
[01-10]
RD
TD
(c)
[0001]
RD
TD
[2-1-10]
RD
TD
[01-10]
RD
TD
(d)
[0001]
RD
TD
[2-1-10]
RD
TD
[01-10]
RD
TD

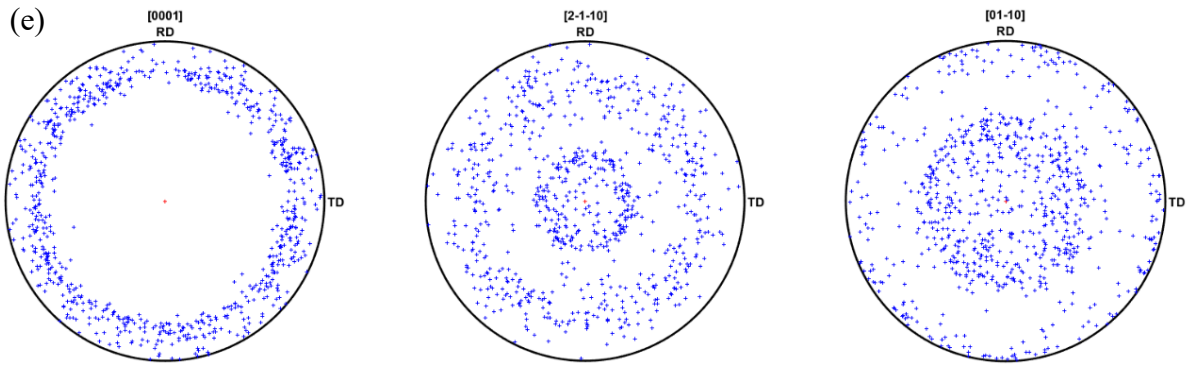

Fig. 6.15. Texture evolution (caused by basal slip) of a polycrystalline Mg sample consisting of 800 grains with random initial texture at room temperature and a strain rate of 0.001/s: (a) ε=0; (b) ε=0.3; (c) ε=0.6; (d) ε=1.0; (e) ε=2.0 (equal area map scheme).

It is interesting to find that the initially random orientation distribution of **a** $[2\bar{1}\bar{1}0]$ axis becomes separate after deformation. Note that, during tensile deformation, only basal slip is activated, with the *c* axis close to be perpendicular to the tensile axis and the basal plane almost parallel to the tensile axis. From the viewpoint of crystal symmetry, when the basal plane is parallel to the tensile axis, the possible range of angles between $[2\bar{1}\bar{1}0]$ axis and the tensile axis will be either approximately 60-90° or 0-15°.

In Fig 6.16, when we rotate the basal crystal plane around the *c* axis, which reaches out of the paper plane in Fig 6.16, the angle between **a** $[2\bar{1}\bar{1}0]$ axis, the closest packed direction and T direction(tensile axis), can be easily envisaged to lie inside of these two angle ranges. Thus, in the pole figure of ***a*** axis, the pole density shows two separate parts. One part is relatively concentrated in the center of the circle and the other part is near the brim of the circle. However, in terms of pole density of the ***b*** axis, *i.e.*, $[01\bar{1}0]$, different characteristics are exhibited. Although, after tensile deformation, the distribution of b axis is also bifurcate, the center part of distribution of the **b** axis is much larger than that of the **a** axis, while the brim part is minor. This can be explained on basis of crystal symmetry as well. The **b** $[01\bar{1}0]$ axis is not the closest packed direction of the hcp lattice. If we rotate the basal crystal plane around the c axis, most of the b directions will be located in the range of 0-60°, which is corresponding to the center part of the pole density of the $[01\bar{1}0]$ axis.

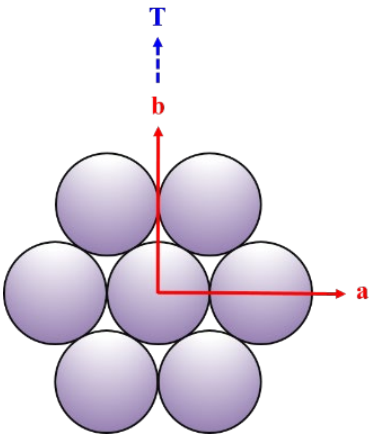

Fig. 6.16. Schematic representation of *a* axis and *b* axis of Mg.

In the preceding discussion, only basal slip is activated at room temperature and the effects of pyramidal slip on the texture evolution are not considered. Then, basal slip is responsible for the texture evolution depicted in Fig. 6.15. At temperatures above approx. 180 °C, pyramidal slip will start to play an important role during deformation. In order to simulate the effects of pyramidal slip on the texture evolution, we choose the 2nd pyramidal slip system and reset the relative value of CRSS for different slip modes so that only the 2nd pyramidal slip system can be activated during tensile deformation. We again start from the sample without initial texture and deform the sample to a strain of 200%.

The simulation results are illustrated in Fig. 6.17. As the tensile deformation proceeds, the pole figure of the *c* axis becomes more and more ring-shaped. The area of the ring does neither expand nor shrink, while it becomes sharper after the sample has experienced large strain. The evolution of *c* axis during tensile deformation is explained by the kinematics of the single crystal: As deformation proceeds, the 2nd pyramidal slip plane tends to be parallel to the tensile axis. When the 2nd pyramidal slip plane tends to be parallel to the tensile axis, the *c* axis will simultaneously be at an angle of about 70° to the tensile axis. However, there is a relatively sharp density of orientations located in the centre of the circle. This is probably caused by double-slip of the 2nd pyramidal slip. Strikingly, the density of *c* axis shrinks to a small area of points at the strain of 200%, causing all 2nd pyramidal slip systems to be active simultaneously. Rotations of these slip systems cancel with each other, resulting solely in an overall sample elongation with the *c* axis remaining unmoved in the pole figure.

From Fig. 6.17, it is obvious that there is no separation of pole density of **a** $[2\bar{1}\bar{1}0]$ axis and **b** $[01\bar{1}0]$ axis, while there are two parts in the pole density of [0001] c axis, and pole densities of both **a** $[2\bar{1}\bar{1}0]$ axis and **b** $[01\bar{1}0]$ axis tend to be closer to the brim of the circle as

strain increases. A blank region forms in the center of the circle in both cases, which expands with strain. This blank region in the $[2\bar{1}\bar{1}0]$ pole figure is considered to be caused by the rotation of the $[2\bar{1}\bar{1}0]$ axis round the $[01\bar{1}0]$ axis.

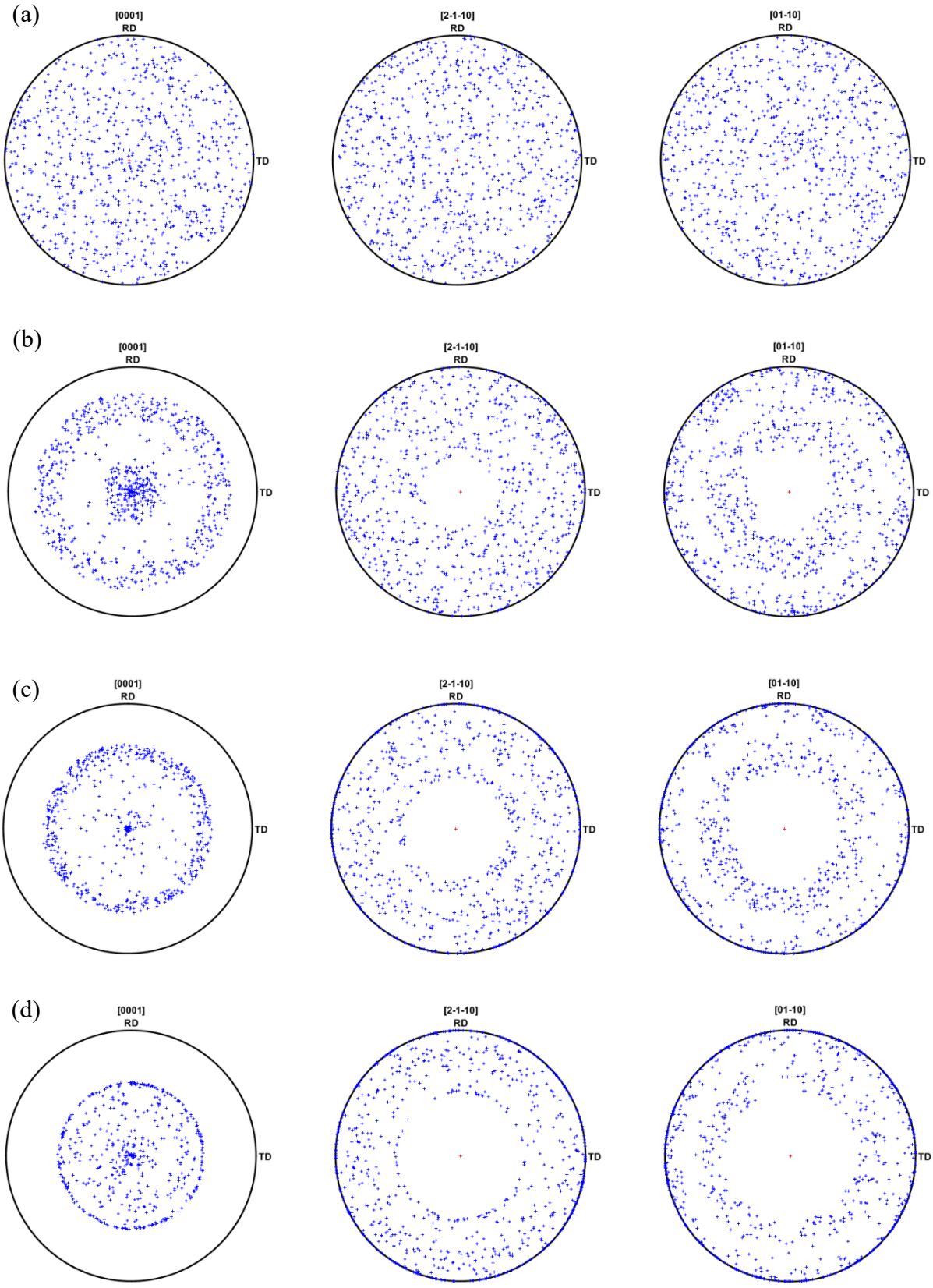

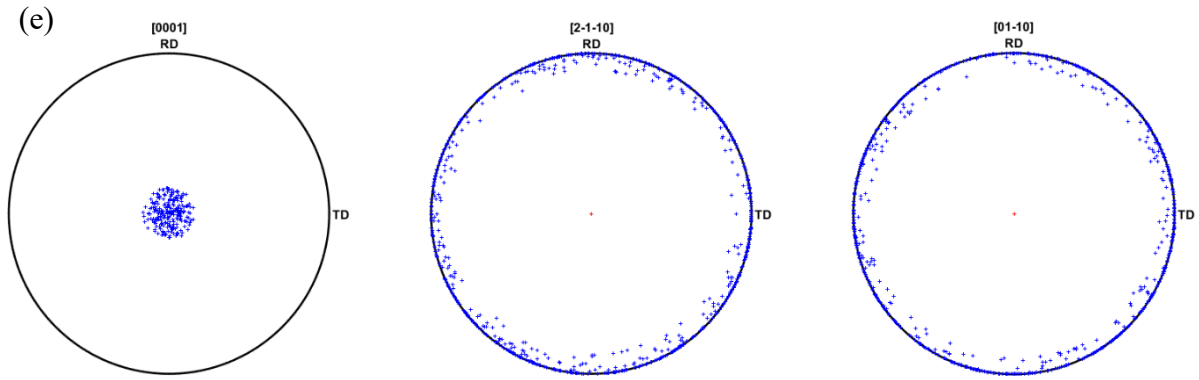

Fig. 6.17. Texture evolution caused by 2nd pyramidal slip of polycrystalline Mg sample consisting of 800 grains without initial texture at high temperature above 180 ℃and a strain rate 0.001/s: (a)ε=0; (b) ε=0.3; (c) ε=0.6; (d) ε=1.0; (e) ε=2.0 (equal area map scheme, only 2nd pyramidal slip is considered).

When the sample is deformed at elevated temperature, both basal slip and 2nd pyramidal slip are activated. We will thus examine the effects of the simultaneous activation of basal slip and 2nd pyramidal slip on the texture evolution in the following. The simulation results are shown in Fig. 6.18, which demonstrates the texture of sample with a tensile strain of about 60%. The *c* axis pole density in the pole figure can be considered as the simple superposition of texture components caused by basal slip and 2nd pyramidal slip. The center part of texture is corresponding to the texture component of pyramidal slip and the brim part corresponding to the component caused by basal slip. Actually, the pole figure of **a** $[2\bar{1}\bar{1}0]$ axis exhibits quite homogeneous feature and the pole figure of **b** $[01\bar{1}0]$ axis as well. Similarly, this feature can also be attributed to the superposition of the two texture components caused by basal slip and 2nd pyramidal slip.

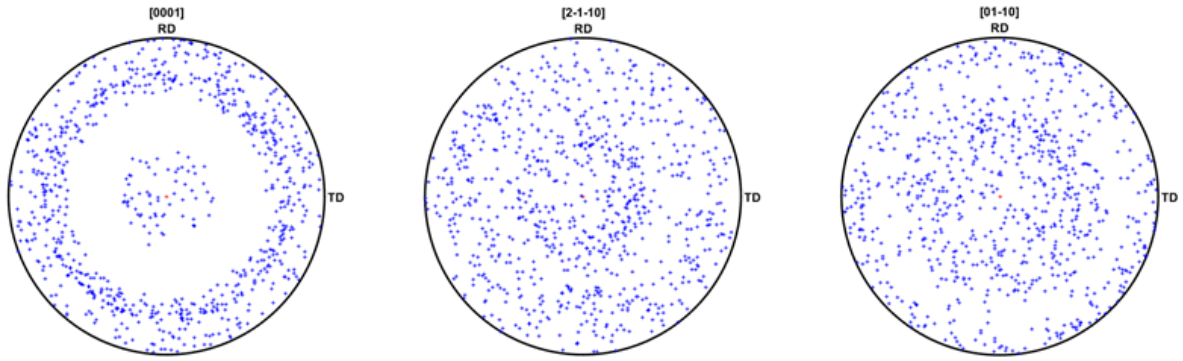

Fig. 6.18 both basal and pyramidal slip active ε=0.6.

The effects of tensile twins on the texture evolution are demonstrated in Fig. 6.19. The simulation sample is polycrystalline Mg with 1000 grains. The blue cross represents the parent crystal, while the red circle represents the twin. It can be seen that, after twinning, the *c* axis of the parent crystal is reoriented by about 86°. This explains the red ring-like pole density in the [0001] pole figure. Those grains, with initial orientation with the *c* axis lying almost parallel to the tensile axis, are favorable for tensile twinning. After twinning, the *c* axis will be almost perpendicular to the tensile axis. Since parent grains located in the center of the [0001] pole figure are favored for tensile twinning, a blank area is left after deformation (all grains twinned). The large size of blank area is due to twin polarity (see Chapter 3).

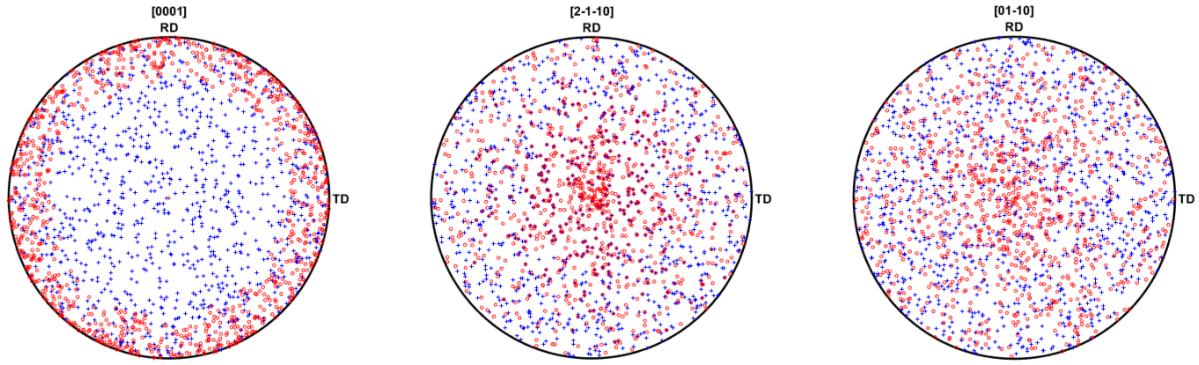

Fig. 6.19. Reorientation of tensile twins in polycrystalline Mg with 1000 grains (the blue cross represents the parent crystal, while the red circle represents the twin).

Current limitations of the model:

It should be noted that the code of twin reorientation used here clearly meets some limitations, since, the volume fraction evolution of twins is not considered. Furthermore, as a rough assumption, the twinned part of the parent grains is defined as a new grain. In spite of this tentativeness of the present code, obviously, some useful information on twin reorientation and tensile twin variants selection is obtained by the present simulations. The modification to this code will include the twin volume fraction evolution, which will be described in detail in Section 6.3.

An even more critical disadvantage in this model is that the stress state is assumed to be the same in each grain. Although the stress equilibrium condition across a grain boundary can be satisfied in this assumption, the compatibility condition is violated. Besides, owing to the simple stress state, the tensile twin selection is clearly over-simplified. In fact, the tensile twin selection is related to the local stress state in the grain scale and should thus take into account the stress state and effects of twin-twin interaction. Therefore, in the next section, a more realistic mean

field model is presented, which considers the evolution of twin volume fraction due to twin growth. The volume fraction evolution equation introduced in Section 4.6 is applied.

6.3 Simulation of texture of AZ31 Mg alloy by Taylor mean field model

6.3.1 Introduction of model and code package

The texture evolution of as-extruded AZ31 Mg alloy is simulated by the Taylor Type mean field model that includes the semi-physics based twin evolution equation afore mentioned in Section 4.5. Owing to its mean field feature, the calculation time is reduced to magnitude of order of minutes. A code package containing eight subroutines has been developed and used in this approach. Fig. 6.20 illustrates the structure of this code package.

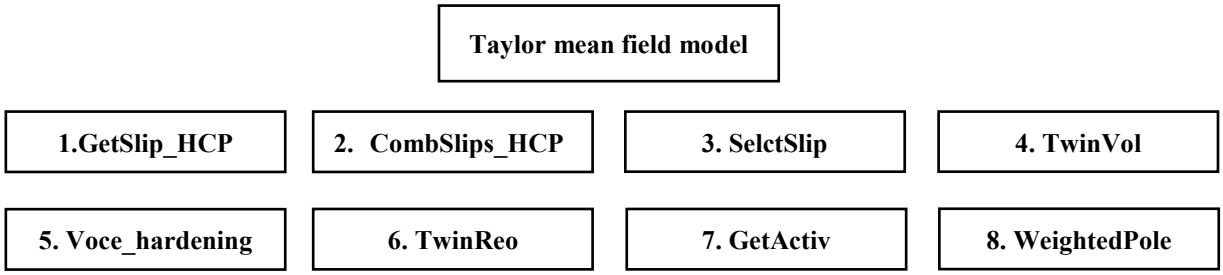

Fig. 6.20. The structure of the developed simulation code package.

1) **GetSlip_HCP:** This subroutine is used to calculate all potential slip systems and twin variants and to express them in the three axis coordinate frame. The transformation matrix $\boldsymbol{Q}$ and $\boldsymbol{S}$, introduced in Section 6.1 are utilized.
2) **CombSlips_HCP:** In the full constraints Taylor model, five independent slip systems are required. However, strong anisotropy of hcp may imply that this requirement cannot be satisfied. Thus, instead of FC model, a relaxed Taylor model has been selected to conduct the simulation. In this subroutine, all possible combinations of slip systems and twin modes are calculated. These slip systems are basal slip, prismatic slip and second order <c+a> pyramidal slip, while the twin modes only consist of the tensile twin mode. Since compression twins are very rarely observed experimentally, this simplification is reasonable and in line with available simulation studies of texture evolution.
3) **SelctSlip:** In Taylor-based models, the microstrain in each grain is assumed to be the same as the macrostrain tensor. The combination of different slip shear, which yields the prescribed strain, might be non-unique. In other words, there might be many different combinations of slip systems, which can meet the geometrical requirement that the slip shear must generate the macrostrain tensor. According to the maximum work principle and

the minimum shear principle proposed by Bishop and Hill [30], the virtual work done by the different slip systems and the twin shear should be the least. Therefore, in this subroutine, the work done by all possible combinations of slip are calculated, among which the combination doing the least work is chosen as the realistic slip systems in this specific step.

4) **TwinVol:** In this subroutine, the semi-physics law of twin growth introduced in Section 4.4 is applied. Changes of the twin volume fraction with strain are captured by this subroutine. For simplicity, the evolution of twin volume fraction is assumed to be the same in each grain. In other word Eq. (4.17) used in each grain has same value of f_0, f_s and α (see Section 4.4). Essentially, the twin volume used here, thus, represents the mean twin volume.
5) **Voce_hardening:** The Voce hardening law is used to describe the hardening behavior of each deformation mode (for details see Chapter 3). The self-hardening and the latent hardening factors are fitted and referred to the literature. Importantly, parameters of this subroutine govern the relative activities of different deformation modes during deformation, *i.e.*, the influence of the ratios among the initial CRSS of different deformation modes on the relative activities can be examined.
6) **TwinReo:** This subroutine numerically realizes the reorientation of tensile twin variants {10-11}<10-12> relative to the matrix. As discussed in Chapter 3 of this thesis, the tensile twin variant {10-11}<10-12> can reorient the matrix by about 86°. The rate of the reorientation caused by twin is thus directly determined by the rate of twin volume faction evolution.
7) **GetActiv:** This subroutine is used to calculate the relative activity among the afore mentioned deformation modes, basal slip, prismatic slip, second order <c+a> pyramidal slip and tensile twinning. The relative activity is based on the calculation of the proportion of the shear increment of each deformation mode on the total shear increment in each simulation step.
8) **WeightedPole:** This subroutine is used to calculate the weighted pole, because of the twin effects. For this, each grain is divided into 100 slices. Each slice represents a specific orientation and each slice is assumed to have the same weight. Therefore, by using this subroutine, materials with inhomogeneous grain size distribution can be simulated and the effects of twinning on the texture evolution can be discretized and shown in the smoothed pole figure.

6.3.2 Texture evolution with initial texture

The initial texture of the as-extruded AZ31 Mg alloy is shown in the Fig. 6.21 (a)-(c). Here the RD-ND plane is chosen as perpendicular to the extrusion axis. In order to simulated the texture evolution of this as-extruded alloy under the compression along the extrusion axis and to validate our model, a virtual material with 1000 equally sized grains and similar initial texture was chosen as the start for the simulation, as shown in the Fig. 6.21 (d)-(f). Obviously, our virtual material can represent the initial texture of real matrial quite well. The *c* axis of all 1000 crystals was set to be perpendicular to the compression axis and the <10$\bar{1}$1> axis was set to be parallel with the compression axis. As mentioned in Chapter 4, the material has strong texture which is unfavorable to basal slip but favourable for tensile twinning.

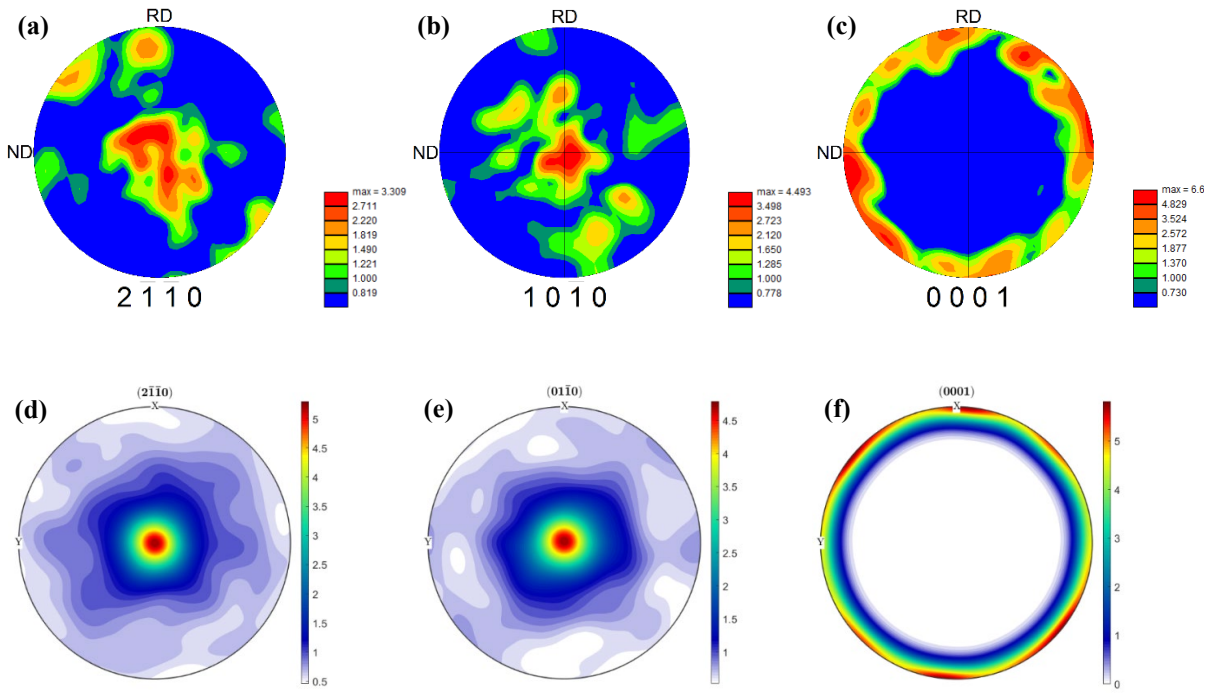

Fig. 6.21. Initial orientation of real AZ31 Mg alloy (a)-(c); and the initial orientation assigned to the virtual material in the simulation (d)-(f).

Fig. 6.22 illustrates the experimental results of AZ31 Mg alloy with different compression strains, being 0.15%, 2% and 6.6% respectively. As can be seen in this Figure, the texture has experienced a significant change. Comparing the Figs. 6.21 (c), (f) and (i), one can find that a new component of texture emerged, which is approximately aligned with the compression axis. This indicates that the new texture component is caused by tensile twins. Simultaneously, the ring (see Figs. 6.21 (c) and (f)) almost disappeared at the strain 6.5%. Thus, it can be inferred

that the tensile twin reoriented a large extent of the matrix volume of the grain at the strain of 6.5%. Similarly, it was reported that the twin volume fraction became saturated, with a volume fraction of about 80% at the strain 6% [102]. In this simulation, the saturated twin volume fraction was set as 80% while the initial twin volume fraction was chosen as 1%.

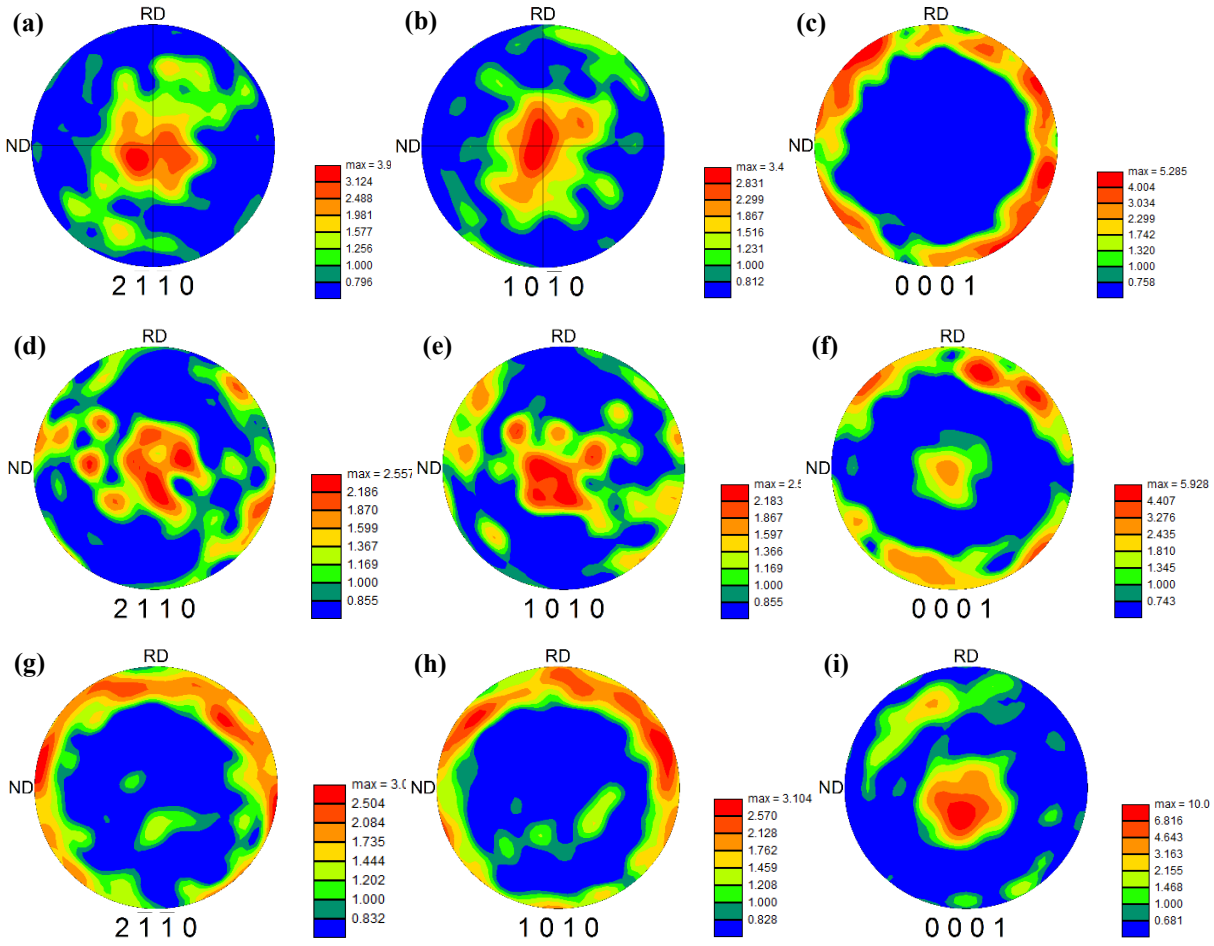

Fig. 6.22. The experimental results of the texture evolution of AZ31 Mg alloy with strain 0.15%: (a)-(c); strain 2%: (d)-(f) and strain 6.5%: (g)-(i).

Fig. 6.23 illustrates the simulation results of AZ31 Mg alloy compression strains of 2% . Generally, the simulation results are in good agreement with the experimental ones (see Fig. 6.23 (a)-(c). Due to twinning the *c* axis of most grains was reoriented by 86°, and as a result a sharp texture component in the center of the circle formed while the ring disappeared. Because the strain is quite small, the texture change caused by slip is relatively small and the main contribution to the texture evolution comes from tensile twinning.

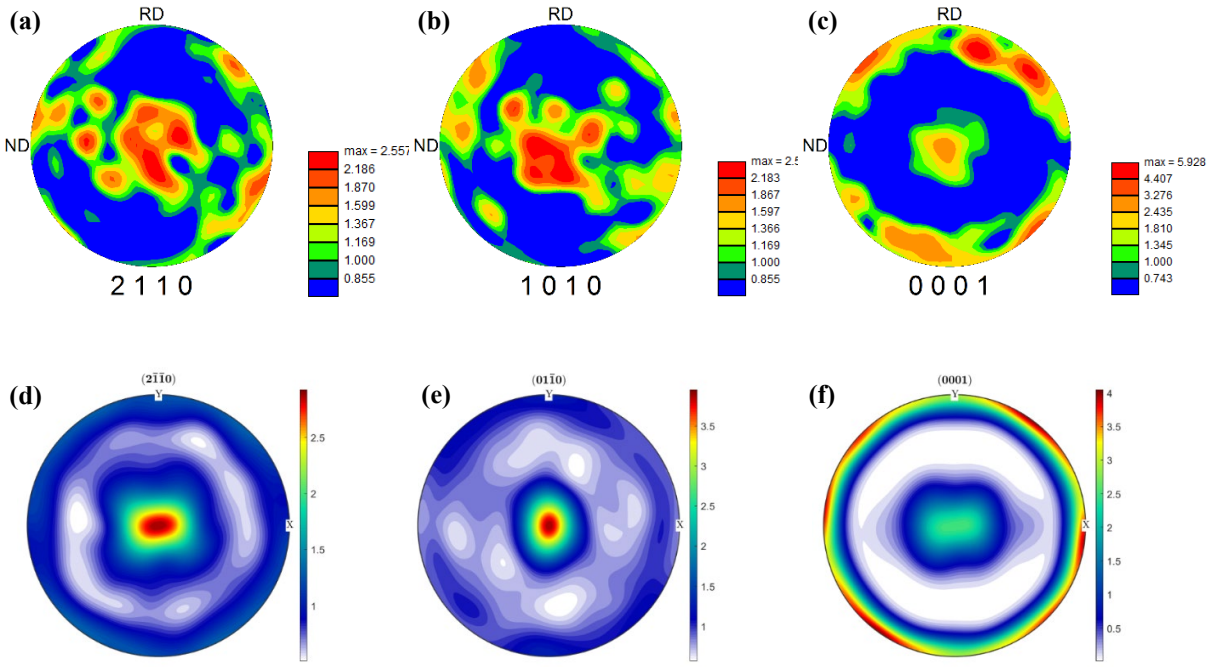

Fig. 6.23. Representative of simulation results (d-f) of the texture of extruded AZ31 Mg alloy with compression strain of 2% compared with experiments (a-c).

Fig. 6.24 illustrates the experimental and simulated flow curve of AZ31 Mg during deformation.

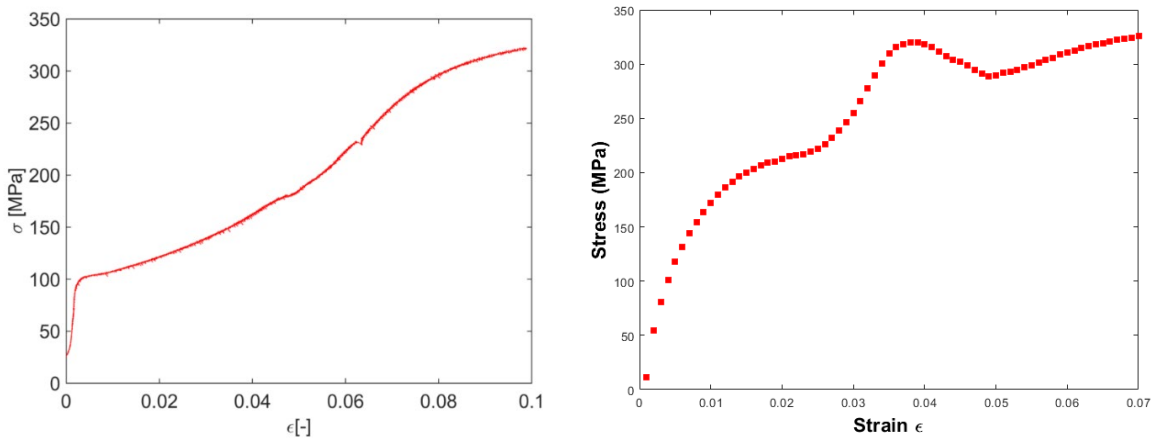

Fig. 6.24. The flow curve comparison between experimental and simulation

Our simulation reproduces experimental quite well at low and high strain, which in general confirms the validity of our model in predicting the mechanical response of hcp material, in terms of texture evolution and flow curve. The hardening rate exhibits a significant change with

strain. In the range 3%-7%, the hardening rate shows a monotonous increase, most likely caused by twin-twin interaction.

The largest difference is found at intermediate strain, where a closer inspection of input data, *i.e.*, the Voce hardening parameters, is necessary. The according choice of proper hardening parameters is an ongoing task. Actually, the present model still has great potential for improvements. Once the appropriate hardening law will be adopted, the model is supposed to deliver better prediction on flow curve. The present model employs rate-independent crystal plasticity, which has before been successfully developed and applied for fcc metals [112]. Rate-independent crystal plasticity avoids the necessity of solving non-linear equation

In the Voce hardening law, the hardening matrix has considered the cross hardening effects between different deformation modes. In order to find the relation between activity of twins and hardening we plot the relative activities of different deformation modes.

Fig. 6.25 exhibits the relative activities of different deformation modes. The definition of relative activity of different deformation modes can be seen in literature [113] The twin activity increase significantly and the during the stage 2%-4% experienced plummet, indicating that the twin volume fraction is rapidly getting saturated. Because in this stage twin-twin interaction impede the rapid growth of the twin, and therefore resulting in an increase hardening rate.

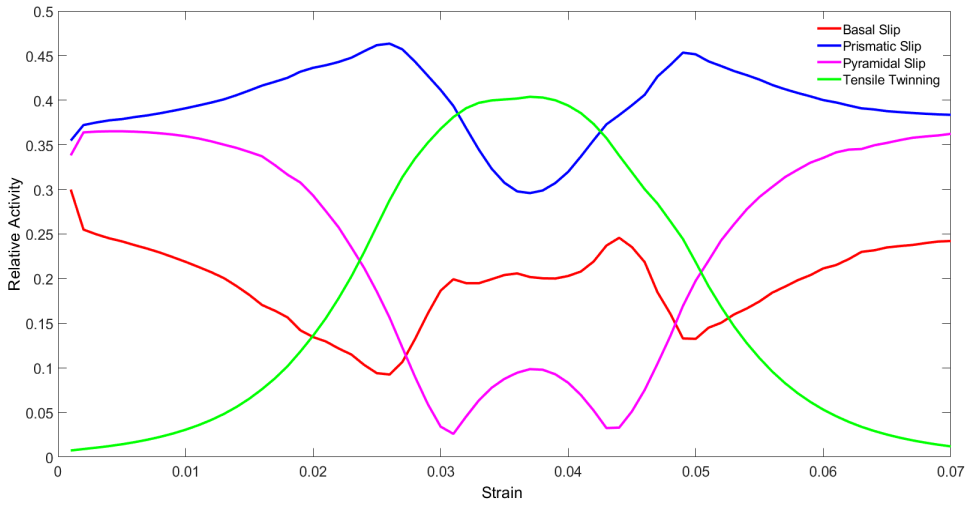

Fig. 6.25. The relative activity of different modes during the deformation process.

7 Conclusions and perspective for ensuing research

1) We established a semi-physically-based twin growth law, which accounts for the twin volume saturation and initial twin volume fraction after nucleation. A growth factor α of twin volume is included, which is required to determine the speed of twin volume fraction and its saturation. This factor is associated to twin-twin and twin-dislocation interactions. The proposed twin growth law is consistent with the experimental observations, and its simplicity facilitates its implementation into a texture model and delivers reasonable texture evolution consistent with the experimental results. α deserves further study, the effects of twin-twin interactions and twin-dislocation interactions on the twin saturation can be simulated by full field modeling approaches such as the CPFEM and phase field method. Also, the local stress caused by twin-twin interaction can be examined by CPFEM.

2) A mean field method based on the Taylor type model is developed, which includes a semi-physics consideration of evolution of the twin volume fraction. In the application to simulation of texture evolution of AZ31 Mg alloy, its simplicity of mathematical form saves computation time. A modified Taylor type relaxed constraint model is applied to simulate the texture evolution of as-extruded AZ31 alloy. The semi-empirical physics law of twin growth is embedded in this model and the minimum shear principle proposed by Bishop and Hill is applied to select the active slip systems. Instead of using computationally expensive and complicated rate sensitive constitutive laws, where nonlinear equations are required to be solved with, *e.g.*, the Newton-Raphson method, the present model avoids this numerical effort. Comparison of simulations with experimental results shows that the resulting fast computation of texture evolution is acceptable and reliable.

Bibliography

[1] Erica Lilleodden. Microcompression Study of Mg (0001) Single Crystal. Scripta Materialia, 62(8):532–535, 2010.

[2] F. Kabirian, A. S. Khan, and T. Gnäupel-Herlod. Visco-plastic Modeling of Mechanical Responses and Texture Evolution in Extruded AZ31 Magnesium alloy for Various Loading Conditions. International Journal of Plasticity, 68:1–20, 2015.

[3] G. Y. Chin and W. L. Mammel. Competition among Basal, Prism, and Pyramidal Slip Modes in hcp Metals. Metallurgical and Materials Transactions B, 1(3):357-361, 1970.

[4] S. R. Agnew and Ö. Duygulu. Plastic Anisotropy and the Role of Non-basal Slip in Magnesium alloy AZ31B. International Journal of Plasticity, 21(6):1161-1193, 2005.

[5] S. R. Agnew, M. H. Yoo and C. N. Tomé. Application of Texture Simulation to Understanding Mechanical Behavior of Mg and Solid Solution Alloys Containing Li or Y. Acta Materialia, 49(20):4277–4289, 2001.

[6] Ana Fernández, María Teresa Pérez Prado, Yujie Wei and Antoine Jérusalem. Continuum Modeling of the Response of a Mg Alloy AZ31 Rolled Sheet During Uniaxial Deformation. International Journal of Plasticity, 27(11): 1739–1757, 2011.

[7] X. Y. Lou, M. Li, R. K. Boger, S. R. Agnew and R. H. Wagoner. Hardening Evolution of AZ31B Mg Sheet. International Journal of Plasticity, 23(1):44–86, 2007.

[8] U. F. Kocks and D. G. Westlake. 1967. The Importance of Twinning for the Ductility of HCP polycrystals. Transactions of the Metallurgical Society of AIME, 239:1107–1109, 1967.

[9] E. W. Kelley, W. F. Hosford. The Deformation Characteristics of Textured Magnesium. Transactions of the Metallurgical Society of AIME, 242:654–661, 1968a.

[10] A. Couret and D. Caillard. An *in situ* Study of Prismatic Glide in Magnesium – I. The Rate Controlling Mechanism. Acta Metallurgica, 33(8):1447–1454, 1985.

[11] M. H. Yoo. Slip, Twinning, and Fracture in Hexagonal Close-Packed Metals. Metallurgical Transactions A, 12(3):409–418, 1981.

[12] H. E. Kadiri, C. D. Barrett, J. Wang and C. N. Tomé. Why are $\{10\bar{1}2\}$ Twins Profuse in Magnesium? Acta Materialia, 85:354–361, 2015.

[13] R. Bullough. Deformation Twinning in the Diamond Structure. Proceedings of the Royal Society A, 241(1227):568–577, 1957.

[14] A. Luque, M. Ghazisaeidi, W. A. Curtin. A New Mechanism for Twin growth in Mg Alloys, 81:442–456, 2014.

[15] I. J. Beyerlein and C. N. Tomé. A Probabilistic Twin Nucleation Model for HCP. Proceedings of the Royal Society A, 466:2517–2544, 2010.

[16] I. J. Beyerlein, J. Wang, M. R. Barnett and C. N. Tomé. Double Twinning Mechanisms in Magnesium Alloys via Dissociation of Lattice Dislocations. Proceedings of the Royal Society A, 468(2141):1496–1520, 2012.

[17] J. D. Robson, N. Stanford and M. R. Barnett. Effect of Particles in Promoting Twin Nucleation in a Mg-5 wt.% Zn Alloy. Scripta Materialia, 63(8):823–826, 2010.

[18] M. Y. Gong, G. S. Liu, J. Wang, L. Capolungo and C. N. Tomé. Atomistic Simulations of Interaction between Basal <a> Dislocations and Three-dimensional Twins in Magnesium. Acta Materialia, 155:187–198, 2018.

[19] B. Li, S. P. Joshi, O. Almagri, Q. Ma, K. T. Ramesh and T. Mukai. Rate-dependent Hardening Due to Twinning in an Ultrafine-grained Magnesium Alloy. Acta Materialia, 60(4):1818–1826, 2012.

[20] M. Knezevic, A. Levinson, R. Harris, R. K. Mishra, R. D. Doherty and S. R. Kalidindi. Deformation Twinning in AZ31: Influence on Strain Hardening and Texture Evolution. Acta Materialia, 58(19):6230–6242, 2010.

[21] G. C. Kaschner, C. N. Tomé, I. J. Beyerlein, S. C. Vogel, D. W. Brown and R. J. McCabe. Role of Twinning in the Hardening Response of Zirconium during Temperature Reloads. Acta Materialia, 54(11):2887–2896, 2006.

[22] C. N. Tomé, R. A. Lebensohn and U. F. Kocks. A Model for Texture Development Dominated by Deformation Twinning: Application to Zirconium Alloys. Acta Metallurgica et Materialia, 39(11):2667–2680, 1991

[23] J. F. Stohr and J. P. Poirier. Etude en Microscopie Electronique du Glissement Pyramidal $\{11\bar{2}2\}<11\bar{2}3>$ dans le Magnesium. The Philosophical Magazine: A, 25(6):1313–1329, 1972.

[24] T. Obara, H. Yoshinga and S. Morozumi. 1973. $\{11\bar{2}2\}<11\bar{2}3>$ Slip System in Magnesium. Acta Metallurgica, 21(7):845–853, 1973.

[25] A. Staroselsky and L. Anand. A Constitutive Model for hcp Materials Deforming by Slip and Twinning: Application to Magnesium Alloy AZ31B. International Journal of Plasticity, 19(10):1843–1864, 2013.

[26] H. Wang, P. D. Wu, J. Wang, C. N. Tomé. A Crystal Plasticity Model for Hexagonal Close Packed (HCP) Crystals including Twinning and De-twinning Mechanisms. International Journal of Plasticity 49:36–52, 2013.

[27] G. I. Taylor, Plastic Strain in Metals. Journal Institute of Metals, 62:307–324, 1938.

[28] F. Roters, P. Eisenlohr, L. Hantcherli, D. D. Tjahjanto, T. R. Bieler, D.Raabe. Overview of Constitutive Laws, Kinematics, Homogenization and Multiscale Methods in Crystal Plasticity Finite-Element Modeling: Theory, Experiments, Applications. Acta Materialia, 58(4):1152–1211, 2010.

[29] P. V. Houtte, S. Y. Li, M. Seefeldt, L. Delannay. Deformation Texture Prediction: from the Taylor model to the Advanced Lamel Model. International Journal of Plasticity, 21(3):589–624, 2005.

[30] J. F. W. Bishop and R. Hill. A Theory of the Plastic Distortion of a Polycrystalline Aggregate under Combined Stresses. Philosophical Magazine series, 42(327):414–427, 1951.

[31] W. B. Hutchinson and M. R. Barnett. Effective Values of Critical Resolved Shear Stress for Slip in Polycrystalline Magnesium and other hcp Metals. Scripta Materialia, 63(7):737–740, 2010.

[32] U. F. Kocks, C. N. Tomé and H. R. Wenk. Texture and Anisotropy: Preferred Orientations in Polycrystals and Their Effect on Materials Properties, pages 336–337. Cambridge University Press, 2000.

[33] R. J. Asaro and V. A. Lubarda. Mechanics of Solids and Materials, pages 506–507. Cambridge University Press, 2006.

[34] U. F. Kocks and H. Mecking. Physics and Phenomenology of Strain Hardening: the FCC Case. Progress in Materials Science, 48(3):171–274, 2003.

[35] R. J. Asaro and V. A. Lubarda. Mechanics of solids and materials, pages 503–504. Cambridge University Press, 2006.

[36] A. S. Khan, A. Pandey, T Gnäupel-Herold and R, K. Mishra. Mechanical Response and Texture Evolution of AZ31 Alloy at Large Strains for Different Strain Rates and Temperatures. International Journal of Plasticity, 27:688–706, 2011.

[37] B. Devincre, T. Hoc, L. B, Kubin. Dislocation Mean Free Paths and Strain Hardening of Crystals. Science, 320(5884):1745–1748, 2008.

[38] M. Khadyko, S. Dumoulin, G. Cailletaud and O. S. Hopperstad. Latent Hardening and Plastic Anisotropy Evolution in AA6060 Aluminum Alloy. International Journal of Plasticity, 76:51-74, 2016.

[39] N. Bertin, C. N. Tomé, I. J. Beyerlein, M. R. Barnett and L. Capolungo. On the Strength of Dislocation Interactions and Their Effect on Latent Hardening in Pure Magnesium. International Journal of Plasticity, 62:72–92, 2014.

[40] J. L. Bassani and T. Y. Wu. Latent Hardening in Single Crystals. Proceedings of the Royal Society A, 435:21-41, 1991.

[41] P. Franciosi and A. Zaoui. Multi slip in f.c.c. Crystals a Theoretical Approach Compared with Experimental Data. Acta Metallurgica, 30(8):1627–1637, 1982.

[42] F. F. Lavrentev and Y. A. Pokhil. Relation of Dislocation Density in Different Slip Systems to Work Hardening Parameters for Magnesium Crystals. Materials Science and Engineering, 18(2):261–270, 1975.

[43] H. E. Kadiri and A. L. Oppedal. A Crystal Plasticity Theory for Latent Hardening by Glide Twinning through Dislocation Transmutation and Twin Accommodation Effects. Journal of the Mechanics and Physics of Solids, 58(4):613–624, 2010.

[44] C. N. Tomé, P. J. Maudlin, R. A. Lebensohn and G. C. Kaschner. Mechanical Response of Zirconium—I. Derivation of A Polycrystal Constitutive Law and Finite Element Analysis. Acta Materialia, 49(15):3085–3096, 2001.

[45] C. E. Slone, S. Chakraborty, J. Miao, E. P. George, M. J. Mills and S. R. Niezgoda, Influence of Deformation Induced Nanoscale Twinning and FCC-HCP Transformation on Hardening and Texture Development in Medium-entropy CrCoNi Alloy. Acta Materialia, 158: 38–52, 2018.

[46] J. Singh, S. Mahesh, S. Roy, G. Kumar, D. Srivastava, G. K. Dey, N. Saibaba and I. Samajdar. Temperature Dependence of Work Hardening in Sparsely Twinning Zirconium. Acta Materialia, 123:337–349, 2017.

[47] C. N. Tomé, G. R. Canova, U. F. Kocks, N. Christodoulou and J. J. Jonas. The Relation between Macroscopic and Microscopic Strain Hardening in F.C.C. Polycrystals. Acta Metallurgica, 32(10):1637–1653, 1984.

[48] Q. Yu, J. Wang, Y. Y. Jiang, R. J. McCabe, N. Li, C. N. Tomé. Twin–Twin Interactions in Magnesium. Acta Materialia, 77:28–42, 2014.

[49] L. Jiang, J. J. Jonas, A. A. Luo, A. K. Sachdev and S. Godet. Influence of {10-12} Extension Twinning on the Flow Behavior of AZ31 Mg Alloy. Materials Science and Engineering:A, 445-446:302–309, 2007.

[50] H. E. Kadiri, J. Kapil, A. L. Oppedal, L. G. Hector, S. R. Agnew, M. Cherkaoui and S. C. Vogel. The Effect of Twin–Twin Interactions on the Nucleation and Propagation of $\{10\bar{1}2\}$ twinning in magnesium. Acta Materialia, 61:3549–3563, 2013.

[51] A. L. Oppedal, H. El Kadiri, C. N. Tomé, G. C. Kaschner, S. C. Vogel, J. C. Baird, M. F. Horstemeyer. Effect of Dislocation Transmutation on Modeling Hardening Mechanisms by Twinning in Magnesium. International Journal of Plasticity, 30–31:41–61, 2012.

[52] U. F. Kocks, C. N. Tomé and H. R. Wenk. Texture and Anisotropy: Preferred Orientations in Polycrystals and Their Effect on Materials Properties, pages 57–58. Cambridge University Press, 2000.

[53] H. J. Bunge. Texture Analysis in Materials Science -Mathematical Methods, pages 6-7. Butterworth & Co, 1982.

[54] M. A. Steiner, J. J. Bhattacharyya and S. R. Agnew. The Origin and Enhancement of {0001}<11$\bar{2}$0> Texture during Heat Treatment of Rolled AZ31B Magnesium Alloys. Acta Materialia, 95:443–455, 2015.

[55] A. Imandoust, C. D. Barrett, A. L. Oppedal, W. R. Whittington, Y. Paudel, H. El Kadiri. Nucleation and Preferential Growth Mechanism of Recrystallization Texture in High Purity Binary Magnesium-Rare Earth Alloys. Acta Materialia, 138:27-41, 2017.

[56] H. J. Bunge. Texture Analysis in Materials Science -Mathematical Methods, pages 47-48. Butterworth & Co, 1982.

[57] R. J Roe. Description of Crystallite Orientation in Polycrystalline Materials. III. General Solution to Pole Figure Inversion. Journal of Applied Physics, 36(6):2024-2031, 1965.

[58] F. Bachmann, R. Hielscher and H. Schäben. Texture Analysis with MTEX - Free and Open Source Software Toolbox. Solid State Phenomena, 160:63-68, 2010.

[59] M. M Avedesian and H. Baker. Magnesium and Magnesium alloys – ASM Speciality Handbook. Materials Park, OH: ASM International, 1999.

[60] S. R. Agnew, L. Capolungo and C. A. Calhoun. Connections between the basal I1 “growth” Fault and 〈c+a〉 dislocations. Acta Materialia, 82:255–265, 2015.

[61] B. C. Wonsiewicz. Plasticity of Magnesium Crystals. PhD thesis, Massachusetts Institute of Technology, 1966.

[62] R. Sánchez-Martín, M. T. Pérez-Prado, J. Segurado, J. Bohlen, I. Gutiérrez-Urrutia, J. Llorca and J.M. Molina-Aldareguia. Measuring the Critical Resolved Shear Stresses in Mg Alloys by Instrumented Nanoindentation. Acta Materialia, 71:283–292, 2014.

[63] J. Jeong, M. Alfreider, R. Konetschnik, D. Kiener, S. H. Oh. In-situ TEM Observation of {10$\bar{1}$2} Twin-Dominated Deformation of Mg Pillars: Twinning Mechanism, Size Effects and Rate Dependency. Acta Materialia, 158:407-421, 2018.

[64] G. P. M. Leyson, L. G. Hector, W. A. Curtin. First-principles prediction of yield stress for basal slip in Mg–Al alloys. Acta Materialia, 60(13-14):5197–5203, 2012.

[65] B. Syed, J. Geng, R. K. Mishra and K. S. Kumar. [0 0 0 1] Compression Response at Room Temperature of Single-Crystal Magnesium. Scripta Materialia, 67(7-8):700–703, 2012.

[66] M. Lentz, M. Risse, N. Schaefer, W. Reimers and I. J. Beyerlein. Strength and Ductility with {10T1}{10T2} Double Twinning in a Magnesium Alloy. Nature Communications. 7:11068 doi: 10.1038/ncomms11068 (2016).

[67] B. M. Morrow, R. J. Mccabe, E. K. Cerreta and C. N. Tomé. In-Situ TEM Observation of Twinning and Detwinning During Cyclic Loading in Mg. Metallurgical and Materials Transactions A, 45A: 36–39, 2014.

[68] D. Sarker, D. L. Chen. Detwinning and Strain Hardening of An Extruded Magnesium Alloy During Compression. Scripta Materialia, 67:165–168, 2012.

[69] J. Wang, N. Li, O. Anderoglu, X. Zhang, A. Misra, J. Y. Huang and J.P. Hirth. Acta Materialia, 58(6):2262-2270, 2010.

[70] Y. T. Zhu, X. Z. Liao, X. L. Wu and J. Narayan. Grain Size Effect on Deformation Twinning and Detwinning. Journal of Materials Science, 48:4467–4475, 2013.

[71] J. W. Christian, S. Mahajan. Deformation Twinning. Progress in Materials Science, 39:1–157, 1995.

[72] K. D. Lagerlöf, J. Castaing, P. Pirouz and A. H. Heuer. Nucleation and Growth of Deformation Twins: A Perspective Based on the Double-Cross-Slip Mechanism of Deformation Twinning. Philosophical Magazine A, 82(15):2841–2854, 2002.

[73] A. H. Cottrell and B. A. Bilby. A Mechanism for the Growth of Deformation Twins in Crystals. Philosophical Magazine A, 42(329):573–581, 1951.

[74] P. Pirouz. Deformation Mode in Silicon, Slip or Twinning? Scripta Metallurgica, 21(11): 1463–1468.

[75] S. Mahajan. Nucleation and Growth of Deformation Twins in Mo-35 at. % Re Alloy. The Philosophical Magazine: A, 26(1):161–171, 1972.

[76] I .J. Beyerlein, L. Capolungo, P. E. Marshall, R. J. McCabe and C. N. Tomé. Statistical Analyses of Deformation Twinning in Magnesium. Philosophical Magazine: A, 90(16):2161–2190, 2010.

[77] A. Khosravani, D. T. Fullwood, B. L. Adams, T. M. Rampton, M. P. Miles and R. K. Mishra. Nucleation and Propagation of $\{10\bar{1}2\}$ Twins in AZ31 Magnesium Alloy. Acta Materialia, 100:202-214, 2015.

[78] I. J. Beyerlein, R. J. McCabe and C. N. Tomé. Effect of Microstructure on the Nucleation of Deformation Twins in Polycrystalline High-Purity Magnesium: A Multi-Scale Modeling Study. Journal of the Mechanics and Physics of Solids, 59(5):988-1003, 2011.

[79] M. E. Gurtin, E. Fried and L. Anand. The Mechanics and Thermodynamics of Continua, pages 62–63. Cambridge University Press, 2010.

[80] S. N. Nasser. Micromechanics: Overall Properties of Heterogeneous Materials,pages 11–12. North Holland, 1998.

[81] A. S. Argon, Strengthening Mechanisms in Crystal Plasticity, pages 44–45. Oxford University Press, 2007.

[82] U. F. Kocks, C. N. Tomé and H. R. Wenk. Texture and Anisotropy: Preferred Orientations in Polycrystals and Their Effect on Materials Properties, pages 352–355. Cambridge University Press, 2000.

[83] U. F. Kocks, C. N. Tomé and H. R. Wenk. Texture and Anisotropy: Preferred Orientations in Polycrystals and Their Effect on Materials Properties, pages 373–374. Cambridge University Press, 2000.

[84] A. S. Khan and S. J. Huang. Continuum Theory of Plasticity, pages 390–395. John Wiley & Sons, Ltd, 1995.

[85] E. Kröner. Zur plastischen Verformung des Vielkristalls. Acta Metallurgica, 9(2):155–161, 1961.

[86] B. Budiansky and T. Y. Wu. Theoretical Prediction of Plastic Strains of Polyctrystals. Cambridge, Mass., Division of Engineering and Applied Physics, Harvard University, 1961.

[87] J. D. Eshelby. The Determination of the Elastic Field of an Ellipsoidal Inclusion, and Related Problems. Proceedings of the Royal Society A, 241(1226):376-398, 1957.

[88] T. Mura. Micromechanics of Defects in Solids, pages 129–165. The Netherlands: Martinus-Nijihoff, 1987

[89] R. Hill. A Self-Consistent Mechanics of Composite Materials. Journal of the Mechanics and Physics of Solids, 13(4):213–222, 1965.

[90] R. A. Lebensohn and C. N. Tomé. A Self-Consistent Anisotropic Approach for the Simulation of Plastic Deformation and Texture Development of Polycrystals: Application to zirconium alloys. Acta Metallurgica et Materialia, 41(9):2611-2624, 1993.

[91] I. J. Beyerlein and C. N. Tomé. A Dislocation-Based Constitutive Law for Pure Zr Including Temperature Effects. International Journal of Plasticity, 24:867–895, 2001.

[92] H. Wang, P. D. Wu, J. Wang and C. N. Tomé. A Crystal Plasticity Model for Hexagonal Close Packed (HCP) Crystals Including Twinning and De-twinning Mechanisms. International Journal of Plasticity, 49:36–52, 2013.

[93] S. B. Yi, C. H. Davies, H. G. Brokmeier, R. E. Bolmaro, K. U. Kainer, J. Homeyer. Deformation and Texture Evolution in AZ31 Magnesium Alloy During Uniaxial Loading. Acta Materialia, 54(2):549–562, 2006.

[94] S. H. Choi, E. J. Shin, B. S. Seong. Simulation of Deformation Twins and Deformation Texture in an AZ31 Mg Alloy under Uniaxial Compression. Acta Materialia 55(12):4181–4192, 2007.

[95] U. F. Kocks, C. N. Tomé and H. R. Wenk. Texture and Anisotropy: Preferred Orientations in Polycrystals and Their Effect on Materials Properties, pages 467–509. Cambridge University Press, 2000

[96] R. J. Asaro. Crystal Plasticity. Journal of Applied Mechanics, 50(4):921–934, 1983.

[97] M. R. Barnett, O. Bouaziz and L. S. Toth. A Microstructure Based Analytical Model for Tensile Twinning in a Rod Textured Mg alloy. International Journal of Plasticity, 72:151–167, 2015.

[98] L. Remy. Kinetics of f.c.c. Deformation Twinning and Its Relationship to Stress-Strain behavior. Acta Metallurgica, 26(3): 443–451, 1978.

[99] M. R. Barnett, A. Ghaderi, J. Fonseca and J. D. Robson. Influence of Orientation on Twin Nucleation and Growth at Low Strains in a Magnesium Alloy. Acta Materialia, 80:380–39, 2014.

[100] J. H Brunton and M. P. Wilson. Proceeding of the Royal Society A. The Kinetics of Twinning in Zinc and Tin Crystals, 309:345-361, 1969

[101] E. Nadgornyi. Dislocation Dynamics and Mechanical Properties of Crystals. Progress in Materials Science, 31:1–530, 1988.

[102] Y. Tadano, Y. Yoshihara and S. Hagihara. A Crystal Plasticity Modeling Considering Volume Fraction of Deformation Twinning. International Journal of Plasticity, 84:88–101, 2016.

[103] G. F. Bolling and R. H. Richma. Continual Mechanical Twinning: Part II : Standard Experiments. Acta Metallurgica, 13(7):723–743, 1965.

[104] I. Basu and T. Al-Samman. Twin Recrystallization Mechanisms in Magnesium-Rare Earth alloys. Acta Materialia, 96:111–132, 2015.

[105] M. Ullmann, M. Graf and R. Kawalla. Static Recrystallization Kinetics of a Twin-roll Cast AZ31 alloy. Materials Today: Proceedings, 2S:S212–S218, 2015.

[106] Z .R. Zeng, Y. M. Zhu, S. W. Xu, M. Z. Bian, C. H. Davies, N. Birbilis, J. F. Nie. Texture Evolution during Static Recrystallization of Cold-Rolled Magnesium Alloys. Acta Materialia, 105:479–494, 2016.

[107] X. P. Li, X. H. Li, J. Zhu, X. X. Ye, G. Y. Tang. Microstructure and Texture Evolution of Cold-Rolled Mg-3Al-1Zn Alloy by Electropulse Treatment Stimulating Recrystallization. Scripta Materialia, 112:23–27, 2016

[108] Q. Ma, B. Li, E. B. Marin and S. J. Horstemeyer. Twinning-induced Dynamic Recrystallization in a Magnesium Alloy Extruded at 450°C. Scripta Materialia, 65(9):823–826, 2011.

[109] Y. C. Xin, M. Y. Wang, Z. Zeng, G. J. Huang and Q. Liu. Tailoring the texture of magnesium alloy by twinning deformation to improve the rolling capability. Scripta Materialia 64(10):986–989, 2011.

[110] A. Chapuis, J. H. Driver. Temperature dependency of slip and twinning in plane strain compressed magnesium single crystals. Acta Materialia, 59(5):1986–1994, 2011.

[111] O. Bouaziz and P. Buessler. Iso-work Increment Assumption for Heterogeneous Material Behaviour Modelling, Advanced Engneering Materials, 6(1-2):79-83, 2004.

[112] L. Anand and M. Kothari. A Computational Procedure for Rate-Independent Crystal Plasticity. Journal of Mechanics and Physics of Solids, 44(4):525-558, 1996.

[113] M. Knezevic, R. J. McCabe, C. N. Tomé, R. A. Lebensohn, S. R. Chen, C. M. Cady, G. T. Gray III and B. Mihaila. Modeling Mechanical Response and Texture Evolution of α-uranium as a Function of Strain Rate and Temperature Using Polycrystal Plasticity. International Journal of Plasticity, 43:70-84, 2013.